UNIVERSITI TEKNOLOGI MARA

MATHEMATICAL MODELLING OF OPEN-CHANNEL DIVIDING FLOW IN VARIOUS CHANNEL FORMS FOR ESTIMATING DISCHARGE AND FLOW DEPTH RATIO

PUTERI NADIA SHAFIQAH BINTI HARMIZI

PhD

June 2026

UNIVERSITI TEKNOLOGI MARA

MATHEMATICAL MODELLING OF OPEN-CHANNEL DIVIDING FLOW IN VARIOUS CHANNEL FORMS FOR ESTIMATING DISCHARGE AND FLOW DEPTH RATIO

PUTERI NADIA SHAFIQAH BINTI HARMIZI

Thesis submitted in fulfilment
of the requirements for the degree of
Doctor of Philosophy
(Mathematics)

Faculty of Computer and Mathematical Sciences

June 2026

CONFIRMATION BY PANEL OF EXAMINERS

I certify that a Panel of Examiners has met on 7 January 2026 to conduct the final examination of Puteri Nadia Shafiqah Binti Harmizi on her Doctors of Philosophy thesis entitled "Mathematical Modelling of Open-Channel Dividing Flow in Various Channel Forms for Estimating Discharge and Flow Depth Ratio" in accordance with Universiti Teknologi MARA Act 1976 (Akta 173). The Panel of Examiners recommends that the student be awarded the relevant degree. The Panel of Examiners was as follows:

Suraya Masrom, PhD
Associate Professor
Faculty of Computer and Mathematical Sciences
Universiti Teknologi MARA
(Chairman)

Shaharuddin Cik Soh, PhD
Associate Professor
Faculty of Computer and Mathematical Sciences
Universiti Teknologi MARA
(Internal Examiner)

Leong Wah June, PhD
Professor
Faculty of Science
Universiti Putra Malaysia
(External Examiner)

PROF DR HJH ZURAEDA IBRAHIM
Dean
Institute of Postgraduates Studies
Universiti Teknologi MARA

Date: 12 June 2026

AUTHOR'S DECLARATION

I declare that the work in this thesis was carried out in accordance with the regulations of Universiti Teknologi MARA. It is original and is the results of my own work, unless otherwise indicated or acknowledged as referenced work. This thesis has not been submitted to any other academic institution or non-academic institution for any degree or qualification.

I, hereby, acknowledge that I have been supplied with the Academic Rules and Regulations for Post Graduate, Universiti Teknologi MARA, regulating the conduct of my study and research.

Name of Student	:	Puteri Nadia Shafiqah Binti Harmizi
Student ID. No.	:	2021575203
Programme	:	Doctor of Philosophy (Mathematics) – CS952
Faculty	:	Computer and Mathematical Sciences
Thesis Title	:	Mathematical Modelling of Open-Channel Dividing Flow in Various Channel Forms for Estimating Discharge and Flow Depth Ratio
Signature of Student	:	…… ……..
Date	:	June 2026

ABSTRACT

Dividing flow in open-channel is a great contributor to river and drainage management suggested by the authority to reduce overflow during heavy rainfall. Our systematic literature review have identified the general equations of dividing flow in trapezoidal and rectangular cross-sectional channels. Therefore, the objectives of this study is to develop a mathematical model of open-channel dividing flow in V-shaped cross-sectional channel. To enhance the model's accuracy and applicability, new dividing flow equations for trapezoidal, rectangular and V-shaped cross-sectional channels are derived which takes into account the Reynold's number. In addition, a new non-linear polynomial equation is formulated for predicting flow characteristics and evaluate the effect of division angles on flow depth using the Newton-Raphson method for trapezoidal, rectangular and V-shaped channels. Furthermore, dimensionless expressions for the width and length of the separation zone in the V-shaped channel are introduced to improve prediction of the discharge distribution. Maple software is used to implement the proposed equations produce the discharge and flow depth ratio. The results indicate that the discharge ratios in all channels remain below the critical discharge ratio at certain dividing angles, preventing the channel from overflow. Incorporating the Reynold's number as an alternative parameter in the proposed model demonstrates good agreement with FLOW-3D simulation data. The non-linear polynomial equations accurately predict flow depth while the separation zone expressions further improve prediction of discharge ratio. Additional analysis shows that Froude number and discharge ratio influence the behavior of flow depth in both channels. Lastly, the results indicate that the proposed models are capable of accurately estimating the discharge ratio and flow depth, with strong agreement observed when compared to experimental data from previous studies. These findings validate the capability of the mathematical models proposed in the study and demonstrate its potential for practical applications in open-channel hydraulic design.

ACKNOWLEDGEMENT

I would like to acknowledge and thank everyone who has been involved with this research. I would like to express my sincere gratitude to my supervisor Associate Professor Dr Iskandar Shah bin Mohd Zawawi. Without his knowledge, direction, guidance and all his help, this research would not have been achievable. He has been a great supervisor to me over the years. I would also like to show a great deal of appreciation to my co-supervisor Associate Professor Dr Mohd Agos Salim bin Nasir. I would also like to acknowledge how thankful I am for my lovely parents and Harmizi bin Azis. Without their unconditional love and support, and always believing in me throughout the years, I would not have been able to achieve a lot of my goals here at Universiti Teknologi MARA, Shah Alam. Last but not least, I would like to express thankful to Dr Mohd Ridza bin Mohd Haniffah and Siti Aimi Asyarah binti Zakaria from the Faculty of Civil Engineering, Universiti Teknologi Malaysia for their invaluable contributions to this research.

TABLE OF CONTENTS

		Page
CONFIRMATION BY PANEL OF EXAMINERS		**ii**
AUTHOR'S DECLARATION		**iii**
ABSTRACT		**iv**
ACKNOWLEDGEMENT		**v**
TABLE OF CONTENTS		**vi**
LIST OF TABLES		**x**
LIST OF FIGURES		**xii**
LIST OF SYMBOLS		**xiv**
LIST OF ABBREVIATIONS		**xv**
CHAPTER 1 INTRODUCTION		**1**
1.1	Introduction	1
1.2	Research Background	1
1.3	Problem Statement	3
1.4	Research Questions	6
1.5	Research Objectives	6
1.6	Significance of Study	6
1.7	Scope and Limitation of The Research	8
1.8	Research Flowchart	9
1.9	Organization of The Thesis	9
1.10	Definition of Terms	11
CHAPTER 2 LITERATURE REVIEW		**13**
2.1	Introduction	13
2.2	Open-channel flow	13
2.3	Dividing Flow	14
2.4	Type of Flow in Open-Channel	16
2.5	Separation Zone	19
2.6	Type of Cross-Sectional Channels	21

2.7 Modelling of Open-Channel Flow 23
2.8 Research Gap 27

CHAPTER 3 MATHEMATICAL MODELLING OF OPEN-CHANNEL DIVIDING FLOW 32
3.1 Introduction 32
3.2 Description of The Open-Channel Dividing Flow 32
3.3 Mathematical modelling of open-channel dividing flow 34
3.3.1 Trapezoidal cross-sectional channel 36
3.3.2 Rectangular Cross-Sectional Channel 37
3.3.3 V-shaped Cross-Sectional Channel 38
3.4 Geometric and Hydraulic Properties 43
3.5 Setting Up The Model Computation 44
3.5.1 Maple Application 45
3.5.2 Developing Interactive Math Apps 46
3.6 Results Analysis 48
3.6.1 Discharge Ratio in Trapezoidal Cross-Sectional Channel 49
3.6.2 Discharge Ratio in Rectangular Cross-Sectional Channel 53
3.6.3 Discharge Ratio in V-Shaped Cross-Sectional Channel 57
3.6.4 Summary of Division Angles for Trapezoidal, Rectangular and V-Shapes Cross-Sectional Channels 61
3.7 Conclusion 64

CHAPTER 4 MODELLING OF OPEN-CHANNEL DIVIDING FLOW WITH REYNOLD'S NUMBER 66
4.1 Introduction 66
4.2 Modelling of Dividing Flow 66
4.2.1 Trapezoidal Cross-Sectional Channel with Reynold's Number 67
4.2.2 Rectangular Cross-Sectional Channel with Reynold's Number 70
4.2.3 V-Shaped Cross-Sectional Channel with Reynold's Number 71
4.3 FLOW-3D Simulation 72
4.4 Setting Up Physics and Fluid Properties of FLOW-3D 73
4.5 Meshing and Geometry 73
4.6 Boundary and Initial Conditions 74

4.7 Results Analysis 77
4.7.1 Discharge Ratio in Trapezoidal Cross-Sectional Channel with Reynold's Number 78
4.7.2 Discharge Ratio in Rectangular Cross-Sectional Channel with Reynold's Number 81
4.7.3 Discharge Ratio in V-Shape Cross-Sectional Channel with Reynold's Number 85
4.8 Conclusion 86

CHAPTER 5 NUMERICAL ANALYSIS ON THE FLOW DEPTH BEHAVIOR IN OPEN-CHANNEL DIVIDING FLOW 88
5.1 Introduction 88
5.2 The Polynomial Equation of Open-Channel Dividing Flow 88
5.2.1 Trapezoidal Cross-Sectional Channel 89
5.2.2 Rectangular Cross-Sectional Channel 90
5.2.3 V-shaped Cross-Sectional Channel 91
5.3 Newton Raphson Method 92
5.4 The Geometric and Hydraulic Properties of Channels 94
5.5 Results validation 95
5.6 Parametric Investigation: Comparative Flow Characteristics 96
5.7 Conclusion 100

CHAPTER 6 MODELLING OF OPEN-CHANNEL DIVIDING FLOW FOR V-SHAPE CHANNEL WITH SEPARATION ZONE 102
6.1 Introduction 102
6.2 FLOW-3D Simulation Data 102
6.3 Mathematical Models for Dimensionless Width and Length of Separation Zone 107
6.4 Least Squares Regression Model for Length of The Separation Zone 110
6.5 Least Squares Regression Model for Width of The Separation Zone 111
6.6 Modelling of Open-Channel Dividing Flow with Separation Zone Shape Index 113
6.7 Results Analysis 114
6.7.1 Discharge Ratio with Length of Separation Zone 114

6.7.2 Discharge Ratio with Width of Separation Zone 115
6.8 Results validation 115
6.9 Conclusion 118

CHAPTER 7 CONCLUSION **119**
7.1 Conclusion 119
7.2 Future Research 121

REFERENCES **123**

APPENDICES **133**

AUTHOR'S PROFILE **175**

LIST OF TABLES

Tables	Title	Page
Table 1.1	Definition Terms	11
Table 2.1	Manning Roughness Coefficient Value (Surface Type)	18
Table 2.2	Summary of Selection Studies on The Open Channel Flow	29
Table 3.1	The Geometric Properties of Cross-Sectional Channel	34
Table 3.2	Geometric Hydraulic Properties for Trapezoidal Cross-Sectional Channel	43
Table 3.3	Geometric Hydraulic Properties for Rectangular Cross-Sectional Channel	43
Table 3.4	Geometric Hydraulic Properties for V-Shaped Cross-Sectional Channel	44
Table 3.5	The Discharge Ratio for Trapezoidal Channel for Case 1 And Case 2	50
Table 3.6	The Discharge Ratio for Rectangular Channel for Case 1 And Case 2	54
Table 3.7	The Discharge Ratio for V-Shape Channel for Case 1 and Case 2	58
Table 3.8	The Division Angles when	61
Table 3.9	The Cross-Sectional Shape with Division Angles	62
Table 4.1	The Discharge Ratio When $\theta_1 = 0°$	78
Table 4.2	The Discharge Ratio When $\theta_1 = 15°$	79
Table 4.3	The Discharge Ratio For OCDFR-R When $\theta_1 = 0°$ and $\theta_1 = 15°$	81
Table 4.4	The Discharge Ratio And Estimated Flow Depth For OCDFR-R, ANSYS-16 Simulation, And Laboratory Experiment	83
Table 4.5	The Deviation Percentage Of ANSYS-16 Simulation and OCDFR-R	84
Table 4.6	The Discharge Ratio For OCDFR-V When $\theta_1 = 0°$ and $\theta_1 = 15°$	85

Table 5.1	The Geometrical Properties Of The Channel Junction	94
Table 5.2	Characteristics of the channels and flow depth measured in experiment	95
Table 5.3	Deviation percentage between measured and predicted flow depth in channel 1, y_1 and depth ratio, y_r	95
Table 5.4	The Effect Of Discharge Ratio, q_r On Depth Ratio, y_r	97
Table 5.5	The Effect Of Froude Number, F_0 On Depth Ratio, y_r	97
Table 6.1	The Dimension Of The Separation Zone For $\theta_2 = 30^0$	105
Table 6.2	The Dimension Of The Separation Zone For $\theta_2 = 45^0$	106
Table 6.3	The Dimension Of The Separation Zone For $\theta_2 = 60^0$	106
Table 6.4	The Dimension Of The Separation Zone For $\theta_2 = 75^0$	106
Table 6.5	The Dimension Of The Separation Zone For $\theta_2 = 90^0$	107
Table 6.6	The Discharge Ratio Obtained By The OCDFLS-V	114
Table 6.7	The Discharge Ratio Obtained By The OCDFWS-V	115
Table 6.8	The Discharge Ratio Obtained By The OCDF-V And FLOW-3D	115
Table 6.9	The Comparison Of Deviation Percentage Between OCDF-V, OCDFLS-V And OCDFWS-V Models	116

LIST OF FIGURES

Figures	Title	Page
Figure 1.1	Research Flowchart	9
Figure 2.1	Separation Zone in Open-Channel Dividing Flow	20
Figure 2.2	Cross-Sectional Shape of The Channel	21
Figure 3.1	Schematic Layout of Open-Channel Dividing Flow	33
Figure 3.2	Diagram of Trapezoidal Cross-Sectional Channel	36
Figure 3.3	Diagram of Rectangular Cross-Sectional Channel	37
Figure 3.4	Diagram of V-Shaped Cross-Sectional Channel	39
Figure 3.5	Maple's Math Apps for Computing The Discharge Ratio in Open-Channel Dividing Flow	47
Figure 3.6	Graph of The Discharge Ratio Against Division Angles for The Trapezoidal Channel (Case 1)	52
Figure 3.7	Graph of The Discharge Ratio Against Division Angles for The Trapezoidal Channel (Case 2)	53
Figure 3.8	Graph of The Discharge Ratio Against Division Angles for The Rectangular Channel (Case 1)	56
Figure 3.9	Graph of The Discharge Ratio Against Division Angles for The Rectangular Channel (Case 2)	57
Figure 3.10	Graph of The Discharge Ratio Against Division Angles for The V-Shape Channel (Case 1)	60
Figure 3.11	Graph of The Discharge Ratio Against Division Angles for The V-Shape Channel (Case 2)	61
Figure 4.1	Actual geometry of the channel	74
Figure 4.2	FAVORized geometry of the channel	74
Figure 4.3	Velocity magnitude (m/s) when $\theta_1 = 0°$ and $\theta_2 = 15°$	75
Figure 4.4	Velocity magnitude (m/s) when $\theta_1 = 0°$ and $\theta_2 = 45°$	75
Figure 4.5	Velocity magnitude (m/s) when $\theta_1 = 0°$ and $\theta_2 = 90°$	76
Figure 4.6	Velocity magnitude (m/s) when $\theta_1 = 15°$ and $\theta_2 = 15°$	76
Figure 4.7	Velocity magnitude (m/s) when $\theta_1 = 15°$ and $\theta_2 = 45°$	77

Figure 4.8	Velocity magnitude (m/s) when $\theta_1 = 15°$ and $\theta_2 = 90°$	77
Figure 4.9	Graph Of The Discharge Ratio, q_r Against Division Angles, θ_2 When $\theta_1 = 0°$ for OCDF-T, OCDFR-T and FLOW-3D	80
Figure 4.10	Graph Of The Discharge Ratio, q_r Against Division Angles, θ_2 When $\theta_1 = 15°$ for OCDF-T, OCDFR-T and FLOW-3D	80
Figure 4.11	Graph Of The Discharge Ratio, q_r Against Division Angles, θ_2 When $\theta_1 = 0°$ and $15°$ for OCDFR-R	82
Figure 4.12	Graph Of The Discharge Ratio, q_r Against Bifurcation Angles, θ_2 When $\theta_1 = 0°$ and $15°$ for OCDFR-V	86
Figure 5.1	The Graph Of Effect Of Discharge Ratio On Depth Ratio For Trapezoidal, Rectangular And V-Shaped channels	99
Figure 5.2	The Graph Of Effect Of Froude Number On Depth Ratio For The Trapezoidal, Rectangular And V-Shaped Channel	100
Figure 6.1	Separation Zone Length And Width In The Branch Channel	103
Figure 6.2	Velocity Distribution At 15°	103
Figure 6.3	Velocity Distribution At 60°	104
Figure 6.4	Velocity Distribution At 30°	104
Figure 6.5	Velocity Distribution At 75°	104
Figure 6.6	Velocity Distribution At 45°	105
Figure 6.7	Velocity Distribution At 90°	105
Figure 6.8	The Graphs Of Maximum And Minimum Deviation Percentage For OCDFLS-V And OCDFWS-V Models	117

LIST OF SYMBOLS

Symbols

A	Cross-Sectional Area of The Channel
C	Constant
F	Froude Number
g	Gravitational Acceleration
k	Side Slope X Flow Depth to Bottom Width Ratio
P	Pressure Force
W_p	Wetted Perimeter
Q	Discharge
q_r	Discharge Ratio
b	Bottom Width of The Channel
B_r	Width Ratio
T	Top Width of The Channel
U	Momentum Transfer
V	Flow Velocity
y	Flow Depth
y_r	Flow Depth Ratio
ρ	Specific Gravity
γ	Specific Weight
θ	The Angle of The Bifurcation

LIST OF ABBREVIATIONS

Abbreviations

CFD	Computational Fluid Dynamics
DID	Department Of Irrigation and Drainage
GHP	Geometric Hydraulic Properties
GUI	Graphical User Interface
LSMLS	Least Squares Model with Length of Separation Zone
LSMWS	Least Squares Models with Width of Separation Zone
N/A	Not Applicable / Not Available
OCDFLS-V	Open-Channel Dividing Flow with The Length Separation Zone In V-Shaped Cross-Sectional Channel
OCDF-R	Open-Channel Dividing Flow in Rectangular Cross-Sectional Channel
OCDFR-R	Open-Channel Dividing Flow with Separation Zone In V-Shaped Cross-Sectional Channel
OCDFR-T	Open-Channel Dividing Flow with Reynold's Number In Trapezoidal Cross-Sectional Channel
OCDFR-V	Open-Channel Dividing Flow with Reynold's Number In V-Shaped Cross-Sectional Channel
OCDFS-V	Open-Channel Dividing Flow with Separation Zone In V-Shaped Cross-Sectional Channel
OCDF-T	Open-Channel Dividing Flow in Trapezoidal Cross-Sectional Channel
OCDF-V	Open-Channel Dividing Flow In V-Shaped Cross-Sectional Channel
OCDFWS-V	Open-Channel Dividing Flow with The Width of Separation Zone In V-Shaped Cross-Sectional Channel
WHO	World Health Organization

CHAPTER 1
INTRODUCTION

1.1 Introduction

This chapter presents a brief overview of the research, which includes the introduction, background of the research, problem statement, objective of the research, scope and limitation of the research, and significance of the research.

1.2 Research Background

Open-channel flow denotes to the movement of a fluid, typically water with a free surface area exposed to atmospheric pressure, driven by a gravity (Ravichandran et al., 2020). The free surface makes the open-channel more complex and difficult due to the large number of parameters and complex flow features related to the junction. The flow behavior in open channel flow is governed by the effects of viscosity and gravity relative to the inertial forces of the flow. The open-channel flow can be either natural or artificial channels. Natural channels are not regular or prismatic and their materials of construction can vary widely. Some examples of natural open-channel are rivers, streams, creeks, and bays. Artificial channels such as pipe, irrigation canals and drainage are human-made structures often designed with a regular cross-section shape and prismatic forms (Ben Meftah, 2022) .

An open-channel junctions occur when two or more channels converge or diverge, significantly influencing water management, energy distribution, and sediment transport. There are two main types of open-channel junctions that are categorized based on their geometry and flow configuration, which are combining and dividing. In the combined form of junction types, the two or more branches of the channel combine to form a single downstream channel, which is commonly seen in river system when tributaries join a main river. In contrast, bifurcating junction occurs when flow from the main channel splits into two or more downstream branches, obviously used in irrigation and flood control systems.

Various types of forces acting on open-channel flow affect the hydraulic behavior of the flow. Grace and Priest (1958) proposed experimental techniques to study the varying ratio of width in dividing flow from the main channel to the branch

channel, utilising the Froude number to describe the behavior of the flow, which includes three types of flow; critical, subcritical, and supercritical, affecting the behavior of the water surface and the occurrence of hydraulic jumps. A sub-critical flow or steady flow system occurs when the Froude number is less than one, indicating that gravity forces dominate in a deep channel, resulting in a steady flow with a low energy state. When inertial forces dominate in areas of rapid flow that exhibit a high energy state, the channel is shallow and possesses a Froude number exceeding one (Azimi & Shabanlou, 2016). A critical flow occurs when the Froude number is one, demonstrating that the inertial forces and gravity are equivalent.

The experimental studies on open-channel dividing flow play an important role in evaluating the scientific theories, gaining detailed insights into hydraulic behavior, validating theoretical or numerical models, and providing the basis mathematical model. However, experimental studies require specialized equipment, large physical space, considerable time and labour, which can be very costly and time-consuming. Therefore, mathematical models are increasingly used as a practical alternative or complement to the experimental studies for validation and improvement of model reliability. They rely on assumptions, flexibility of parameter, conditions, and their accuracy depends heavily on the quality of data input and the correctness of the underlying derived equations.

The advancement of mathematical modelling in open-channel flow is the consequence of cumulative contributions by many researchers throughout the centuries. Pandey & Mishra (2012) derived the fundamental equations for the combination and division of open-channel flow in trapezoidal and rectangular cross-sectional channels. Subsequently, Zawawi et al. (2019) elaborated on the mathematical modelling of dividing flow initially proposed by Pandey & Mishra (2012). The authors presented the derivation of general equation of dividing flow for trapezoidal channel by using algebraic manipulation and ratio principle. The relationship between the bifurcation angles and discharge ratio was investigated, revealing that selecting an appropriate bifurcation angle leads in the post-junction discharge ratio that is below the critical discharge ratio. Nevertheless, the methodologies of dividing flow proposed by Pandey & Mishra (2012) and Zawawi et al. (2019) have neglected the separation zone at the junction, which refers to a region of circulating or stagnant flow that forms near the inner wall of the downstream branches when flow is disrupted typically at junction. Their models may not fully capture the effects of flow characteristics and discharge

distribution. In particular, the influence of other junction geometry, flow depth, and Reynold's number on the discharge ratio remains a complex and not fully resolved issue.

In light of the complexities associated with the division flow, there remains a need for a comprehensive and predictive mathematical model that can accurately describe these phenomena under various conditions. This study aims to address this gap by deriving a model for estimating the discharge ratio using the fundamental momentum principle and continuity equation. It further explores the interrelationship between discharge ratio, flow depth, and division angles, which are critical parameters in channel design. Additionally, the effect of Reynold's number will be investigated to understand how different flow regimes influence the flow distribution. Thus, to improve the model's generality and applicability, a new mathematical model for V-shape channel involving the dimensionless width and length of separation zone will be derived to estimate the discharge ratio in certain division angles. Finally, the reliability and accuracy of the proposed models will be validated using numerical data obtained from the computational fluid dynamics (CFD) software, which is known as FLOW-3D simulation. To provide easy access to change the specified variables, the graphical user interface (GUI) will be constructed using Maple programming.

1.3 Problem Statement

In recent years, floods have become the most frequent type of natural disaster that impacts human life. Flood occurs when water overflows the natural or artificial boundaries of a river, stream, or drainage system, which are often caused by heavy rains, sudden snowmelt, and ruptured dams. According to the World Health Organization (WHO), there are three types of floods, which are flash floods, river floods, and coastal floods. River floods occurs when consistent rain forces a river to exceed its capacity. During a flood, the volume and velocity of water increase significantly, making the flow behavior at channel junctions or branches more complex and difficult to predict. Improperly designed dividing structures or misjudged flow division can lead to flooding in unintended areas, overloading of certain branches, and failure of flood protection systems.

The flow pattern at the water intake is very complex due to the dividing flow phenomenon, which is also influenced by the shape of the cross-sectional channel such

as trapezoidal, rectangular and V-shaped. A variety of cross-sectional channels should be investigated to determine the best channel that can avoid overflow in the channel after the junction. The design of channels commonly relies on rectangular and trapezoidal channels because of their simplicity and well-established hydraulic formulations. However, both geometries exhibit intrinsic limitations that affect flow performance, durability and cost efficiency. Rectangular channels exhibit hydraulic inefficiency due to their large wetted perimeter, causing elevated friction losses, energy dissipation, and reduced conveyance capacity, whereas trapezoidal channels, despite being more efficient, require a wider base that is unsuitable for space-restricted sites and are vulnerable to side-slope erosion under high-velocity flows. According to Guo et al. (2005), the most efficient cross-sectional channels can be determined by minimizing the excavated cross-sectional area or maximizing the flow capacity to a specified channel excavated area. The design of V-shaped cross-sectional channels allows for minimal excavation, while also generating minimal turbulence and shear stress. However, the hydraulic characteristics of dividing flow in V-shaped channel have not been fully explored, particularly in comparison with rectangular and trapezoidal channels. To address this gap, the present study develops mathematical models of open-channel dividing flow for trapezoidal, rectangular, and V-shaped cross-sections to investigate the influence of discharge ratio and flow depth ratio on different shape of cross-sectional channels.

Understanding and accurately investigating open-channel dividing flow is essential for flood forecasting, risk assessment, and the design of flood mitigation structures like diversion channels, floodways, and spillways. In hydraulic engineering field, research on dividing flow or bifurcation flow has commonly relied on numerical simulation and laboratory experiments, with a limited emphasis on mathematical modeling. Considering the expenses related to lab instruments and the limitations of simulation software, mathematical models are found to be practical and reasonable for effective flood management and infrastructure resilience.

The one-dimensional mathematical models are usually developed by applying the mass continuity equation, combined with a simplified momentum or energy conservation at the junction area. Accurately estimating the discharge ratio in open-channel dividing flow is critical for effective water flow distribution, yet existing empirical approaches often lack general applicability. This study seeks to formulate a mathematical model based on the fundamental principles of momentum conservation

and mass continuity, enabling an analytical estimation of the discharge ratio for varied channel geometries and flow conditions. The significance of the mathematical model lies in its ability to vary one variable at a time, thereby enabling the assessment of the relative importance of various variables or factors that influence the behavior of dividing flows, such as the size of the channel, the shape of the cross-sectional channel, the slope, the angle of bifurcations, the Froude number, channel roughness, the discharge ratio, and hydraulic properties.

A key challenge lies in quantifying the relationship between the division angles and depth flow ratio in dividing flow. Flow behavior in open-channel flow is significantly influenced by inertial and viscous forces, which are characterised by the Reynolds number. Existing models often neglect these effects, limiting their accuracy in turbulent regimes. This objective addresses the need to incorporate Reynolds number into the mathematical modeling of dividing flow, allowing for a more realistic representation of the flow physics. The trapezoidal model will be validated against numerical simulations conducted using FLOW-3D to ensure robustness across varying division angles.

The division angle influences not only the distribution of discharge but also flow depth in the resulting dividing channels. Despite its importance, the relationship between division angle and flow depth remains insufficiently comprehended, particularly in the context of dividing flow or confluence in open-channel. Furthermore, the impact of division angles on flow depth is not well quantified in existing analytical or empirical models, which often focused on combining flow. This research aims to numerically investigate the impact of different division angles on flow depth using numerical methods, providing valuable insights for optimizing channel design and mitigating flow imbalances.

One of the important characteristics, the separation zone, develops immediately downstream of the open-channel junction when branch flow enters, leading to changes in the discharge after the channel junction. During high-flow conditions, separation zones in dividing channels become more prominent and have a critical impact on the effectiveness of flow distribution, yet existing studies often overlooked in simplified models. Therefore, this study proposes a new mathematical model incorporating the separation zone shape index to refine the estimation of the discharge ratio, hence improving the accuracy under various conditions.

1.4 Research Questions

1. How can a mathematical model be developed to estimate the discharge ratio in open-channel dividing flow?
2. How can Reynold's number be integrated into a mathematical model of dividing flow to accurately estimate the discharge ratio?
3. How can mathematical model of open-channel dividing flow be modified to estimate the flow depth ratio?
4. How can a characteristic of the separation zone, specifically its dimensionless width and length be modelled and analysed to estimate the discharge ratio?
5. How can the performance of the proposed models be validated?

1.5 Research Objectives

With the problems stated above, this research will be conducted based on the following objectives:

1. To develop a mathematical model of open-channel dividing flow using momentum principle and continuity equations for estimating the discharge ratio.
2. To integrate Reynold's number into mathematical model of open-channel dividing flow for estimating the discharge ratio.
3. To modify the mathematical models of open-channel dividing flow in the form of non-linear polynomial equations for estimating the flow depth ratio.
4. To formulate a mathematical model of open-channel dividing flow for V-shaped channel by incorporating the dimensionless width and length of separation zone for estimating the discharge ratio.
5. To validate the performance of proposed models in terms of deviation percentage by comparing the results with numerical simulation and experiment data.

1.6 Significance of Study

The proposed research on the mathematical modeling of open-channel dividing flow aims to address critical gaps in hydraulic engineering, particularly concerning flood mitigation strategies, managing water distribution systems, irrigation networks, and stormwater infrastructure, where the division flow plays an important role. Existing

studies have primarily focused on standard bifurcation angles without adequately exploring the nuanced effects of varying division angles across different channel cross-sections. By systematically analyzing how discharge ratios are influenced by physical and hydraulic parameters, this study seeks to provide more comprehensive understanding of flow behavior at river bifurcations. Such insights are essential for refining theoretical models that predict flow distribution, contributing to the advancement of hydraulic theory and offering practical guidelines for designing more efficient water diversion structures.

Incorporating separation zones into the mathematical modeling of dividing flows represents a significant advancement in predicting the flow behavior. Separation zones, characterized by recirculating flow regions that can alter velocity distributions and pressure fields, have been shown to impact the efficiency of flow division and sediment transport. By developing models that account for these zones, the research aims to enhance the predictive accuracy of flow behavior at bifurcations, thereby informing the design of more effective flood mitigation infrastructure. This approach addresses the limitations of existing models that often overlook the complexities introduced by separation zones, thereby bridging a critical gap between theoretical predictions and observed flow behaviors.

The practical implications of this research extend to informing policy and operational decisions within governmental agencies, particularly the Department of Irrigation and Drainage (DID) in Malaysia, which can implement the proposed model to execute the bifurcation of the river in the flood-prone area, as it provides optimal angles for river bifurcation to alleviate floods. By providing a validated computational tool that can simulate various bifurcation scenarios, the study offers a resource for planning and implementing flood mitigation measures. This tool can assist in evaluating the potential outcomes of proposed interventions, optimizing resource allocation, and enhancing the resilience of flood-prone regions. Furthermore, the adaptable nature of the developed software ensures its applicability to diverse hydrological contexts, thereby extending its utility beyond the immediate geographical focus.

However, this study lays the groundwork for future research endeavors in hydraulic engineering and environmental management. The methodologies and findings can serve as a foundation for exploring related phenomena, such as sediment transport dynamics at bifurcations and the ecological impacts of altered flow regimes. Additionally, the integration of advanced mathematical modeling techniques with practical engineering

challenges exemplifies an interdisciplinary approach that can inspire subsequent studies aiming to address complex environmental issues. By bridging theoretical insights with practical applications, this research contributes to the ongoing discourse on sustainable water resource management and flood mitigation strategies.

1.7 Scope and Limitation of The Research

This study aims to propose a mathematical model for open-channel dividing flow, concentrating on three types of the cross-sectional channels: trapezoidal, rectangular and V-shaped channels. Since the trapezoidal and rectangular have already been discussed by the previous researchers, the details of modelling procedure will only be covered for V-shaped channels. The analysis of discharge ratio and depth ratio is dependent upon variations in division angles. The division angles employed in this study are below 90 degrees to examine the discharge ratio and flow depth. Additionally, data concerning hydraulic and geometric characteristics, encompassing channel characteristics and the Froude number, are adopted from the literature. Furthermore, the study introduces a novel perspective by incorporating the dimensionless width and length of separation zone into the modeling process. This study will employ Maple software to analyse the effects of varying the size of the separation zone on the discharge ratio.

However, the scope of this study is subject to several limitations. Notably, the feasibility of conducting physical experiments in a hydraulic laboratory to validate the mathematical models is constrained by the absence of laboratory facilities and the lack of available technical expertise. Moreover, physical experiments are often costly and time-consuming, which further restricts their inclusion in this study. The credibility of the results obtained from the proposed models is supported through validation using FLOW-3D simulations, which were conducted in collaboration with researchers from the Faculty of Civil Engineering, Universiti Teknologi Malaysia. However, the validation relies solely on some simulation data and published experimental results and is confined to just certain cross-sectional channel shapes, as simulated data for other geometries were unavailable.

1.8 Research Flowchart

In completing this study steps taken are briefly outlined as follows.

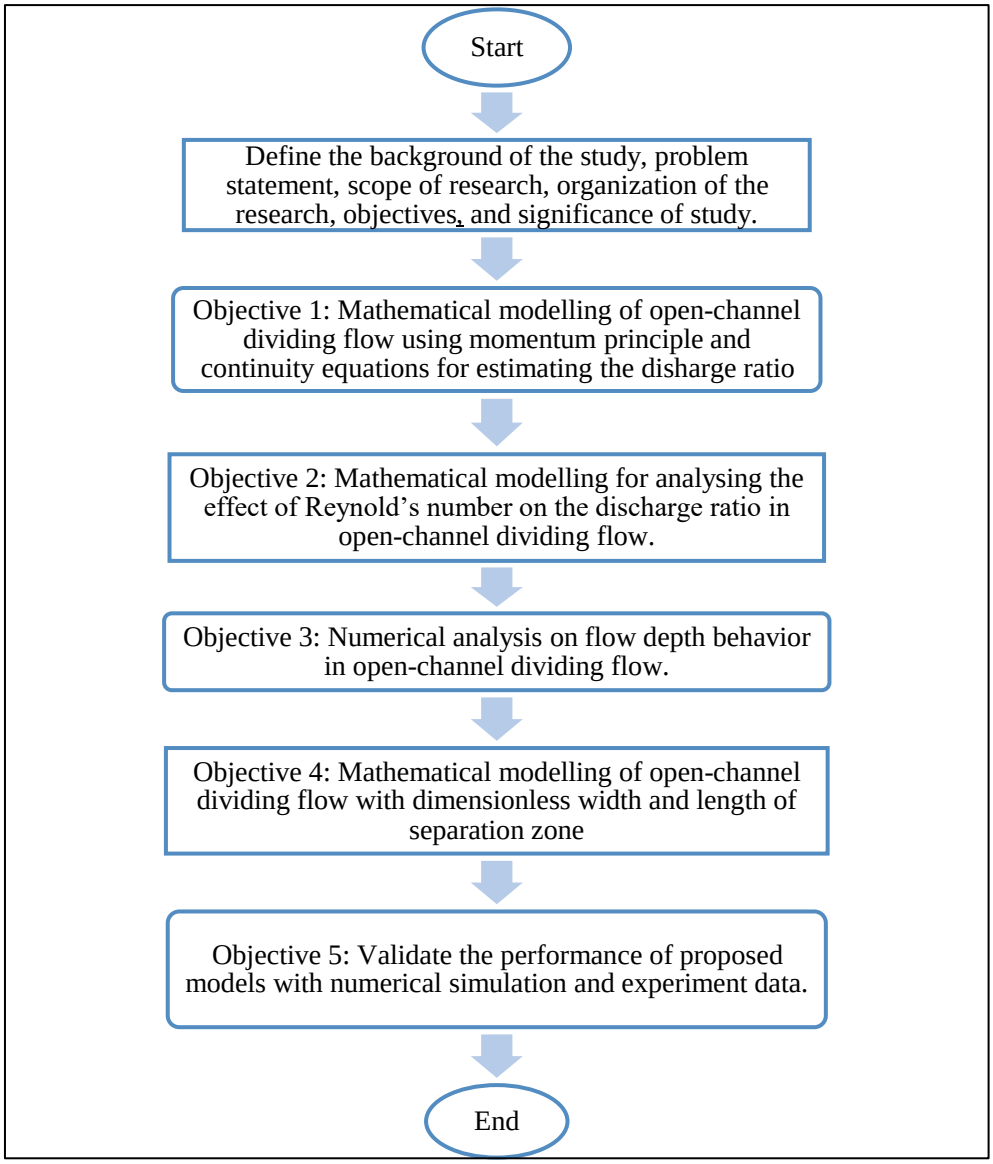


Figure 1.1 Research Flowchart

1.9 Organization of The Thesis

An overview of the organization of this thesis serves to systematically address the research objectives and provide comprehensive understanding of the research topics. Chapter 1 provides the background study of open-channel dividing flows with separation zones and mathematical modelling. This chapter identifies the problem statement, research gaps, research questions, research objectives, scope, limitations,

significance of the research and research flowchart. Furthermore, it offers a synopsis of the thesis organization to guide the reader through the ensuing chapters.

Chapter 2 reviews recent research in the study of the open channel flow, critically examining the fundamental principles governing open channel flows, the mechanisms and dynamics of separation zone in various geometries and existing mathematical modelling approaches for dividing flows. The chapter concludes with a critical synthesis that identifies specific gaps and inconsistencies within the existing body of knowledge, thus justifying the need for the present research.

This contribution of the study comprises four distinct main chapters. In each chapter, the theories, methods, and formulations regarding the modeling aspects will be discussed in the beginning of the sections, followed by the results and discussions of findings. Chapter 3 will focus on the mathematical modelling of open-channel dividing flow for various cross-sectional channels, including trapezoidal, rectangular, and V-shaped channels. This chapter will provide a detailed derivation of the V-shaped cross-section and analyse the discharge ratios for all types of channels with varying dividing angles. In addition, this chapter will present the applications of the open-channel dividing flow by computing the mathematical models using Maple software. This chapter introduces Maple's Math Apps as an innovative, effective, and pragmatic method to mathematical modeling.

Chapter 4 will be on the modeling of a new mathematical model of dividing open-channel flow for trapezoidal, rectangular and V-shaped cross-sectional channels based on the Reynolds number in the main channel to investigate the relationship between discharge ratio and dividing angles. This chapter presents the comparison of the results obtained by the mathematical models, FLOW-3D simulation and experimental data for the validation purposes. The accuracy of the models will be discussed based on its deviation percentage.

Chapter 5 will be on the study of the flow depth behavior in open channel dividing flow by modifying the fundamental equations of open-channel dividing flow in trapezoidal, rectangular and V-shaped cross-sectional channels in the form of a non-linear polynomial equation. The proposed equations are solved numerically using the Newton-Raphson procedure to determine the upstream flow depth. The predicted flow depths in both rectangular and trapezoidal open channel obtained by the proposed non-linear polynomial equation will be compared with the experimental results from the

literature studies. However, there is no validation for V-shaped cross-sectional channel because lack of the validation data.

In Chapter 6 a new mathematical modelling for V-shaped cross-sectional channels with separation zone will be proposed. The dimension of separation zone will be provided based on the simulation data obtained from the FLOW-3D software to produce the polynomial least-squares regression models with length and width of separation zone index. The absolute error or deviation percentage will be determined by evaluating the difference between the discharge ratio of the proposed models and simulation data.

Finally, Chapter 7 concludes the thesis by summarizing the major findings, explicitly addressing the research questions and hypotheses, and delineating the contributions made to the field of open-channel flow and mathematical modelling. It acknowledges the limitations encountered during the research process and proposes directions for future investigations. The chapter closes with reflective remarks on the significance and potential impact of the research outcomes.

1.10 Definition of Terms

The following are meaning of concepts and terms used in this study:

Table 1.1
Definition Terms

Terms	Definitions
Bed slope	The slope of the channel
Behavior of water flow	Any characteristics related to the flow of water includes its discharge, depth and type of flow
Continuity equation	A mass balance of a fluid flowing through a stationary volume element
Cross-sectional area	Two-dimensional area of a shape that is obtained when slicing the water flow with a plane that perpendicular to the direction of the flow
Discharge	Water passes per unit time
Discharge ratio	The ratio of upstream to downstream channel discharge
Flow depth	Distance of the lowest point of the channel's bed slope from the free surface of the water flow
Froude number	Ratio of gravitational acceleration and inertia

Hydraulic jump	Jump of water flow formed when the depth of the flow changes
Hydraulic radius	Ratio of cross-sectional area of the water that is flowing in the channel over the channel's wetted parameter
Hydrostatic pressure	Pressure that is been exerted by the water at equilibrium condition at a given point within the water
Momentum transfer	The amount of momentum that the water flow before the junction is given to the water flow after the junction
Open channel flow	Flow in a channel which have a free surface
Reynold's number	The ratio of the inertial force to the viscous force of a fluid flow
Separation zone	A region of low-velocity, low-pressure flow that develops at the junction of two channels.
Wetted Perimeter	The surface of the channel that touches physically the water

CHAPTER 2
LITERATURE REVIEW

2.1 Introduction

This chapter reviews the existing bodies of knowledge on open-channel dividing flow, separation zone and mathematical modelling. First, the chapter explains the basic principles of open-channel flow and discusses the occurrence of dividing channel, with particular emphasis on factors such as channel shape, bed slope, and flow velocity. Then, the laws of mass, momentum, and energy conservation are reviewed, which are the foundation for predicting flow behavior in open channels. The chapter investigates the various mathematical and numerical models that have been developed in the literatures to describe open-channel dividing flow, highlighting both their strengths and weaknesses. Challenges in modeling complex flow behaviors like turbulence and separation zones are also identified. The influence of channel geometry, such as rectangular, trapezoidal, and V-shaped cross-sections on the flow behavior is reviewed. Finally, the chapter summarizes key findings from past research, points out the existing gaps in the literature that this study aims to address, and explains the goals of this study, particularly the need for more comprehensive models.

2.2 Open-channel flow

Open-channel flow represents a fundamental area of hydraulic engineering involving the movement of water in conduits where the liquid surface is exposed to atmospheric pressure (Waller & Yitayew, 2016). The open-channel flow can be either natural or artificial channels. Natural channels are not regular or prismatic and their materials of construction can vary widely. Some examples of natural open-channel are rivers, streams, creeks and bays. Artificial channels are a human-made structures such as pipe, irrigation canals and drainage that often designed with a regular cross-section shape and prismatic forms (Ben Meftah, 2022) . The behavior of this flow is influenced by the interplay of viscosity, gravity and inertial forces (Ravichandran et al., 2020). According to Pradhan et al. (2024), the free surface makes the open-channel flow more complex due the large number of parameters and complex flow features. However, Pandey & Mishra (2012) said that the efficiency of any hydraulic network depends on

the discharge carrying capacity through the different elements of the system. In the design of an efficient channel network, junctions in open-channel are most critical element. Open-channel junction can be either a combining or dividing type. Therefore, understanding the phenomenon of flow division in open-channel is essential for this study. It will be discussed in the next section.

2.3 Dividing Flow

River bifurcations are natural divisions in the flow into two different channels resulting from morphological factors. A diversion is a specific instance of an asymmetric bifurcation in which one channel continues along its original channel; this is primarily constructed for various reasons, such as water supply and irrigation (Ibrahim et al., 2020). The current study concentrates on dividing flow or branching channel; hence, the review will emphasize this element. Many strategies have been proposed to preserve the stability dividing or bifurcation flow. One of the earliest literatures was studied by Kesserwani et al. (2010), predicting the discharge ratio with subcritical, supercritical, and transcritical flow at the right-angled open-channel junction. Researchers such as Alomari et al. (2018) and Cao et al. (2018) have suggested bifurcation angles below $90°$ to ensure flow stability and uniformity. Consequently, most of the previous studies related to open-channel dividing flows have employed a maximum $90°$ division angles. To enhance the predictive accuracy of bifurcation models, continued integration of new empirical data and refinement of existing methodologies is imperative. The longitudinal training walls have emerged as a viable alternative to traditional transverse groynes, effectively maintaining dividing flow stability and mitigating erosion at bifurcation points (Ruijsscher et al., 2019; Le et al., 2018). However, relying on extensive structural development and modification to manage dividing flows is not an effective approach.

Sayed (2019) concluded that discharge in the branch channel diminishes as the velocity, Froude number and momentum in the upstream main channel flow rise. It escalates with the augmentation of water depth in the upstream main channel and the widening of the branch channel's bed. In subcritical flow, the water depth in the primary channel diminishes in the downstream diversion zone. Conversely, it diminishes in depth within the branch channel. The water depth in the branch channel is consistently less than that of the main channel. The diversion of flow to the branch channel results

in a reduction of water depth downstream of the main channel. Alomari et al. (2020) studied the transport of sediment based on five diversion angles with different bed width ratios using physical model to maximise diversion flow and minimise diversion sediment. The results showed that the diversion channel flow and sediment discharge could be effectively managed by varying the diversion angles.

Shahari et al. (2021) have made further advancements on conservation principles to develop predictive equations for right-angled and short-branch channels, providing accurate flow estimations at bifurcations. Alfatlawi & Hussein (2024) reviewed the relevant kinds of literature to study the effect of physical features and models of branch channels, including the angle of diversion, discharge of the main channel, and slope of the bed on the flow quantity. The branch channel exhibits a decrease in velocity, momentum, and Froude number because of an increase in the upstream discharge of the main channel. It rises with the increasing water depth upstream in the branch and the width of the main channel bed. This review addresses the boundary condition and angle diversion of branch channels, indicating that the recirculation zone in the upstream branch channel declines as the diversion angle decreases.

Open-channel confluences introduce complexities due to flow separation, secondary circulation, and mixing processes. These phenomena complicate numerical modeling efforts, as conventional data sets often fail to capture the intricate three-dimensionality of flow fields (Nazari-Sharabian et al., 2020). Contractions and backwater effects further exacerbate prediction difficulties in lateral drainage systems. Their studies emphasize the importance of turbulence modeling and high-resolution numerical methods to address these challenges. Integrating empirical observations with simulations has improved the accuracy of predictions, concerning flow separation and recirculation patterns. Researchers have observed subcritical bifurcations at low elasticity numbers, where turbulence displays Newtonian-like characteristics, in contrast to the initial turbulence at raised elasticity values (Wan et al., 2021). These findings underscore the influence of fluid characteristics on flow dynamics.

The evolution of mathematical modeling for dividing flows has progressed from simplified analytical methods to sophisticated numerical simulations. The application of Taylor’s momentum principle initiated early investigations into open-channel junctions (Wuppukondur, 2018). Characterising hydraulic profiles in open channels is complicated by phenomena such as hydraulic jumps, secondary flows, and sediment

dynamics. Numerical models based on the Saint-Venant equations and volume of fluid (VOF) methods show promise but demonstrate significant sensitivity to boundary conditions and fluid properties (Harmizi et al., 2022; Welahettige et al., 2019). No single modeling framework can capture all flow behaviors, prompting a transition toward hybrid approaches that integrate empirical, analytical, and computational techniques for more accurate modelling.

2.4 Type of Flow in Open-Channel

Reynolds number plays fundamental role in fluid dynamics taking into account diffusive and convective effects. The Reynolds number value determinates the structure of the flow, its dynamical behavior and its quality for a given boundary conditions unambiguously. The Reynolds number can be defined as a non-dimensional parameter that represents the influence of viscosity relative to inertia and is important for analyzing the effect of gravity in fluid flow. It is defined as the ratio of inertial forces and gravitational forces (Macharia, 2014). Since the Reynold's number is defined as the ratio between the inertial and viscous forces, the mathematical definition is presented in equation 2.1 (Uruba, 2019):

$$\mathrm{Re} = \frac{VL}{v} \tag{2.1}$$

This indicator V represents the characteristic velocity of the flow, L is a characteristics length, such as the hydraulic diameter and v is the fluid kinematic viscosity. The changes in channel flow from laminar to turbulent depend on the Reynold's number. If the Reynold's number $\mathrm{Re} \leq 2000$, the fluid moves ordered layers and viscous forces dominate. This indicates that the flow is laminar. If $\mathrm{Re} > 4000$, the flow is turbulent where the inertial forces predominate and the flow is chaotic. If $2000 < \mathrm{Re} < 4000$, the flow is corresponded to a transition regime between laminar and turbulent (Saldana et al., 2024).

Reynold's number takes into account the viscosity of water. When the temperature of water increases, the viscosity decreases (Ahammed et al., 2016; Hemmat Esfe et al., 2016; Toghraie et al., 2016). Most of the researchers investigated the viscosity of the fluid at a temperature from $10°$ to $90°$ Celsius, but Abdurrasheed et al. (2019) used the temperature at $20°$ Celsius and the results are almost accurate when compared with numerical techniques and experimental data.

Other than findings the type of flow based on Reynold's number, the flow regime such as Froude number is prevalent in open-channels, where it describes the characteristics of the water flow based on parameters like velocity, flow depth, bed slope, and surface condition. The Froude number is a dimensionless metric that assesses the relative importance of inertial forces and gravitational effects in fluid dynamics, which can be defined as follows (Liu et al., 2024):

$$F = \frac{V}{\sqrt{gD}} \tag{2.2}$$

This indicator represents the ratio of the velocity of water, V to the celerity. This number is characterised as the velocity of propagation of a small amplitude wave on the surface, where g represents the gravitational constant and D denotes the hydraulic depth. The latter parameter denotes the ratio of cross-sectional area to the width of the top water surface. It is important to note that the Froude number is a dimensionless index, as both the numerator and denominator share the same unit of measurement (m/s). If a flow has a Froude number $F \geq 1$, the velocity of the water flow exceeds the wave velocity. This indicates that waves cannot travel upstream; they can only propagate downstream. The flow is referred to as supercritical in this instance. If $F \leq 1$, the flow velocity of water is less than the wave velocity, allowing waves to propagate in both upstream and downstream directions. The flow is called subcritical, except when $F = 1$, which is referred to as critical (Bryanskaya & Ostiakova, 2019).

Elevated Froude number values imply the dominant role of inertial forces, whereas reduced values indicate a greater influence of gravitational forces. This parameter is essential to evaluate the hydrodynamic performance of flow in submerged hydraulic conditions (Fesal et al., 2023). The Froude number is also important in the open-channel because it determines the types of flow of the open-channel. There are three types of the flow which are subcritical, supercritical and critical flow. Azimi & Shabanlou (2016) mentioned that when the flow depth is deep then it is a subcritical flow while the flow depth is shallow it is a supercritical flow. The Froude number concerns the flow depth in open-channel flow.

The Froude number and Reynold's number are quite similar since both measure the energy state of flow depending on the velocity of the flow, which can be calculated by using Manning velocity equation. The Manning's velocity equation is widely used to find the average flow velocity in the uniform open-channel flow, speed function of

channel, the hydraulic radius and slope of the channel (Nohani, 2019; Wibowo et al., 2015). The general expression of Manning's equation is given as follows:

$$Q = \frac{1}{n} A R_h^{\frac{2}{3}} S^{\frac{1}{2}} \tag{2.3}$$

where n is the roughness coefficient of Manning and S is the longitudinal slope of the channel, R_h is hydraulic radius, A is wetted cross-sectional area, and Q is discharge. Cowan's method has been applied to estimate the value of roughness coefficient of Manning formula by using geometry and hydraulic properties (Demir & Keskin, 2020; Mohammadi & Kashefipour, 2014). Manning's roughness coefficient is one of the most important parameters in the design and evaluation of surface irrigation of open-channel (Chen et al., 2023; Kamali et al., 2018). It is an empirically established quantity that is particularly influenced by surface roughness. The primary challenge in utilising the Manning formula lies in determining the roughness coefficient, as there is no exact method for estimating its value (Sabah & Bachir, 2023).

The value of Manning's roughness coefficient can be determined based on field observations or the engineering judgements, which varies based on the type of soil surface as shown in Table 2.1 (Jamal & Md Ali, 2023).

Table 2.1
Manning Roughness Coefficient Value (Surface Type)

Surface Type	**Manning's Roughness Coefficient, *n***
Coated cast iron	0.014
Glass	0.010
Concrete channel	0.013
Brick coated with mortar	0.015
Cement stone masonry	0.025
Clean earth channel	0.022
Earth channel	0.030
Channel with stone bed and grassed banks	0.040
Channel excavated in rock	0.040

In addition, the value of roughness coefficient can also be obtained based on the type and criteria of drainage. A high value indicates that the flow has high friction, while a low value indicates low friction in the flow. There are several factors that can influence the value of the roughness coefficient in open channel flow, such as surface roughness, channel alignment, vegetation, depth and flow rate, obstructions, channel irregularities,

and channel shape and size. Parsaie et al. (2017) investigated the flow rate of the rivers by using the empirical approaches including the Manning's formula. Teixeira et al. (2018) estimated the roughness coefficient of Manning along the river in Brazil and discussed the uncertainties and variations associated with this value. The analysis revealed that the uncertainties in flow and depth measurements affect the Manning coefficient value. Abd Elmoaty & T. A (2020) investigate the characteristics of Manning's roughness with the aquatic weeds. Tahmid et al. (2021) employed regression analysis to develop 11 polynomial equations for evaluating the Manning roughness coefficient of various rivers in Bangladesh, based on water depth, and validated through an error measurement parameter. Gautam (2021) deployed Manning's equation to ascertain the Manning's roughness coefficient in open channel flow by measuring velocity, cross-section, and bed slope in the Bijayapur irrigation system located in Kaski district, Nepal.

2.5 Separation Zone

The behaviour of dividing flow directly affects the inflow and outflow discharges at junction or branch, upstream and downstream water depths, and the presence of recirculation or separation zones within the branch channel (Feng et al., 2022; Hsu et al., 2002). Weber et al. (2001) claimed that the separation zone is influenced by the channel's geometry and bed discordance. The momentum of the lateral branch flow leads the main flow to detach at the downstream corner of the junction. The sudden change in the flow direction influences the flow separation in the channel. Several factors contribute to the formation of a separation zone at an open-channel junction. Unlike pressurized pipe flow, open-channel flow features a free surface, rendering it highly sensitive to channel geometry, bed slope, roughness, and flow velocity. Empirical studies have demonstrated that variations in these parameters significantly influence the formation of separation zones, which in turn affect water conveyance and sediment transport dynamics (Ali & Elhamaimi, 2020; Jasim et al., 2023). In practical scenarios, these factors govern the hydraulic performance of distribution systems and directly impact the structural stability of riverbanks and artificial channels.

A separation zone will occur near the entrance of the branch channel, a stagnation zone will appear near the downstream corner junction, and continuous

separation will develop along the far wall due to the flow expansion. Figure 2.1 illustrates the characteristics of the flow pattern when the flow is diverted (Pandey & Mohapatra, 2019).

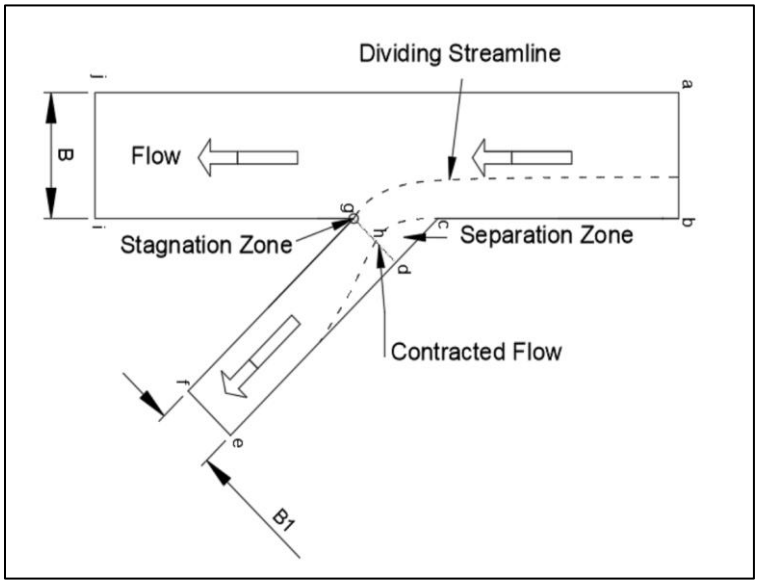


Figure 2.1 Separation Zone in Open-Channel Dividing Flow

Separation zones can be formed by shifting flow regimes due to slight variations in geometry or inflow ratios. The size of the separation zone is easily determined in an artificial open-channel as the cross section and the geometry of the downstream corner can generate lateral currents directed into the separation zone. The dimensions of the separation zone are significantly different for non-rectangular shapes. Flow separation is undeniably visible at the confluences of such channels (Ramamurthy et al., 1989; Rooniyan, 2014; Webber et al., 1967). However, the flow characteristics of the separation zone are influenced by the discharge ratio and angle of the bifurcation (Sui & Huang, 2017).

Earlier studies by Best & Reid (1985) found that the separation zone in open-channel flow expands in width and length as the angle of bifurcation increases. Specifically, as the confluence angle rises from 15° to 90°, both dimensions of the separation zone expand progressively, but the actual width is smaller than that predicted by mathematical models. However, the researcher discovered that the separation zone forms along the downstream wall when the branch channel angle is small, such as 30° , and along the upstream wall when the angle is larger, such as 90° (Alomari et al., 2016; Lama et al., 2003, 2002). Comparative analysis of separation zone sizes at various

bifurcation angles have indicated that an angle of $55°$ minimizes the separation zone in the intake channel (Ramamurthy et al., 2007). The increase of the bifurcation angle will increase both length and width of the separation zone (Hassan & Shabat, 2023).

Previous studies were conducted to investigate the separation zone and various division angles and discharge ratio. Jamshidi et al. (2016) measured dimensions of flow separation zone. In all experiments, separation zone decreases with an increase in non-dimensional parameter of discharge ratio. According to Pandey et al. (2019), an increase in the discharge ratio will lead to a reduction in the length and width of the separation zone. Sayed Abu-Zaid (2023) employed three-dimensional numerical modelling and demonstrated that a $15°$ diversion angle maximises the bifurcating channel flow rate, while minimizing the separation zone. Alfatlawi & Hussein (2024) conducted experimental and numerical investigations using FLOW-3D software, revealing that a diversion angle of $25°$ optimally reduces the separation zone size while enhancing discharge into the branch channel.

2.6 Type of Cross-Sectional Channels

Channel geometry plays a significant role in determining the hydraulic behavior in open-channel flow, particularly in bifurcation channel where separation and turbulence are influenced by its cross-sectional shape. The different geometries, such as rectangular, trapezoidal, and semi-circular channels produce varying flow separation zones and turbulence intensities. Figure 2.2 shows the types of cross-sectional channels (Schindfessel et al., 2017).

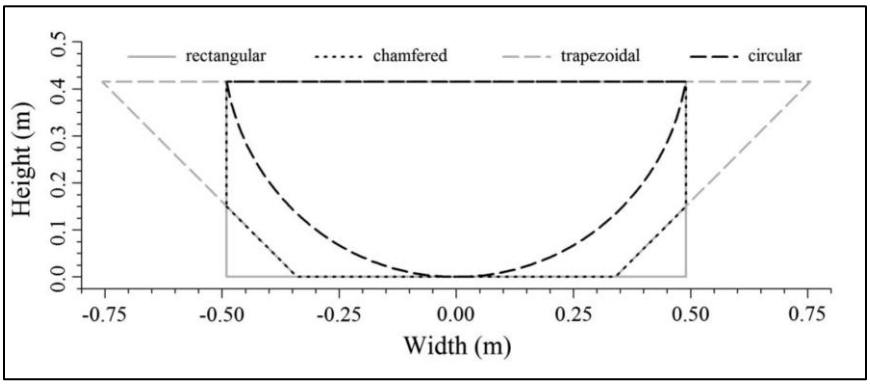


Figure 2.2 Cross-Sectional Shape of The Channel

The most common channel sections of open channel flow that have been studied by the previous research are trapezoidal and rectangular. For instance, Pandey & Mishra (2012), proposed mathematical equations for trapezoidal and rectangular cross-sectional channels in combining and dividing open-channel to investigate the relationship between depth ratio and complex flow features. The results showed that the depth ratio in both channels increases when the discharge ratio increases. Mohammed (2015) investigated the relationship between discharge and flow depth in a rectangular cross-sectional channel.

In other study, Schindfessel et al. (2017) elaborated on the influence of the cross-sectional shape (semi-circular, rectangular and trapezoidal) of the separation zone in a junction using large-eddy simulation models to stimulate the complex turbulent flow. The results show that the dimensions of the separation zone are significantly influenced by cross-sectional channel. Azma & Zhang (2020a) have focused on the rectangular cross-sectional shape to investigate the flow behavior with different hydraulic and discharge conditions. Then, Azma & Zhang (2020b) investigated the effect of the variations in tributary channel width with trapezoidal and rectangular on the flow parameters, and vertical structure in a T-shape confluence. Subsequently, Malik & Abdul Matin (2021) investigated transport of sediment in a bifurcation of a rectangular channel with varying bifurcation angles. The discharge and sediment ratio between the branch and main channels increased with an increase in the bifurcation angle.

Comparative analyses of rectangular and trapezoidal channels show that with equal bottom width and flow depth, rectangular sections typically exhibit higher depth ratios at the junctions. This indicates greater flow resistance and more pronounced separation tendencies in rectangular channels (Shahari et al., 2021). Trapezoidal channels allow smoother transitions and more uniform discharge distributions due to their sloped sides. These differences underscore the necessity for geometry-specific modelling approaches when analysing flow division and hydraulic behavior at channel junctions.

According to Qiu et al. (2023), the cross-sectional shape of an open-channel significantly influences flow capacity in the channel. The width-to-wetted perimeter ratio affects the discharge capacity in laminar and turbulent flow with variations observed across different shapes like rectangular, trapezoidal, and compound. Numerical models have shown that mechanical energy losses vary with the volume and shape of the cross-section channel. Trapezoidal and compound channels generally

exhibit lower energy losses than rectangular, contributing to more efficient flow conveyance. Secondary flows, which are prominent in curved or asymmetrical channels, are also sensitive to cross-sectional geometry. An experimental study revealed that the structure and intensity of these flows vary significantly with the shape of the channel, altering shear stress distribution and affecting sediment transport and channel stability (Hu & Zhang, 2018). For instance, trapezoidal channels with steeper side slopes generate stronger spanwise secondary currents, which in turn affect boundary shear stress profiles more dramatically than in flatter sections.

2.7 Modelling of Open-Channel Flow

The fundamental principles governing open-channel flow models are described through the continuity, momentum, and energy equations, which serve as the foundation for most analytical, numerical models, and hydraulic mathematical models (Sayed Abu-Zaid, 2023). The continuity equation (mass conservation) expresses the principle that mass cannot be created or destroyed in a flow system. Any increase in flow into a section must either increase the depth of water or outflow. The momentum equation (conservation of momentum or force balance) accounts for the balance between external forces and the change in momentum of the fluid, which results in acceleration or deceleration of flow. Meanwhile, the energy equation (conservation of energy) accounts for the total mechanical energy, including potential, kinetic, and pressure in the flow. As flow moves, energy can convert from one form to another, for example, velocity to depth, but the total energy is conserved. Continuity and momentum equations govern the movement of unsteady flows in open channels, known as Saint–Venant equations (David et al., 2024). The robustness of the Saint-Venant equations in maintaining mass and momentum balance, even in flows with obstructions and contractions, has been validated through numerical simulations (Fadl-Elmola et al., 2021). These foundational theories continue to refine hydraulic models, ensuring that conservation principles are adequately represented in the research on open-channel flow. Mnassri & Triki (2021) examine the discharge ratio in trapezoidal channel by using the 1-D Extended Saint-Venant based on Prandtl power law as a momentum correction coefficient. Muhamediyeva et al. (2024) investigated the flow characteristics such as discharge, free surface elevation, and flow velocity in the main channel using Saint-Venant equations.

Various numerical techniques, including finite difference and finite element methods are employed to solve these open-channel equations, facilitating the analysis of complex flow scenarios such as flood waves and transactions between free surface and pressurized flows (A et al., 2015). Furthermore, Ac et al. (2021) utilized the finite difference method to study the effect of a difference in angle in two lateral inflow channels on the main channel's velocity. This study examined the flow from two lateral inflow channels in an open rectangular artificial channel of an incompressible Newtonian fluid with one-dimensional and unsteady. Nazir & Awan (2021) investigated flood flow routing by using the finite difference method with overbank unsteady flow in an open channel. The effectiveness of this method to optimize the choice of finite difference method is more accurate than other methods, having adequate space and time steps. Xue et al. (2023) examined a numerical model for one-dimensional open-channel flow, incorporating a pressure term in the momentum equation and utilizing a Harten Lax and van Leer Riemann solver, achieving second-order accuracy through an upwind scheme and Runge-Kutta discretization. Specifically, Magdalena et al. (2024) utilised the Saint-Venant Equations to explore fluid flow evolution in irregular channels. This model is solved numerically using a staggered finite volume method and validated with data collection from laboratory experiment. Nyaga et al. (2024) developed a finite difference to solve the effect of length and angle of bifurcation of the lateral channel on the flow velocity in the main channel.

Computational hydraulics fluid dynamics (CFD) models in hydro-environmental engineering exhibit a wide range of foundational formulations to predict the flow behaviour within open-channels. The fundamental equations that govern the physics of fluid mechanics and thermal sciences, vital in CFD, include the continuity equations, Navier–Stokes equations, and energy equations. Zahran et al. (2019) proposed analytical models based on the Navier-Stokes equation and k-c turbulent model to replicate flow characteristics at junctions. However, the analytical solutions gave a greater error than numerical solutions with a maximum discrepancy for the rectangular channel and irregular channel than the published experimental data. Furthermore, the Navier–Stokes equations are frequently considered some of the most complex and difficult equations to apply and solve. The set of coupled time-dependent nonlinear equations requires multiple approximations to obtain analytical solutions.

Goudarzizadeh & Musavi-Jahromi (2020) applied the Reynolds stress turbulence model (RSM) to simulate turbulent flow at a 90° equal-width open-channel

junction, indicating that an increase in discharge ratio reduces the separation zone's length and width. Ouro et al. (2024) compared six distinct computational models: Iber Plus, High-Order Shallow Water Model (HO-SWM), Godunov-type Boussinesq Volume Conservative model (GBVC), Open Field Operation and Manipulation Reynolds-Averaged Navier-Stokes (OpenFOAM (RANS)), Hydro3D large Eddy simulation model (LES), and Dual Smoothed Particle Hydrodynamics (DualSPHysics (SPH)), focussing on their ability to predict mean velocities and free-surface dynamics in two benchmarks featuring open-channel flows with symmetric lateral cavities. Alfatlawi & Hussein (2024) employed FLOW-3D, a numerical three-dimensional (3D) software that utilises CFD principles and integrates certain governing equations, mesh type and size, as well as initial and boundary conditions. T. J. M. Alfatlawi & Hussein (2024) utilized FLOW-3D to simulate branching flows, focusing on optimizing diversion angles to achieve maximum discharge ratios and minimum separation zones. The results were presented for many different flow discharge ratios depending on two inflow discharges. The software is validated with experimental data and demonstrates good agreement.

Research on open-channel flow later advanced with the exploration of mathematical modelling, which is crucial for validating experimental outcomes. Ramamurthy et al. (2007) developed mathematical models with a rectangular and trapezoidal cross-sectional channel using momentum principle to compare the flow depth features. The mathematical model formulations reveal substantial differences between combining and dividing flows in trapezoidal and rectangular $\left(k_3 = 0\right)$, which are given as follows:

Combining flow equation:

$$\begin{aligned}&\left(1+2k_3\right)\left[\frac{1}{2}\left(y_r{}^2-1\right)+\frac{k_3}{3}\left(y_r{}^3-1\right)\right]\\&=F_3^2\left(1+k_3\right)^2\left[1-\frac{1+k_3}{y_r}\left(\frac{\left(1-q_r\right)^2}{Br_1+k_3y_r}\cos\theta_1+\frac{q_r{}^2}{Br_2+k_3y_r}\cos\theta_2\right)\right]\end{aligned} \tag{2.4}$$

Dividing flow equation:

$$\left(1+2k_3\right)\left[\frac{1}{2}\left(y_r{}^2-1-Br_2y_r{}^2\cos\theta_2\right)+\frac{k_3}{3}\left(y_r{}^2\left(1+\cos\theta_1\right)-1\right)\right]$$
$$=F_3^2\left(1+k_3\right)^2\left[1-C\left(q_r\sin\theta_2+\left(1-q_r\right)\sin\theta_1\right)-\frac{1+k_3}{y_r}\left(\frac{\left(1-q_r\right)^2}{Br_1+k_3y_r}\cos\theta_1+\frac{q_r{}^2}{Br_2+k_3y_r}\cos\theta_2\right)\right]. \quad (2.5)$$

where k_3 is the side slope/flow depth to bottom width ratio, y_r is the flow depth ratio, B_r is the width ratio, F_3 is the Froude number, q_r is the discharge ratio, and $C=\frac{5}{6}-\frac{F_3^2}{40}-\frac{k_3}{12q_r}\left(\frac{1+2k_3}{(1+k_3)^2}\right)$ is constant in momentum transfer coefficient for trapezoidal channel junction given by Pandey & Mishra (2012). Subscript of 3 represents the main channel, while subscripts of 1 and 2 represent the branch channel of open-channel dividing flow. This study concluded that the depth ratio must be different upstream and downstream to prevent river overflow.

For instance, Cheng et al. (2018) applied the theory of algebraic inequality to determine the critical depth for steady non-uniform flow in open channels. They emphasized that the polynomial is too challenging to be solved. The evaluation of the correlations between flow cross-sectional area and flow depth for typical cross-sectional shapes indicates that there exist analytical and numerical solutions for determining critical depth. Pourbakhshian & Pouraminian (2021) proposed conceptual and analytical models to study the optimal design for trapezoidal composite channel cross-sections with different discharge values. The mathematical models of channel construction cost were presented based on design variables, Froude number, flow velocity, and channel depth for each specified discharge.

Recent studies have highlighted advancements in modelling techniques that enhance accuracy and applicability in real-world scenarios. Zakaria et al. (2025) investigated the relationship between the separation zone and the discharge ratio. Their findings indicate that a decrease in the width of the separation zone leads to an increase in the effective flow directed into the branch channel. Comparably, Harmizi et al. (2023) examined dividing flow in open channels to analyse the flow depth behaviour between trapezoidal and rectangular cross-sectional channels using a non-linear polynomial equation. In other research, Shahari et al. (2021) investigated the relationship between

flow depth, Froude number, and flow rate ratio by solving a non-linear polynomial equation for combining flows in trapezoidal and V-shaped channels. As the Froude number and flow rate ratio increase, the flow depth in the trapezoidal channel is greater than in the V-shaped channel.

Then, Zawawi et al. (2019) detailed out the technique to derive the dividing flow equation in (2.5) proposed by Pandey & Mishra (2012) using algebraic manipulation and ratio principle. The authors reviewed the model's derivation to study the effect of bifurcation angles on the river flow rate ratio. The results of the study reveal that by using an appropriate bifurcation angle, the flow rate of the river after the channel is below the critical flow rate ratio. Although certain researchers in this field have recommended an analysis between the discharge ratio and division angles, their studies appear to be applicable primarily to cases involving different channel widths. The evaluation of discharge ratios at different division angles should be performed with uniform or equivalent channel widths to minimise any impact on correlation analyses.

2.8 Research Gap

To the best of our knowledge, existing literature on dividing flow in open-channel has not addressed the V-shaped cross-sectional channel, particularly within the context of mathematical models. However, Zawawi et al. (2019) consider the different width of the channels for the trapezoidal, rectangular and V-shape cross-sectional channel. The current study will be focusing on two cases which are Case 1 and Case 2.

A key innovation of this research is the development of mathematical models for trapezoidal, rectangular and V-shaped cross-sectional channels for two cases in dividing flow through the principle of continuity and momentum principles, enabling a more accurate prediction of discharge distribution between the main and branch channels. Furthermore, this study systematically investigates the impact of Reynold number on the discharge ratio in trapezoidal cross-sectional channel. The flow depth for all type of channels based on certain division angles are analysed.

Most previous studies have focused on discharge ratio in dividing flow often neglecting the complex interactions between flow behavior and specific phenomena such as flow separation. This represents a significant research gap in the field of open-channel flow. In response, the present study introduces a novel mathematical modeling framework that incorporates the presence of a separation zone to estimate dividing flow

in V-shaped channels. By addressing these previously unexplored parameters, this study advances the current understanding of open-channel flow division and provides a foundation for more refined hydraulic design and analysis in natural and engineered channel networks. Table 2.2 presents a scoping review of recent studies on open-channel dividing flow, focusing on the methodologies, key findings and research gaps reported in the literature.

Table 2.2
Summary of Selection Studies on The Open Channel Flow

Author(s) and Year	Shape of the channel	Bifurcation angle	Method	Findings
Hsu et al. (2002)	Rectangular	90°	Experiment	The depth ratio increases as the discharge ratio increase with decreasing Froude number.
Ramamurthy et al. (2007)	Rectangular	90°	RANS & Experiment	The width and length of the separation zone in the branch channel decreases when the discharge ratio Q_r increases.
Shamloo & Pirzadeh (2008)	Rectangular	90°	Reynolds Stress Method (RSM)	The non-dimensionless width and length of separation zone decreases, the discharge ratio Q_r increases.
Zhang et al. (2009)	Rectangular	90°	RANS Model	It is seen that although the size of separation zone decreases with the discharge ratio increases.
Pandey & Mishra (2012)	Rectangular & Trapezoidal	30°, 90°	Mass continuity and momentum principle	Rectangular channel gives higher depth ratio compared to the trapezoidal channel but lower depth ratio for rectangular.
Schindfessel et al. (2017)	Trapezoidal, Rectangular, Circular, Chamfered rectangular	90°	Large eddy simulation (LES)	The shape of the cross-sectional channels significantly influences the separation zone. The geometry of the downstream corner can introduce lateral currents directed into the separation zone.
Sui & Huang (2017)	Rectangular	30°, 60°, 90°	Large eddy simulation (LES)	The length and width of the separation zone increases with the increase of discharge ratio and bifurcation angle. The width of the separation zone constant when the angle of bifurcation increases from 60°

				to $90°$.
Alomari et al. (2018)	Rectangular	$30°, 45°, 60°, 75°, 90°$	Experiment	The results show that when the angle of diversion decreases, the scour depths become smaller.
Pandey & Mohapatra (2019)	Rectangular	$45°$	RANS Model	The increase in discharge ratio leads to a reduction in the length and width of the separation zone. At the intake of $45°$, the length of separation zone is smaller than intake of $90°$.
Sayed (2019)	Rectangular	$45°, 60°, 75°, 90°$	Experiment	The highest discharge ratio is obtained at the angle of $45°$ and the lowest is obtained at angle $90°$.
Zawawi et al. (2019)	Trapezoidal	$0°, 30°, 45°, 60°, 75°, 90°$	Mass continuity and momentum principle	The derived equation examines the discharge ratio with different angles of the bifurcations. Discharge ratio decreased as the off-take angle decreased.
Shahari et al. (2021)	Trapezoidal & V-shaped	$90°$	Mass continuity and momentum principle	The rate of increase of depth flow for the trapezoidal channel is higher than the V-shaped channel as the Froude number and discharge ratio increase.
Cheng et al. (2022)	Trapezoidal	$90°$	The $k-\varepsilon$ turbulence model	A small Froude number, F_r indicating the value of pulsating velocity was large then the existence of the recirculation zone has a narrowing effect on the flow.
Harmizi et al. (2023)	Trapezoidal & Rectangular	$30°, 90°$	Mass continuity and momentum principle	The discharge ratio and Froude number increase, the flow depth in the rectangular channel decreases.

Hassan & Shabat (2023)	Rectangular	$30°, 45°, 60°, 90°$	The $k-\varepsilon$ turbulence model	The result showed that when the discharge ratio increases, the separation zone will decrease.
Sayed Abu-Zaid (2023)	Rectangular	$15°, 30°, 45°, 60°, 75°, 90$	RANS Model	The angle of $15°$ has the optimum impact on the flow rate and the size of the separation zone in the bifurcating channel. When bifurcation angle increase, the separation zone increases.
Zakaria et al. (2025)	Trapezoidal	$0°, 15°, 30°, 45°, 60°, 75°, 90$	3D Navier Stokes Equation	The results shows that when bifurcation angles increase, the discharge ratio decrease. Thus, the width of the separation has a greater impact on discharge ratio compare to the length of the separation zone.

CHAPTER 3
MATHEMATICAL MODELLING OF OPEN-CHANNEL DIVIDING FLOW

3.1 Introduction

The previous chapter reveals that the study on mathematical models in open-channel dividing flow focuses on the trapezoidal and rectangular cross-sectional channels. This chapter primarily addresses the modelling of open-channel dividing flow in the trapezoidal, rectangular, and V-shaped cross-sectional channels, utilising the momentum principle and continuity equation for estimating the discharge ratio. The characteristics and schematic layout of the open-channel dividing flow for each channel will be presented and discussed. Meanwhile, the geometric hydraulic properties for all types of cross-sectional channels will be provided. Finally, the computation of the proposed models and the results of the discharge ratio across a specific division angle will be discussed.

3.2 Description of The Open-Channel Dividing Flow

The dividing flow consists of a main channel that divides into two branch channels at a defined junction point. The channels are assumed to have trapezoidal, rectangular or V-shaped cross-sectional geometry properties, which are representative of many natural and engineered open-channel systems. At the junction point, the main channel splits at a defined dividing angle. which is the angle between the axes of the two branch channels measured relative to the original direction of the flow in the main channel. This division angle plays a significant role in the conceptual foundation and development of the open-channel dividing flow models undertaken in this research. The schematic layout of the open-channel dividing flow channel is illustrated in Figure 3.1, where the main channel is divided into two branch channels, namely channel 1 and channel 2.

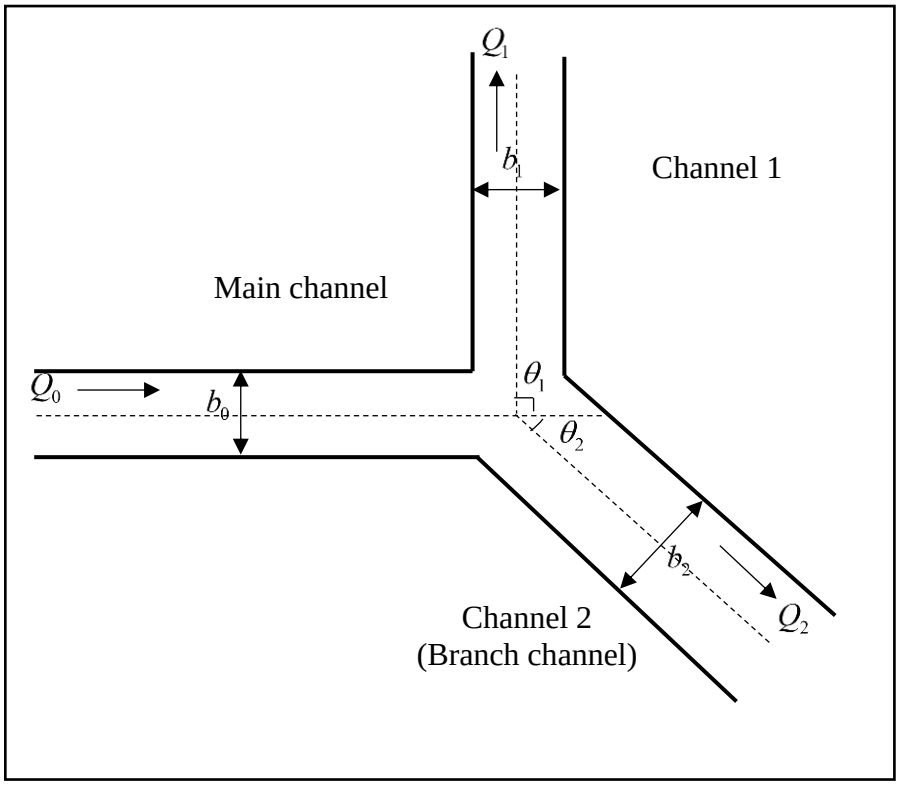


Figure 3.1 Schematic Layout of Open-Channel Dividing Flow

The notation of 0 is main channel (upstream), while 1 and 2 is channel 1 (downstream) and channel 2 (branch channel) respectively. Q is the discharge in each channel, θ_1 and θ_2 are the division angles and b is the bottom width of the channel. The dividing flow from main channel to two branch channels may be determined with aid of momentum principle and mass continuity with the following assumptions:

1) The flow is one-dimensional and steady.
2) All channels are straight in which the cross-sectional shape and size and also the bottom slope is constant (prismatic channel).
3) Main channel is connected to two branch channels.
4) The flow is taking place from main channel to the channel 1 and channel 2.
5) Direction of main channels with respect to the axis of channel 1 and channel 2 are θ_1 and θ_2 respectively.
6) The flow is parallel to channel walls, and the velocity is uniformly distributed immediately above and below the junction.

7) The wall friction is neglected as compared to other forces.
8) The depth of the flow in main channel is equal to the channel 1 and channel 2.

The geometric characteristics of trapezoidal, rectangular and V-shaped cross-sectional channels are presented in Table 3.1, where b is the bottom width of the channel section, a is the side slope value of the channel and y is the flow depth of the water flow (Shahari et al., 2021).

Table 3.1
The Geometric Properties of Cross-Sectional Channel

Properties	**Trapezoidal**	**Rectangular**	**V-shaped**
Cross-sectional area, A	$by + ay^2$	by	ay^2
Wetted perimeter, W_P	$b + 2y\sqrt{1+a^2}$	$b + 2y$	$2y\sqrt{1+a^2}$
Hydraulic radius, H_R	$\frac{by + ay^2}{b + 2y\sqrt{1+a^2}}$	$\frac{by}{b+2y}$	$\frac{ay^2}{2y\sqrt{1+a^2}}$
Top width, T	$b + 2ay$	b	$2ay$

3.3 Mathematical modelling of open-channel dividing flow

For one-dimensional, steady, incompressible flow in an open-channel, the continuity equation is expressed as (Gąsiorowski & Artichowicz, 2019):

$$\frac{dQ}{dx} = 0$$

where Q is the discharge (m^3/s) and x is the longitudinal coordinate along the channel (m). In the context of dividing flow, the total inflow in the main channel can be determined as follows:

$$Q_0 = Q_1 + Q_2 \tag{3.1}$$

where $Q_0 = A_0V_0, Q_1 = A_1V_1,$ and $Q_2 = A_2V_2$ are discharges in the main channel, channel after junction and branch channel respectively. For each channel, these equations state that the discharge, Q is equivalent to the product of the channel velocity, V and area of the

flow, A. While it is possible to estimate or survey the channel shape, it may not be as practical to manually or physically measure the flow velocity.

The following information are required to determine the geometric hydraulic properties (GHP) and solve the open channel dividing flow equations:

a) Hydraulic radius, $H_R = \frac{A}{W_P}$, where A is area while W_P is the wetted perimeter.

b) Hydraulic depth, $D = \frac{A}{T}$, where T is top width of the channel.

c) From (2.2), the Manning's equation is $V = \frac{1}{n} H_R^{2/3} S^{1/2}$, where $n = 0.03$, is the Manning's roughness coefficient for the main channel (The surface type is assumed to be earth channel based on Table 2.1 by Jamal & Md Ali (2023)), V is the cross-sectional average velocity or mean velocity of flow in meter (m) per second (ms^{-1}), R_h is hydraulic radius in meter (Area of the flow section per wetted perimeter, W_P of flow in channel), S is the slope of the channel in meter (vertical) per foot (horizontal).

d) From (2.1), Froude number in the main channel is $F_0 = \frac{V}{\sqrt{gD}}$, where g is gravity. The value of $g = 9.80665 m/s^2$. This index classifies water flow; specifically, a low Froude number indicates deep, slow flow, whereas a high Froude number signifies shallow, rapid flow. Froude number for each of the cross-sectional channels are different since the hydraulic depth are not the same, yet the velocity and gravity are same for different shapes of the cross-sectional channel.

e) The flow depth for all the branches of each shape is, $y = 3.5m$.

The behaviour of fluids in open-channel systems is defined by the core concepts of mass, momentum, and energy conservation. As the dividing of open channel flow model is an application of fluid dynamics, the momentum principle used is slightly different from classical physics. Momentum is usually a product of mass and velocity. In the open channel flow model, the momentum conservation principle accounts for the balance of forces acting on a fluid element, generally known as the product of mass discharge and velocity. In this study, the general equation of momentum principle is given as follows:

$$-\rho QV_1 + \rho QV_2 = \bar{P}_1 A_1 - \bar{P}_2 A_2 \tag{3.2}$$

The terms of where ρ is the fluid density (density of water) and $\bar{P}$ is the average pressure. By applying the momentum principle (3.2) and mass continuity (3.1) in the flow direction of the main channel, the following equation is obtained:

$$P_0 - P_2 \cos\theta_2 - P_1 \cos\theta_1 - \Delta P = \frac{\gamma}{g}\left(Q_1 V_1 \cos\theta_1 + Q_2 V_2 \cos\theta_2 - Q_0 V_0\right) + U_1 + U_2 \tag{3.3}$$

where P is the pressure force, Q is the discharge in channel, V is the flow velocity, ΔP is a difference between the pressure force at the branch channel on the main channel and the pressure force right before that, U_1 and U_2 are the momentum transfer from the main channel to branch channel, which can be written as:

$$U_1 = \rho Q_1 V_0 C \sin\theta_1,\ U_2 = \rho Q_2 V_0 C \sin\theta_2$$

3.3.1 Trapezoidal cross-sectional channel

A trapezoidal cross-sectional channel is one of the most used geometries in open-channel flow. This trapezoidal consists of flat bottom of width, b and two sloped sides that rise from the base at angle determined by the side slope ratio, a, which is defined as the horizontal distance per unit vertical rise (a:1). It also consists of top width, T, and depth of flow, y. Figure 3.2 illustrates the diagram of trapezoidal shape of cross-sectional channel.

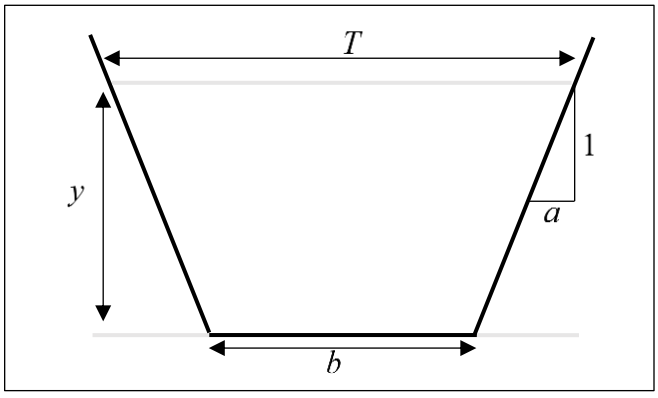


Figure 3.2 Diagram of Trapezoidal Cross-Sectional Channel

The general equation of open-channel dividing flow in trapezoidal cross-sectional channel (OCDF-T) is given as follows Zawawi et al. (2019):

$$\left(1+2k_0\right)\left[\frac{1}{2}\left(1-y_r^{\,2}-Br_1y_r^{\,2}\cos\theta_1\right)+\frac{k_0}{3}\left(1-y_r^{\,3}-y_r^{\,3}\cos\theta_1\right)\right]$$
$$=F_0^2\left(1+k_0\right)^2\left[C\left(q_r\sin\theta_1+\left(1-q_r\right)\sin\theta_2\right)+\frac{1+k_0}{y_r}\left(\frac{\left(1-q_r\right)^2}{Br_2+k_0y_r}\cos\theta_2+\frac{q_r^{\,2}}{Br_1+k_0y_r}\cos\theta_1\right)_1-1\right]. \quad (3.4)$$

where k_0 is the side slope/flow depth to bottom width ratio, y_r is the flow depth ratio, B_r is the width ratio, F_0 is the Froude number, q_r is the discharge ratio, and C is constant. It can be observed that (3.4) is slightly different from (2.2) in terms of the power of the flow depth ratio, y_r in the left-hand side of the equation.

3.3.2 Rectangular Cross-Sectional Channel

A rectangular cross-sectional channel is the most basic and widely studied geometry in open-channel flow. Its geometric details consist of top width, T, depth of flow, y, and horizontal flat bottom of constant width, b with vertical side walls, creating a uniform cross-section along the channel's length. This simple geometry is commonly used in urban drainage systems and some engineered irrigation. Figure 3.3 shows the typical rectangular cross-sectional channel.

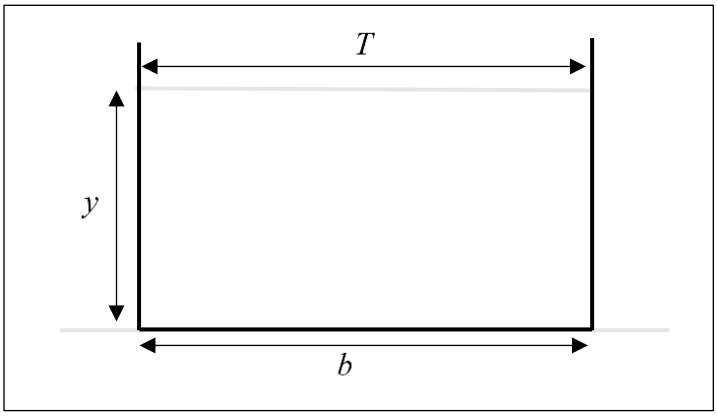


Figure 3.3 Diagram of Rectangular Cross-Sectional Channel

By substituting $k_0 = 0$ into (3.4), the general equation of open-channel dividing flow in the rectangular channel (OCDF-R) is obtained as follows:

$$\frac{1}{2}\left(1 - y_r^{\,2} - Br_1 y_r^{\,2}\cos\theta_1\right) = F_0^2\left[C\left(q_r\sin\theta_1 + \left(1-q_r\right)\sin\theta_2\right) + \frac{1}{y_r}\left(\frac{\left(1-q_r\right)^2}{Br_2}\cos\theta_2 + \frac{q_r^{\,2}}{Br_1}\cos\theta_1\right) - 1\right]. \qquad (3.5)$$

where y_r is the flow depth ratio, B_r is the width ratio, F_0 is the Froude number, q_r is the discharge ratio and C is constant. The rectangular channel serves as a standard case for the validation of numerical models or experimental data and may not be ideal in natural settings due to its instability of vertical side walls.

3.3.3 V-shaped Cross-Sectional Channel

A V-shaped cross-sectional channel is characterized by two inclined side slopes meeting at a sharp vertex, forming a symmetrical triangular geometry. Unlike rectangular or trapezoidal channels, the V-shaped channel does not have a flat bottom; instead, the channel bed forms a continuous incline, typically defined by a single side slope ratio a which expresses the horizontal projection per unit vertical rise (i.e., a :1) on each side. This configuration is frequently observed in natural drainage paths, mountainous streams, and constructed channels where rapid concentration and conveyance of flow are desired. The shape of V-shaped cross-sectional is illustrated in Figure 3.4 where the geometric details of the cross-sectional are side slope of the channel, a, top width, T, depth of flow, y.

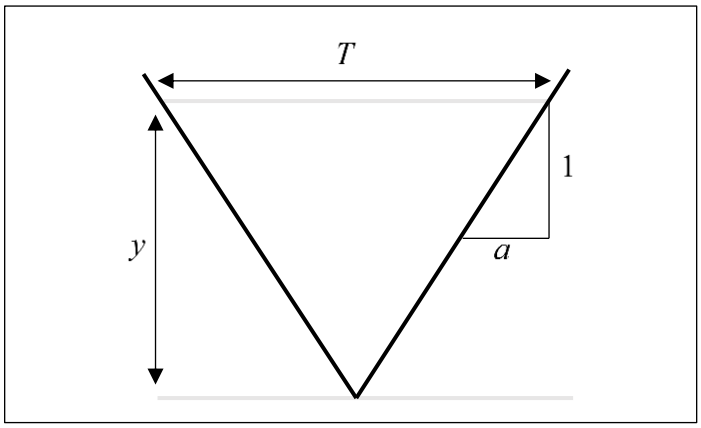


Figure 3.4 Diagram of V-Shaped Cross-Sectional Channel

In this section, the general equation of dividing flow in V-shaped cross-sectional channel will be derived. The hydrostatic force, which is one of the important characteristics to derive the open-channel flow model, can be defined by the pressure applied at a stationary fluid on any surface in contact with it. The pressure of a fluid is contingent upon its depth, density, and gravitational acceleration. In open channels flow, hydrostatic forces influence the pressure distribution, affecting flow characteristics, slope stability, and channel design. Based on Table 3.1, the total of hydrostatic force for the V-shaped is determined as follows:

$$P = \gamma \int_0^y ay^2 dy = \gamma \left[\frac{ay^3}{3} \right]_0^y = \gamma \left(\frac{ay^3}{3} \right). \tag{3.6}$$

where $C = \frac{5}{6} - \frac{F_0^{\,2}}{40}$. From the LHS of (3.3),

$$P_0 - P_2 \cos\theta_2 - P_1 \cos\theta_1 - \Delta P \tag{3.7}$$

where $\Delta P = \gamma \left(\frac{ay_2^{\,3}}{y^3} \right) - P_2 \cos\theta_2$ and equation (3.6) are substituted into (3.7)

$$\gamma \left[\left(\frac{ay_0^{\,3}}{3} \right) - \left(\frac{ay_2^{\,3}}{3} \right) \cos\theta_2 - \left(\frac{ay_1^{\,3}}{3} \right) \cos\theta_1 - \left(\frac{ay_2^{\,3}}{3} \right) + \left(\frac{ay_2^{\,3}}{3} \right) \cos\theta_2 \right]$$

$$\gamma\left[\left(\frac{ay_0{}^3}{3}\right)-\left(\frac{ay_1{}^3}{3}\right)\cos\theta_1-\left(\frac{ay_2{}^3}{3}\right)\right] \tag{3.8}$$

Expand, simplify, and factorise (3.8) into

$$\gamma\frac{a}{3}\left[y_0{}^3-y_1{}^3\cos\theta_1-y_2{}^3\right] \tag{3.9}$$

Next, the RHS from (3.3) by substituting the U_1 and U_2 into the following equation,

$$\frac{\gamma}{g}\left(Q_2V_2\cos\theta_2+Q_1V_1\cos\theta_1-Q_0V_0\right)+\rho Q_1V_0C\sin\theta_1+\rho Q_2V_0C\sin\theta_2 \tag{3.10}$$

Based on (3.1), expression (3.10) turns into the following form:

$$\frac{\gamma}{g}\left[\frac{Q_2Q_2}{A_2}\cos\theta_2+\frac{Q_1Q_1}{A_1}\cos\theta_1-\frac{Q_0Q_0}{A_0}+\frac{Q_1Q_0}{A_0}C\sin\theta_1+\frac{Q_2Q_0}{A_0}C\sin\theta_2\right] \tag{3.11}$$

Factorise (3.11) with $\frac{Q_0{}^2}{A_0}$, resulting in

$$\frac{\gamma}{g}\frac{Q_0{}^2}{A_0}\left[\frac{1}{Q_0{}^2}\frac{Q_2{}^2}{A_2/A_0}\cos\theta_2+\frac{1}{Q_0{}^2}\frac{Q_1{}^2}{A_1/A_0}\cos\theta_1-1+C\left[\frac{Q_1}{Q_0}\sin\theta_1+\frac{Q_2}{Q_0}\sin\theta_2\right]\right] \tag{3.12}$$

The discharge ratio is given as

$$q_r=\frac{Q_1}{Q_2}\ \text{where}\ Q_1=Q_0q_r\,.$$

Modify (3.1) into $Q_0=Q_0q_r+Q_2$ and $\frac{Q_2}{Q_0}=1-q_r$. Thus, (3.12) will become

$$\frac{\gamma}{g}\frac{Q_0{}^2}{A_0}\left[\frac{\left(1-q_r\right)^2}{A_2/A_0}\cos\theta_2+\frac{q_r{}^2}{A_1/A_0}\cos\theta_1-1+C\left[q_r\sin\theta_1+\left(1-q_r\right)\sin\theta_2\right]\right] \tag{3.13}$$

From the Froude number in Zawawi et al. (2019),

$$F_0 = \frac{Q}{A_0\sqrt{g\left(\frac{A_0}{T_0}\right)}} \tag{3.14}$$

$\frac{Q_0^{\,2}}{A_0 g}$ in (3.13) turn into the Froude number by using (3.14) to determine the type of flow of the channel.

$$F_0 = \frac{Q_0}{A_0\sqrt{g\left(\frac{A_0}{T_0}\right)}}$$

$F_0 A_0\sqrt{g\left(\frac{A_0}{T_0}\right)} = Q_0$, squared both sides of the equation

$$F_0^{\,2} A_0^{\,2} g\left(\frac{A_0}{T_0}\right) = Q_0^{\,2}$$

$$F_0^{\,2}\frac{A_0}{T_0} = \frac{Q_0^{\,2}}{A_0^{\,2} g} \tag{3.15}$$

The area and top width from the left-hand side in (3.15) are expend according to the channel and produce (3.16) where $A = ay^2$ and $T = 2ay$.

$$F_0^{\,2}\frac{ay_0^{\,3}}{2} \tag{3.16}$$

The following procedure is required to obtain y_r in V-shape.

$$\frac{A_2}{A_0} = \frac{ay_2^{\,2}}{ay_0^{\,2}}, \frac{A_1}{A_0} = \frac{ay_1^{\,2}}{ay_0^{\,2}} = y_r^{\,2} \tag{3.17}$$

Next, substitute (3.16) and (3.17) into (3.13), yields

$$\gamma F_0^{\,2}\,\frac{a y_0^{\,3}}{2}\left[\frac{1}{y_r^{\,2}}\left(\left(1-q_r\right)^2\cos\theta_2+q_r^{\,2}\cos\theta_1\right)-1+C\left(q_r\sin\theta_1+\left(1-q_r\right)\sin\theta_2\right)\right] \qquad (3.18)$$

Then, (3.9) is equal to (3.18) to become a complete equation for V-shape cross-sectional channel

$$\gamma\frac{a}{3}\left[y_0^{\,3}-y_1^{\,3}\cos\theta_1-y_2^{\,3}\right]$$
$$=\gamma F_0^{\,2}\,\frac{a y_0^{\,3}}{2}\left[\frac{1}{y_r^{\,2}}\left(\left(1-q_r\right)^2\cos\theta_2+q_r^{\,2}\cos\theta_1\right)-1+C\left(q_r\sin\theta_1+\left(1-q_r\right)\sin\theta_2\right)\right]$$

$$\left(\frac{a}{3}\times\frac{2}{a y_0^{\,3}}\right)\left[y_0^{\,3}-y_1^{\,3}\cos\theta_1-y_2^{\,3}\right]$$
$$=F_0^{\,2}\left[\frac{1}{y_r^{\,2}}\left(\left(1-q_r\right)^2\cos\theta_2+q_r^{\,2}\cos\theta_1\right)-1+C\left(q_r\sin\theta_1+\left(1-q_r\right)\sin\theta_2\right)\right]$$

$$\left(\frac{2}{3y_0^{\,3}}\right)\left[y_0^{\,3}-y_1^{\,3}\cos\theta_1-y_2^{\,3}\right]$$
$$=F_0^{\,2}\left[\frac{1}{y_r^{\,2}}\left(\left(1-q_r\right)^2\cos\theta_2+q_r^{\,2}\cos\theta_1\right)-1+C\left(q_r\sin\theta_1+\left(1-q_r\right)\sin\theta_2\right)\right]$$

After applying algebraic manipulation, ratio principle and some simplification techniques, the mathematical model of open-channel dividing flow in V-shaped cross-sectional channel (OCDF-V) is obtained as follows:

$$\frac{2}{3}\left[1-y_r^{\,3}-y_r^{\,3}\cos\theta_1\right]$$
$$=F_0^{\,2}\left[\frac{1}{y_r^{\,2}}\left(\left(1-q_r\right)^2\cos\theta_2+q_r^{\,2}\cos\theta_1\right)-1+C\left(q_r\sin\theta_1+\left(1-q_r\right)\sin\theta_2\right)\right] \qquad (3.19)$$

where y_r is the flow depth ratio, F_0 is the Froude number, q_r is the discharge ratio, C is constant, and $C=\frac{5}{6}-\frac{F_0^{\,2}}{40}$ is a momentum correction factor to account for non-uniform velocity distribution. This coefficient is analogous to the Boussinesq coefficient, commonly used in open-channel flow theory.

3.4 Geometric and Hydraulic Properties

The analysis of open-channel flow relies heavily on the geometric and hydraulic properties (GHP) of the channels. These properties govern how water is conveyed through a channel and describe flow behavior under various conditions. Tables 3.2 to 3.4 show the GHP of trapezoidal, rectangular and V-shaped cross-sectional channels respectively, which have been used in this study for computing the discharge ratio. For branch channel 2, Case 1 is considered as constant width of the channel, whereas Case 2 investigates the different width of the channel.

Table 3.2
Geometric Hydraulic Properties for Trapezoidal Cross-Sectional Channel

GHP	Main channel	Branch channel 1	Branch channel 2	
			Case 1	Case 2
a	4.081632657	4.081632657m	4.081632657m	0.859291082m
T	300m	300m	300m	60.15037595m
b	271.285714	271.285714m	271.285714m	54.13533835m
A	1000m^2	1000m^2	1000m^2	200m^2
λ	14.70821651m	14.70821651m	14.70821651m	4.614668923m
W_P	300.8450044m	300.8450044m	300.8450044m	63.3646762m
H_R	3.323970767m	3.323970767m	3.323970767m	3.156332708m
D	3.33m	3.33m	3.33m	3.325m

Table 3.3
Geometric Hydraulic Properties for Rectangular Cross-Sectional Channel

GHP	Main channel	Branch channel 1	Branch channel 2	
			Case 1	Case 2
T/b	285.7142857	285.7142857	285.7142857	57.14285714
W_P	292.7142857	292.7142857	292.7142857	64.14285714
H_R	3.416300634	3.416300634	3.416300634	3.118040089
D	3.5	3.5	3.5	3.5

Table 3.4
Geometric Hydraulic Properties for V-Shaped Cross-Sectional Channel

GHP	Main channel	Branch channel 1	Branch channel 2	
			Case 1	Case 2
a	81.63265306	81.63265306	81.63265306	16.32653061
T	571.4285714	571.4285714	571.4285714	114.2857143
λ	285.7204106	285.7204106	285.7204106	57.24994430
W_P	571.4714448	571.4714448	571.4714448	114.4998886
H_R	1.74986871	1.74986871	1.74986871	1.746726590
D	1.75	1.75	1.75	1.75

3.5 Setting Up The Model Computation

A graphical user interface (GUI) is a software interface that employs windows, icons and menus, which can be operated by a mouse to create dynamic interactive documents applicable in various fields such as business or education applications. The basic GUI consists of worksheet interfaces that execute tedious computations and manipulate mathematical expressions by solving complex mathematical problems from mathematics, science, and engineering. Recent studies have emphasized the advantages of several popular technology tools that are widely used in mathematics education and scientific research. Putra et al. (2024) discussed the creation of an educational tool using MATLAB graphical user interface (GUI) to improve students' mathematical connection abilities. Other studies used Maple software to determine the analytical solutions for the current flowing in the different branches of the electronic circuit, derive analytical expressions for the terminal voltages of all the elements of the circuit, calculate the dynamic resistances diodes of the circuit, and animate graphic representations to study the influence of certain parameters on the current and the voltages at the terminals of all the elements of the circuit (El Aydi et al., 2020). Although current research recognises the significance of technology in problem-solving, enquiries regarding the integration of digital tools into mathematical modelling remain unresolved. Therefore, this chapter demonstrates the utilization and usability of Maple software for interactive mathematical modeling of open-channel dividing flow.

3.5.1 Maple Application

Maple is a modern, interactive, and customized software that has the potential to significantly enhance application usage in a dynamic user-friendly environment. This software is built to help students, mathematicians, engineers, scientists, educators, and researchers visualize calculations, analyze logical modelling, and solve mathematical problems in various fields, such as algebra, calculus, differential equations, and linear algebra, among others.

The viewpoint of the Maple application includes not only mathematical interest but also taking into account the numerous needs of users. To the best of our knowledge, this interactive application offers valuable insights for comprehending river flow and aids engineers and authorities in properly designing river bifurcations. Therefore, this section introduces Maple's Math Apps as an innovative, effective, and pragmatic method to mathematical modelling, which has been extensively employed to estimate the discharge ratio in open-channel dividing flow. Math Apps is employed to create a custom interactive user interface where users can enter values for variables and see real-time results. This application uses interactive features and visualization that can manipulate the inputs such as mathematical expressions and instantly demonstrate the outputs. The request sending by user to Maple is called Maple input, and the resultant output is referred to as Maple output. The input and output constitute an execution group, which is the essential component of the worksheet. The procedure to set up the Math Apps for this research is:

i) Define variables by simply assigning them values using := command.
ii) Maple's symbolic algebra functions is performed
iii) Use fsolve or similar functions to solve numerically.

For specific applications such as hydraulic modelling, a series of steps to input parameters, perform calculations, and solve equations are defined. The following steps show the computation of the OCDF-V model.

Step 1: Define Parameters:

Input variables or constants needed for your specific model.

```
>T1 := theta1;
>T2 := theta2;
```

>yr := flow depth ratio;

>Q := discharge ratio;

>a0 := slope channel0;

>a1 := slope channel1;

>a2 := slope channel2;

Step 2: Define equations using Maple's mathematical functions. For example:

>FR := (2/3 * (1 - yr^3 - yr^3* cos(T2)) = F0^2 * ((1/yr^2) * (1-Q)^2 * cos(T2) + Q^2 * cos(T1)) - 1 + C * ((1 - Q) * sin(T2) + Q * sin(T1)));

Step 3: Use solve or fsolve to find the solutions.

>FLR := solve(FR, [Q]);

Step 4: After solving the equations, perform any additional computations.

>rh0 := A0/P;

>v := rh0^(2/3) * S0^(1/2) / n;

>F0 := v/sqrt(9.80665*d)

Step 5: Use printf, display, or plot to visualize and display results.

>printf("The Flow Rate Ratio is: %s", FLR);

>plot([f(x)], x = -10 .. 10);

3.5.2 Developing Interactive Math Apps

Maple also allows you to create interactive applications using MapleSim or Interactive Tools to allow users to manipulate variables and immediately see the effect on the solution.

Define Parameters as Sliders (interactive widgets) for variable adjustment.

>with(plots):

>slider := Slider([x=0..10, increment=0.1, value=5]);

>plot([sin(x)], x = 0..10);

Maple Application Builder is employed for computing the discharge ratio as shown in Figure 3.5.

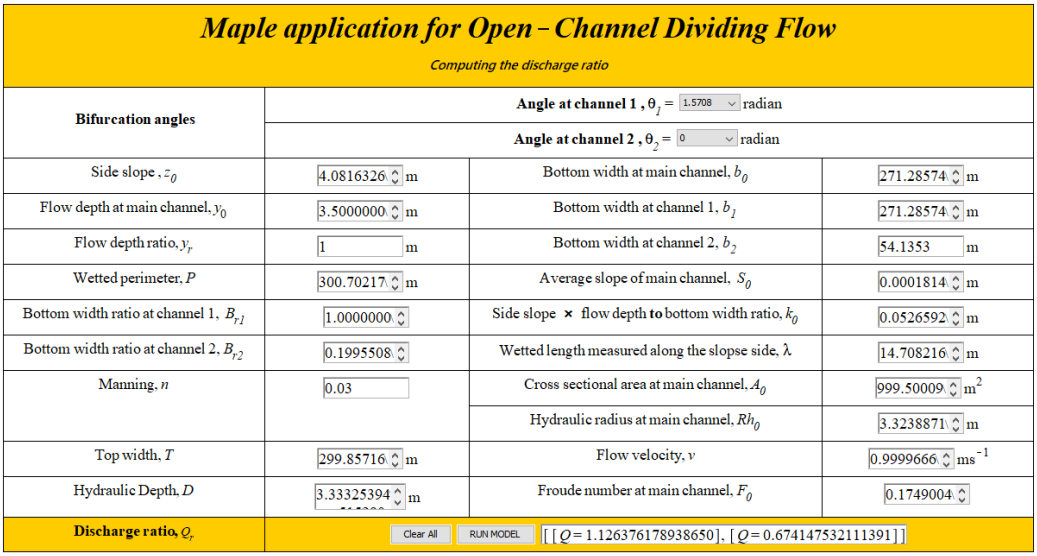


Figure 3.5 Maple's Math Apps for Computing The Discharge Ratio in Open-Channel Dividing Flow

In Figure 3.5, the Math Apps in Maple software is employed to develop the GUI for the mathematical model in order to determine the amount of river flowrate with some important parameters. The application will be divided into two parts which are the input value of the data and the output of the behavior of water flow. The first part is a platform that allows the user to manually input the values of all the domain data. The input button functions that will be used in this study are bottom width, Froude number, bifurcation or division angles, shape of the cross-sectional channel and equation of dividing flow. Select one of the listed options from the drop-down menu in combo box to change the bifurcation angles. Fill up the entry boxes or text area for the bottom widths, side slope, flow depth, flow depth ratio, Manning's number and average slope of channel. The other parameters will be updated automatically when the value changes. Click the "Run Model" button to perform an action, that is, execute code. A series of variables and performing computations are defined in the "Run Model" button. A method called Do is used to assign values to variables, and related equations are set up to calculate parameters such as flow rate, velocity, hydraulic depth, Froude number and others. The script is defining relationships

between variables such as depth (y0), slope (S0), wetted perimeter (P), and bottom ratios (br1, br2), among others. The last block of code (the Do block) is used to store the final computed results in specific variables. A summary of key components used in this Math Apps is as follows:

i. Initial definitions: Define a series of variables using Do (e.g., t1, t2, b0, b1, b2, etc.).
ii. Relations between parameters: Several computed relationships are defined between parameters (such as the Froude number F0, hydraulic radius rh0, velocity v, etc.).
iii. Equations for discharge or flow rate (FR) and flow rate ratio (FLR): The equation for the flow rate ratio (FR) is given as a complex formula that involves several parameters like slope, depth, and the Manning's roughness coefficient. The solve function is used to solve for the flow rate ratio Q based on the equation FR.
iv. Final variable assignment: After calculations, the results are reassigned to the corresponding input variables with the Do function.

3.6 Results Analysis

In this study, the Maple software will be utilised as mathematical tools for computing the models (3.4), (3.5) and (3.18). The division angles used in channel 1 (θ_1) and channel 2 (θ_2) are $0°, 15°, 30°, 45°, 60°, 75°$ and $90°$. The discharge in the main channel is assumed to be $Q_0 = 1000 m^3 / s$ for two cases, while Q_1 and Q_2 are discharges in branch channel 1 and channel 2 respectively. The critical discharge ratio, which represents theoretical threshold or limiting value is assumed to be 0.8 for all cross-sectional channels (Zawawi et al., 2019). This value distinguishes between different flow regimes or behaviors. If the discharge ratio exceeds this value, it may lead to instability or overflow in branch channel 2. The Froude number of the main channel is a subcritical flow, in which the value is less than one. To determine the discharge ratio, the GHP from Tables 3.2-3.4 are utilised.

This section discusses the relationship between discharge ratio and division angles for the trapezoidal, rectangular, and V-shaped cross-sectional channels. Since the models are in the form of non-linear polynomials of degree 3, they have exactly 3 roots, which are real or/and complex roots (see appendix 1-21). However, solutions are expected to be real and positive because discharge represents physical quantity. For hydraulic analysis purposes, the real solution or real part of the complex solution is meaningful and valid to be the discharge ratio, which must fall within the range of 0.1 to 1. Any value outside this range implies an inconsistency with physical interpretation or invalid results.

3.6.1 Discharge Ratio in Trapezoidal Cross-Sectional Channel

The discharge ratio with varying division angles for the trapezoidal cross-sectional channels is presented in Tables 3.5. From table, it can be seen that the discharge ratio for case 1 is less than the critical discharge ratio for all division angles. For case 2, the discharge ratio is greater than the critical discharge ratio when the angles are $\theta_1 = 0°, 15°, 30°, 45$ and $60°$. The discharge ratio is less than the critical discharge ratio when the angles $\theta_2 = 60°, 75°$ and $90°$.

Table 3.5

The Discharge Ratio for Trapezoidal Channel for Case 1 And Case 2

θ_2	Case	Discharge ratio, q_r						
		θ_1						
		0°	15°	30°	45°	60°	75°	90°
0°	1	0.5000000000	0.5461054114	0.5755808979	0.5865540452	0.5735640691	0.5249051775	0.4161511761
	2	0.8067160848	0.8226382348	0.8283452301	0.8213342498	0.7927343687	0.7124608934	0.4161443710
15°	1	0.4538613814	0.4999656320	0.5274728248	0.5340995931	0.5133969807	0.4515365724	0.3192880683
	2	0.7911013937	0.8066871059	0.8109839965	0.8009719983	0.7662873548	0.6716673110	0.3192795235
30°	1	0.4243553313	0.4724229022	0.4999265413	0.5041908116	0.4774402349	0.4023784604	0.2401870884
	2	0.7868614482	0.8026398125	0.8066540658	0.7956266293	0.7582042246	0.6545505153	0.2401765844
45°	1	0.4133558446	0.4657604019	0.4956158083	0.4998734439	0.4688619674	0.3793144587	0.1722403341
	2	0.7948174697	0.8113592294	0.8163584990	0.8066091456	0.7704568039	0.6644960296	0.1722262016
60°	1	0.4263250903	0.4864225730	0.5223064984	0.5308048678	0.4997810924	0.3956360764	0.1112713479

	2	0.8158835905	0.8338330477	0.8413532061	0.8358169980	0.8065310627	0.7096814712	0.1112506317
75°	1	0.4749700466	0.5482096464	0.5972420592	0.6201773408	0.6037020813	0.4995228164	0.0542697543
	2	0.8508949019	0.8709907424	0.8829582015	0.8855863895	0.8716262437	0.8063134411	0.05422717560
90°	1	0.0007903002	0.1449569681	0.2458732068	0.2953691295	0.2751390988	0.06638769415	0.5130667561
	2	0.674147370	0.7029950944	0.7163498259	0.7129924603	0.6835953375	0.5842975764	0.8197818834

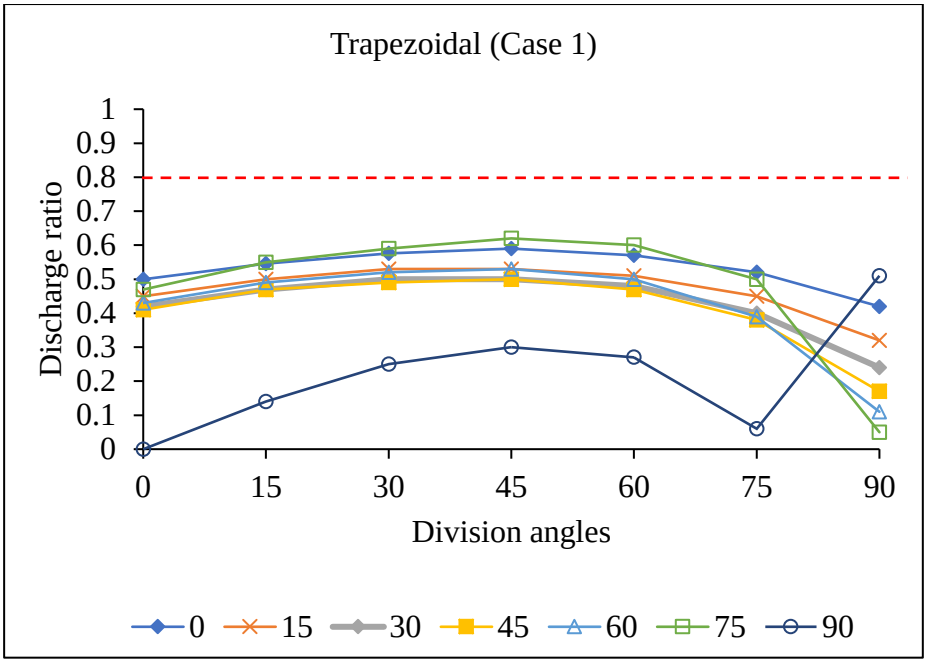


Figure 3.6 Graph of The Discharge Ratio Against Division Angles for The Trapezoidal Channel (Case 1)

Figure 3.6 shows the graph of discharge ratio, q_r against division angles, θ_2 when angles, θ_1 from 0^0 to 90^0 for trapezoidal in Case 1. The horizontal dashed line in the graph represents the critical discharge ratio. There is smallest or no discharge ratio when $\theta_1 = 0^0$ and $\theta_2 = 0^0$. However, it can be seen that all division angles for the trapezoidal are less than the critical line. Hence, the Case 1 for trapezoidal channel contribute to many division angles that able to mitigate the channel from overflow.

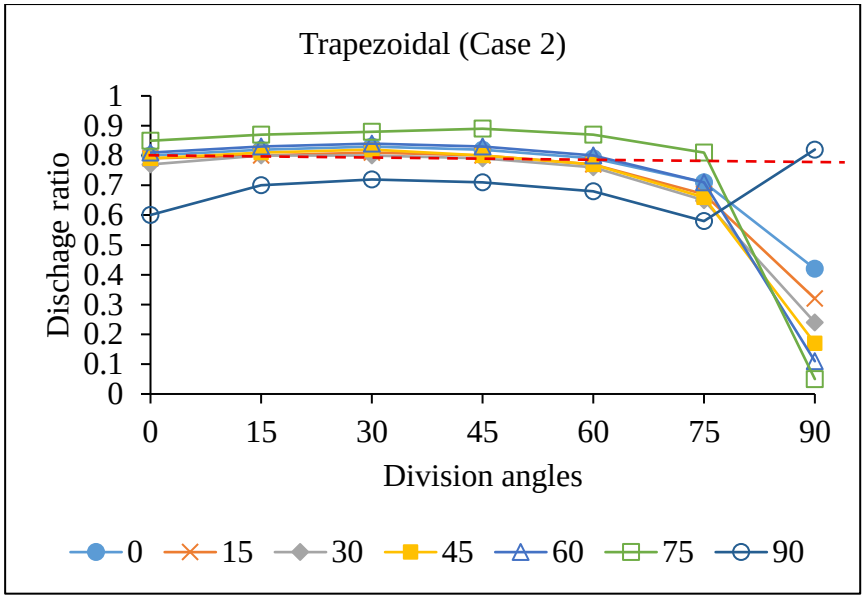


Figure 3.7 Graph of The Discharge Ratio Against Division Angles for The Trapezoidal Channel (Case 2)

Figure 3.7 shows the graph of discharge ratio, q_r against bifurcation angles, θ_2 when angles, θ_1 from 0^0 to 90^0 for trapezoidal in Case 2. For $\theta_1 = 0^0, 15^0, 30^0, 45^0, 60^0$, the discharge ratio approaches to the critical ratio except when $\theta_2 = 75^0, 90^0$. If $\theta_1 = 75^0$, the discharge ratio exceeds the critical ratio and approaches it when $\theta_2 = 75^0$. Hence, it is obvious that division angles for the Case 2 of trapezoidal channel are less than the critical ratio when $\theta_1 = 90^0$ or with any division angles except at $\theta_2 = 90^0$.

3.6.2 Discharge Ratio in Rectangular Cross-Sectional Channel

The discharge ratio for the rectangular cross-sectional channels is presented in Tables 3.6. The discharge ratio for case 1 is less than the critical discharge ratio for all division angles. For case 2, the discharge ratio is greater than the critical discharge ratio for all division angles except when $\theta_2 = 90^0$.

Table 3.6

The Discharge Ratio for Rectangular Channel for Case 1 And Case 2

θ_2	Case	Discharge ratio, q_r						
		θ_1						
		0°	15°	30°	45°	60°	75°	90°
0°	1	0.5000000000	0.5461392314	0.5756459162	0.5866460837	0.5736775976	0.5250335256	0.4162867882
	2	0.8333333334	0.8469445738	0.8514377717	0.8444196963	0.8172901037	0.7393746843	0.4162782116
15°	1	0.4538607686	0.5000000000	0.5275394241	0.5341940785	0.5135136142	0.4516684284	0.3194272727
	2	0.8200330548	0.8333333333	0.8365716767	0.8268763138	0.7942384322	0.7028482116	0.3194165895
30°	1	0.4243540838	0.4724605759	0.5000000000	0.5042952108	0.4775692291	0.4025244005	0.2403412429
	2	0.8168828573	0.8303221901	0.8333333334	0.8228333108	0.7879829499	0.6888738901	0.2403280768
45°	1	0.4133539163	0.4658059215	0.4957047892	0.5000000000	0.4690185245	0.3794919222	0.1724282626
	2	0.8245228246	0.8385829933	0.8425082971	0.8333333333	0.8001464023	0.7004964995	0.1724105783
60°	1	0.4263224024	0.4864863858	0.5224307709	0.5309814755	0.5000000000	0.3958853704	0.1115372099

	2	0.8435426343	0.8587571813	0.8649370981	0.8597075049	0.8333333333	0.7444868412	0.1115111007
75°	1	0.4749664744	0.5483315716	0.5974755995	0.6205080778	0.6041146296	0.5000000000	0.05479141481
	2	0.8743213990	0.8912876210	0.9013332628	0.9033932006	0.8911110804	0.8333333333	0.05473775213
90°	1	0.0000000000	0.1557591447	0.2584984950	0.3112438390	0.2990413770	0.1388977580	0.5000000000
	2	0.7156730271	0.7392383863	0.7494721822	0.7451473040	0.7178992463	0.6291173744	0.8333333333

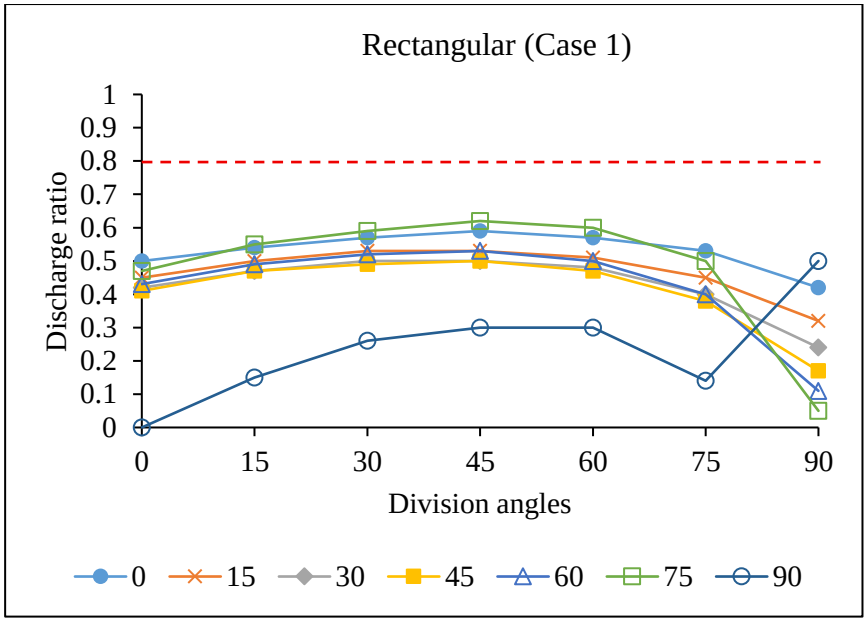


Figure 3.8 Graph of The Discharge Ratio Against Division Angles for The Rectangular Channel (Case 1)

Figure 3.8 shows the graph of discharge ratio, q_r against division angles, θ_2 when angles, θ_1 from 0^0 to 90^0 for rectangular in Case 1. If the division angles, $\theta_1 = \theta_2 = 0^0, 15^0, 30^0, 45^0.60^0, 75^0, 90^0$, the discharge ratio is below the critical ratio. Therefore, the discharge ratio increases and approach to the critical ratio when $\theta_1 = 90^0$.

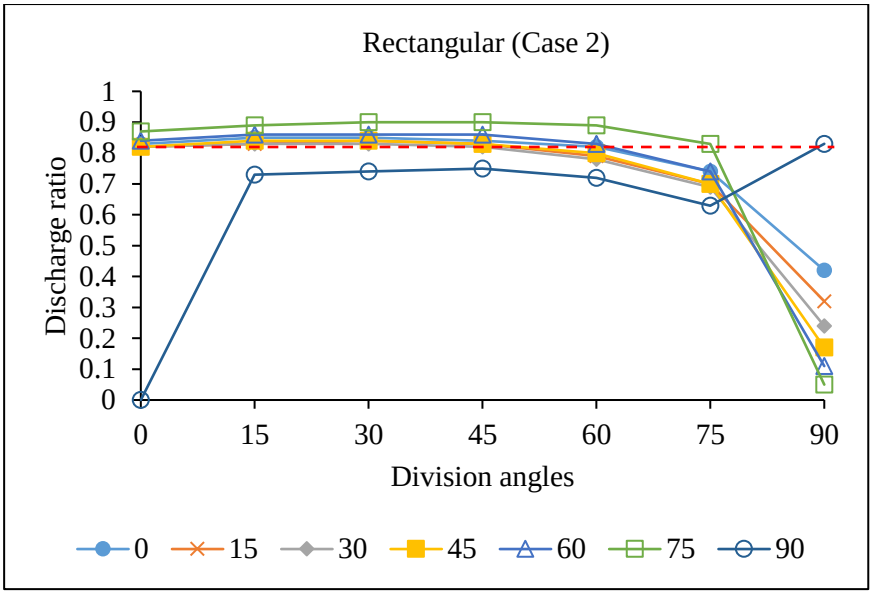


Figure 3.9 Graph of The Discharge Ratio Against Division Angles for The Rectangular Channel (Case 2)

Figure 3.9 shows the graph of discharge ratio, q_r against division angles, θ_2 when angles, θ_1 from 0^0 to 90^0 for rectangular in Case 2. The critical discharge ratio or critical line in the graph is 0.8. It is observed that when $\theta_1 = 0^0, 15^0, 30^0, 45^0, 60^0$, the discharge ratio approaches the critical discharge ratio except when $\theta_2 = 75^0, 90^0$. When $\theta_1 = 75^0$, the discharge ratio is above the critical discharge ratio for all division angles except when $\theta_2 = 90^0$.

3.6.3 Discharge Ratio in V-Shaped Cross-Sectional Channel

The discharge ratio for the V-shaped cross-sectional channels is presented in Tables 3.7. Table shows that the discharge ratio for case 1 and case 2 is less than the critical discharge ratio for all division angles except when case 1 is $\theta_2 = 90°$.

Table 3.7

The Discharge Ratio for V-Shape Channel for Case 1 and Case 2

θ_2	Case	Discharge ratio, q_r						
		θ_1						
		0°	15°	30°	45°	60°	75°	90°
0°	1	0.5000000000	0.5461481972	0.5756641641	0.5866742924	0.5737169162	0.5250857823	0.00000000
	2	0.5000000000	0.5461488004	0.5756651764	0.5866757371	0.5737189263	0.5250884537	0.4163583717
15°	1	0.4538518028	0.5000000000	0.5275483899	0.5342123264	0.5135418228	0.4517077471	0.00000000
	2	0.4538511996	0.5000000000	0.5275487711	0.5342130598	0.5135430815	0.4517095243	0.3194818701
30°	1	0.4243358359	0.4724516101	0.5000000000	0.5043041764	0.4775874769	0.4025526091	0.0000000000
	2	0.4243348236	0.4724512289	0.5000000000	0.5043044947	0.4775883208	0.4025539097	0.2403822939
45°	1	0.4133257076	0.4657876736	0.4956958236	0.5000000000	0.4690274903	0.3795101701	0.0000000000
	2	0.4133242629	0.4657869402	0.4956955053	0.5000000000	0.4690280103	0.3795110490	0.1724574256
60°	1	0.4262830838	0.4864581772	0.5224125231	0.5309725097	0.5000000000	0.3958943363	0.0000000000

	2	0.4262810737	0.4864569185	0.5224116792	0.5309719897	0.5000000000	0.3958947946	0.1115563906
75°	1	0.4749142177	0.5482922529	0.5974473909	0.6204898299	0.6041056637	0.5000000000	0.0000000000
	2	0.4749115463	0.5482904757	0.5974460903	0.6204889510	0.6041052054	0.5000000000	0.05480083896
90°	1	0.5836451098	0.6805204708	0.7596194386	0.8275435286	0.8884445423	0.9451996194	0.5000000000
	2	0.0000000000	0.1557738132	0.2585574188	0.3113468684	0.2991949705	0.1391368174	0.5000000000

Figure 3.10 shows the graph of discharge ratio, q_r against division angles, θ_2 when angles, θ_1 from 0^0 to 90^0 for V-shape in Case 1. When $\theta_1 = 0^0, 15^0, 30^0, 45^0.60^0, 75^0$, the discharge ratio is less than the critical ratio except $\theta_1 = 90^0$. It can be seen that when $\theta_1 = 90^0$, the discharge ratio exceeds the critical ratio and it obvious when $\theta_2 = 75^0$. Most of the division angles of θ_1 can be paired with $\theta_2 = 90^0$ since the discharge ratio is less than critical ratio except $\theta_1 = 90^0$.

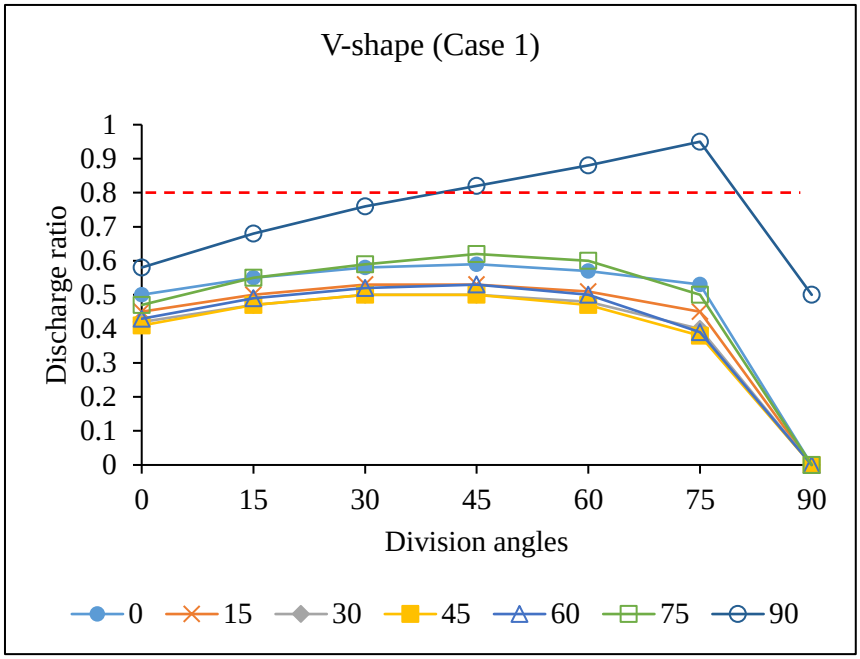


Figure 3.10 Graph of The Discharge Ratio Against Division Angles for The V-Shape Channel (Case 1)

Figure 3.11 shows the graph of discharge ratio, q_r against division angles, θ_2 when angles, θ_1 from 0^0 to 90^0 for V-shape in Case 2. The critical discharge ratio of the channel is 0.8. It can be seen that when $\theta_1 = 0^0, 15^0, 30^0, 45^0.60^0$, the discharge ratio approaches to the critical ratio, except when $\theta_1 = 75^0, 90^0$. From the graph, it is obvious that the discharge ratio for the V-shape channel is below the critical ratio when $\theta_1 = 90^0$ and with any division angles, except at $\theta_2 = 90^0$.

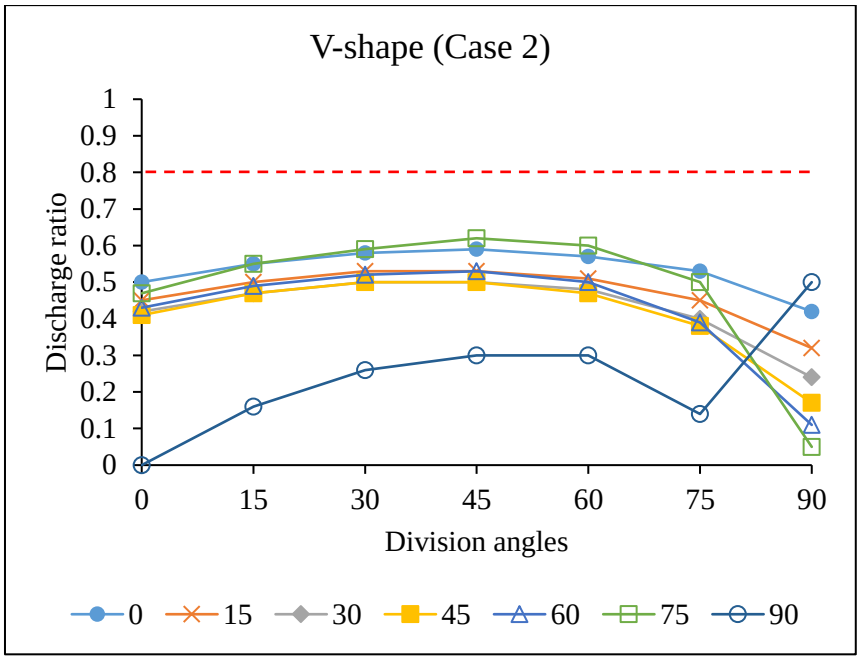


Figure 3.11 Graph of The Discharge Ratio Against Division Angles for The V-Shape Channel (Case 2)

3.6.4 Summary of Division Angles for Trapezoidal, Rectangular and V-Shapes Cross-Sectional Channels

Table 3.8 shows the summary of division angles for all types of cross-section channels when q_r is less than the critical discharge ratio

Table 3.8
The Division Angles when $q_r \leq 0.8$

θ_1	Trapezoidal		Rectangular		V-shape	
	θ_2 (Case 1)	θ_2 (Case 2)	θ_2 (Case 1)	θ_2 (Case 2)	θ_2 (Case 1)	θ_2 (Case 2)
0^0	0°,15°,30°, 45°,60°, 75°,90°	60°,75°, 90°	0°,15°,30°, 45°,60°, 75°,90°	75°,90°	0°,15°,30°, 45°,60°, 75°	0°,15°,30°, 45°,60°, 75°,90°
15^0	0°,15°,30°, 45°,60°, 75°,90°	0°,60°, 75°,90°	0°,15°,30°, 45°,60°, 75°,90°	60°,75°, 90°	0°,15°,30°, 45°,60°, 75°	0°,15°,30°, 45°,60°, 75°,90°
30^0	0°,15°,30°, 45°,60°, 75°,90°	0°,45°,60°, 75°,90°	0°,15°,30°, 45°,60°, 75°,90°	60°,75°, 90°	0°,15°,30°, 45°,60°, 75°,90°	0°,15°,30°, 45°,60°, 75°,90°

45^0	0°,15°,30°, 45°,60°, 75°,90°	0°,60°, 75°,90°	0°,15°,30°, 45°,60°, 75°,90°	75°,90°	0°,15°,30°, 45°,60°, 75°,90°	0°,15°,30°, 45°,60°, 75°,90°
60^0	0°,15°,30°, 45°,60°, 75°,90°	75°,90°	0°,15°,30°, 45°,60°, 75°,90°	75°,90°	0°,15°,30°, 45°,60°, 75°,90°	0°,15°,30°, 45°,60°, 75°,90°
75^0	0°,15°,30°, 45°,60°, 75°,90°	90°	0°,15°,30°, 45°,60°, 75°,90°	90°	0°,15°,30°, 45°,60°, 75°,90°	0°,15°,30°, 45°,60°, 75°,90°
90^0	0°,15°,30°, 45°,60°, 75°,90°	0°,15°,30°, 45°,60°, 75°	0°,15°,30°, 45°,60°, 75°,90°	0°,15°,30°, 45°,60°, 75°	0^0,15^0, 30^0,90^0	0°,15°,30°, 45°,60°, 75°,90°

Table 3.9
The Cross-Sectional Shape with Division Angles

θ_1	θ_2						
	0^0	15^0	30^0	45^0	60^0	75^0	90^0
0^0	T1 R1 V1 V2	T1 R1 V1 V2	T1 R1 V1 V2	T1 R1 V1 V2	T1 T2 R1 V1 V2	T1 T2 R1 R2 V1 V2	T1 T2 R1 R2 V2
15^0	T1 T2 R1 V1 V2	T1 R1 V1 V2	T1 R1 V1 V2	T1 R1 V1 V2	T1 T2 R1 R2 V1 V2	T1 T2 R1 R2 V1 V2	T1 T2 R1 R2 V2
30^0	T1 T2 R1 V1 V2	T1 R1 V1 V2	T1 R1 V1 V2	T1 T2 R1 V1 V2	T1 T2 R1 R2 V1 V2	T1 T2 R1 R2 V1 V2	T1 T2 R1 V1 V2
45^0	T1 T2 R1 V1 V2	T1 R1 V1 V2	T1 R1 V1 V2	T1 R1 V1 V2	T1 T2 R1 V1 V2	T1 T2 R1 R2 V1	T1 T2 R1 R2 V1

						V2	V2
60^0	T1 R1 V1 V2	T1 R1 V1 V2	T1 R1 V1 V2	T1 R1 V1 V2	T1 R1 V1 V2	T1 T2 R1 R2 V1 V2	T1 T2 R1 R2 V1 V2
75^0	T1 R1 V1 V2	T1 R1 V1 V2	T1 R1 V1 V2	T1 R1 V1 V2	T1 R1 V1 V2	T1 R1 V1 V2	T1 T2 R1 R2 V1 V2
90^0	T1 T2 R1 R2 V1 V2	T1 T2 R1 R2 V1 V2	T1 T2 R1 R2 V1 V2	T1 T2 R1 R2 V2	T1 T2 R1 R2 V2	T1 T2 R1 R2 V2	T1 R1 V1 V2

T1: Trapezoidal (case 1), T2: Trapezoidal (case 2), R1: Rectangular (case 1), R2: Rectangular (case 2), V1: V-shaped (case 1), V2: V-shaped (case 2)

From Table 3.8, in Case 1, the discharge ratio in the trapezoidal and rectangular channels is less than 0.8 for all division angles. However, it can be observed that the discharge ratio in V-shaped channel is below the critical discharge ratio when $\theta_1 = 90^0$ and $\theta_2 = 0^0, 15^0, 30^0, 90^0$. In Case 2, the discharge ratio in the trapezoidal and rectangular channels are below the critical discharge ratio when $\theta_1 = 90^0$ and $\theta_2 = 0°, 15°, 30°, 45°, 60°, 75°$. Angles at channel 1, $\theta_1 = 0^0, 15^0, 30^0, 45^0.60^0, 75^0$ can be paired with $\theta_2 = 90^0$ for all channels and cases. When the division angles $\theta_1 = 75^0$ and $\theta_2 = 90^0$, the discharge ratio is less than 0.8 for all channels and cases. Meanwhile, when $\theta_1 = 60^0$ and $\theta_2 = 75^0$ or $\theta_2 = 90^0$, the discharge ratio is below the critical discharge ratio for all cases. Nevertheless, for all channels, Case 1 is suitable for finding the discharge ratio below the critical discharge ratio to prevent the channel from overflowing. On the other hand, it is also observed that the discharge ratio for the

trapezoidal and rectangular in Case 1 and V-shaped in Case 2 is less than 0.8 for all division angles

3.7 Conclusion

The chapter mainly discusses the analysis of mathematical models of open channel dividing flow, specifically focusing on the effect of division angles on the discharge ratio. Based on different division angles, the discharge ratio in the trapezoidal, rectangular and V-shape cross-sectional channels are categorized based on Case 1 and Case 2, which represent the cases of different and constant bottom width of channels, respectively. For case 1, the discharge ratio for trapezoidal and rectangular cross-sectional channels is less than the critical discharge ratio for all division angles. For all angles at channel 2, θ_2, the V-shaped cross-sectional channel is less than the critical discharge ratio when $\theta_1 = 30°, 45°, 60°$ and $75°$. For case 2, the discharge ratio for V-shaped cross-sectional channel is less than critical discharge ratio for all division angles.

Meanwhile, trapezoidal and rectangular have optimal discharge ratio for all division angles in θ_2 when $\theta_1 = 90^0$ but not for $\theta_1 = \theta_2 = 90^0$. Therefore, case 1 shows that trapezoidal and rectangular tend not to overflow for any division angles, while for case 2, V-shaped has produced the discharge ratio below critical discharge. The discharge ratio must be less than the critical discharge to prevent the channel from overflow, and the discharge ratio is affected by the division angles. Hence, the first objective is achieved. As the division angle (ranging from 0° to 90°) increases**,** both real and imaginary parts of the complex roots increase, reflecting a growing nonlinear response in the system. At a certain division angle, the model yields very small real root (approaching zero) and a pair of complex conjugate roots.

The real solutions, although technically valid, remain extremely small across all cases and are unlikely to represent any physically meaningful discharge, indicating a near-zero or negligible flow condition. The complex roots, while mathematically significant, have no direct hydraulic interpretation in steady open channel flow and are typically discarded in practical analysis. Their presence suggests the underlying polynomial equations model a system that becomes increasingly non-linear or potentially unstable as the division angle increases. A comparison between the two cases shows consistent trends, with Case 2 generally yielding slightly smaller real and imaginary components than Case 1, possibly due to different assumptions or parameters

in the width of channels. Overall, the results imply that the model produces more pronounced complex behavior, and the solutions drift further from physical realism, showing a need for model refinement or the application of solution constraints to extract meaningful, real results.

CHAPTER 4
MODELLING OF OPEN-CHANNEL DIVIDING FLOW WITH REYNOLD'S NUMBER

4.1 Introduction

Despite numerous successful research on dividing flows, it is important to carry out the mathematical modelling with specific concern to Reynold's number to improve the accuracy of the solution. Interestingly, the mathematical model of dividing flow in open- channel related to Reynold's number has yet to be established in the literature. Therefore, this chapter aims to introduce a new mathematical model concerning the Reynold's number. The roughness coefficient is applied in the dividing flow equations, which are based on the principle of momentum conservation. The angles in the channel junction affect the discharge in the channel after a junction; thus, the relationships between the discharge ratio and division angles are investigated.

4.2 Modelling of Dividing Flow

A prismatic channel (trapezoidal, rectangular and V-shaped cross-sectional channel) is chosen to investigate the effect of angles upon discharge ratio and various angles below $90°$ are considered. A uniform flow is preferred in order to find the discharge ratio based on the bifurcation angles and maintain the stability of the dividing flow to evade any appalling consequences. The kinematic viscosity, dynamic viscosity and specific weight of water have a certain value at a certain temperature (Kestin et al., 1978; Korson et al., 1969). In this study, $20°$ Celsius is chosen to be temperature of water.

Reynold's numbers are utilized to classify the flow type in open channel flow. However, the Reynold's number takes into account the viscosity of water. The viscosity of any fluid type has a specific value at a particular temperature. In this study, the Reynolds number is considered as a parameter, while keeping the temperature constant at $20°$ Celsius in both the upstream and downstream sections of the channel. Reynolds number, $\mathrm{Re}_0 = \frac{VH_R}{\upsilon}$ (Uruba, 2019), where $\upsilon = 1.004,$ is a kinematic viscosity, $\upsilon = \frac{\mu}{\rho}$

. The density is $\rho = \frac{\gamma}{g}$ where $\gamma = 9.787114841$ is a specific weight of water and $\mu = 1.002$ is a dynamic viscosity (Kestin et al., 1978; Korson et al., 1969). However, the slope in the main channel is different for each type of cross-sectional channels.

4.2.1 Trapezoidal Cross-Sectional Channel with Reynold's Number

The similar procedure in Chapter 3 is employed to obtain the new model with Reynold's number. From (3.3), the hydrostatic force is integrated with respect to the area, yields

$$P = \gamma \int_0^y by + zy^2 dy = \gamma \left[\frac{by^2}{2} + \frac{zy^3}{3} \right]_0^y = \gamma \left(\frac{by^2}{2} + \frac{zy^3}{3} \right). \tag{4.1}$$

The steps are repeated from (3.7) to (3.13). Substitute (4.1) and $\Delta P = \gamma \left(\frac{b_0 y_2^2}{2} + \frac{a y_2^3}{3} \right) - P_2 \cos\theta_2$ to the left-hand side of (3.3), the equation will obtain

$$\gamma \left[\begin{array}{l} \left(\frac{b_0 y_0^2}{2} + \frac{a y_0^3}{3} \right) - \left(\frac{b_2 y_2^2}{2} + \frac{a y_2^3}{3} \right) \cos\theta_2 - \left(\frac{b_1 y_1^2}{2} + \frac{a y_1^3}{3} \right) \cos\theta_1 - \left(\frac{b_0 y_2^2}{2} + \frac{a y_2^3}{3} \right) \\ + \left(\frac{b_2 y_2^2}{2} + \frac{a y_2^3}{3} \right) \cos\theta_2 \end{array} \right]. \tag{4.2}$$

Expand, simplify and factorise (4.2), yields

$$\gamma \left[\frac{1}{2} \left(b_0 y_0^2 - b_0 y_2^2 - b_1 y_1^2 \cos\theta_1 \right) + \frac{a}{3} \left(y_0^3 - y_2^3 - y_1^3 \cos\theta_1 \right) \right] \tag{4.3}$$

From the right-hand side of (3.3) and modify (3.1) into $V = \frac{Q}{A}$, resulting in

$$\frac{\gamma}{g} \left(\frac{Q_2 Q_2}{A_2} \cos\theta_2 + \frac{Q_1 Q_1}{A_1} \cos\theta_1 - \frac{Q_0 Q_0}{A_0} + \frac{Q_2 Q_0}{A_0} C \sin\theta_2 + \frac{Q_1 Q_0}{A_0} C \sin\theta_1 \right) \tag{4.4}$$

Factorise (4.4) to produce

$$\frac{\gamma}{g} \frac{Q_0^2}{A_0} \left(\frac{Q_2^2 A_0}{A_2 Q_0^2} \cos\theta_2 + \frac{Q_1^2 A_0}{A_1 Q_0^2} \cos\theta_1 - 1 + \frac{Q_2}{Q_0} C \sin\theta_2 + \frac{Q_1}{Q_0} C \sin\theta_1 \right) \tag{4.5}$$

By manipulating (4.5) algebraically, the following expression is obtained:

$$\frac{\gamma}{g}\frac{Q_0^2}{A_0}\left[\frac{1}{Q_0^2}\frac{Q_2^2}{A_2/A_0}\cos\theta_2+\frac{1}{Q_0^2}\frac{Q_1^2}{A_1/A_0}\cos\theta_1-1+C\left(\frac{Q_2}{Q_0}\sin\theta_2+\frac{Q_1}{Q_0}\sin\theta_1\right)\right] \tag{4.6}$$

Let $q_r=\frac{Q_1}{Q_0}$, where $Q_1=Q_0q_r$. From (3.1),

$$Q_0=Q_0q_r+Q_2 \tag{4.7}$$

Then (4.7) turns into $\frac{Q_2}{Q_0}=1-q_r$. Thus, (4.6) becomes

$$\frac{\gamma}{g}\frac{Q_0^2}{A_0}\left(\frac{(1-q_r)^2}{A_2/A_0}\cos\theta_2+\frac{q_r^2}{A_1/A_0}\cos\theta_1-1+C\left((1-q_r)\sin\theta_2+q_r\sin\theta_1\right)\right) \tag{4.8}$$

The Reynold's number, $\mathrm{Re}_0=\frac{V_0R_{h_0}}{\upsilon}$ can be expanded as

$$\mathrm{Re}_0=\frac{\frac{Q_0}{A_0}\frac{A_0}{P_{w_0}}}{\frac{\mu}{\rho}}=\frac{Q_0\rho}{P_{w_0}\mu} \tag{4.9}$$

where $\rho=\frac{\gamma}{g}$. Rearrange (4.9),

$$P_{w_0}\mu\,\mathrm{Re}_0=Q_0\rho \tag{4.10}$$

by squaring both sides of (4.10),

$$\frac{{P_{w_0}}^2\mu^2\,{\mathrm{Re}_0}^2}{\rho}={Q_0}^2\rho \tag{4.11}$$

Multiply (4.11) both sides with $\frac{1}{A_0}$, yields

$$\frac{{P_{w_0}}^2\mu^2\,{\mathrm{Re}_0}^2}{\rho A_0}=\frac{{Q_0}^2\rho}{A_0} \tag{4.12}$$

Hence, replace $\frac{\gamma}{g}\frac{Q_0^2}{A_0}$ in (4.8) by (4.12) to produce

$$\frac{P_{w_0}{}^2 \mu^2 \operatorname{Re}_0{}^2}{\rho A_0}\left(\frac{(1-q_r)^2}{A_2/A_0}\cos\theta_2+\frac{q_r^2}{A_1/A_0}\cos\theta_1-1+C\left((1-q_r)\sin\theta_2+q_r\sin\theta_1\right)\right) \quad (4.13)$$

From (4.13), the coefficient C is derived by incorporating the Reynold's number into the formulation in (2.5), yielding

$$C=\frac{5}{6}-\frac{\left(\frac{\operatorname{Re}_1 \mu}{\rho R_h}\right)^2}{40g\left(\frac{A_1}{T}\right)}-\frac{ay_1}{12b_1q_r}\left(\frac{b_1+2ay_1}{b_1+2ay_1+\frac{a^2y_1{}^2}{b_1}}\right), \quad (4.14)$$

Simplify (4.14) and replace $R_h=\frac{A_1}{P_w}$ and $\rho=\frac{\gamma}{g}$ in (4.15), will become

$$C=\frac{5}{6}-\frac{\operatorname{Re}_1{}^2 \mu^2 T}{40gA_1\left(\frac{A_1}{P_w}\right)^2\left(\frac{\gamma}{g}\right)^2}-\frac{ay_1}{12b_1q_r}\left(\frac{b_1+2ay_1}{b_1+2ay_1+\frac{a^2y_1{}^2}{b_1}}\right). \quad (4.15)$$

Upon simplifying (4.15) and (4.3) with (4.13), the final model is a new model of open-channel dividing flow with Reynold's number in trapezoidal channel (OCDFR-T):

$$\begin{aligned}&\frac{\gamma^2 A_0}{g}\left[\frac{1}{2}\left(b_0y_0^2-b_0y_2^2-b_1y_1^2\cos\theta_1\right)+\frac{a}{3}\left(y_0^3-y_2^3-y_1^3\cos\theta_1\right)\right]=\\&P_{w_0}{}^2\mu^2\operatorname{Re}_0{}^2\left(A_0\left(\frac{(1-q_r)^2}{A_2}\cos\theta_2+\frac{q_r^2}{A_1}\cos\theta_1\right)-1+C\left((1-q_r)\sin\theta_2+q_r\sin\theta_1\right)\right)\end{aligned} \quad (4.16)$$

where $C=\frac{5}{6}-\frac{T_1gP_{w_1}{}^2\mu^2\operatorname{Re}_1{}^2}{40A_1{}^3\gamma}-\frac{y_1a}{12b_1q_r}\left(\frac{b_1+2y_1a}{b_1+2y_1a+\frac{y_1{}^2a^2}{b_1}}\right)$.

The open-channel dividing flow for trapezoidal with Reynold's number are solved by using the Maple software by findings the geometric hydraulic properties. Then, the velocity from the Manning's equation needs the value of the main channel slope in order to calculate the Reynold's number. Assume that the slope for main channel is $S_0=0.0001814260235$. Thus, Reynold's number in the main channel is

$\mathrm{Re}_0 = 2.837766734$. The Reynold's number represent the types of flow in the main channel, which are subcritical and laminar flow.

4.2.2 Rectangular Cross-Sectional Channel with Reynold's Number

The same steps from trapezoidal cross-sectional channel are taken by this channel to derive the rectangular cross-sectional channel equation with Reynold's number. The hydrostatic force is integrated as same as before but only the area is different,

$$P = \gamma \int_0^y by dy = \gamma \left[\frac{by^2}{2} \right]_0^y = \gamma \left(\frac{by^2}{2} \right) \tag{4.17}$$

Substitute (4.17) and $\Delta P = \gamma \left(\frac{b_0 y_2^2}{2} \right) - P_2 \cos\theta_2$ to the left-hand side of (3.3), the equation will obtain

$$\gamma \left[\left(\frac{b_0 y_0^2}{2} \right) - \left(\frac{b_2 y_2^2}{2} \right) \cos\theta_2 - \left(\frac{b_1 y_1^2}{2} \right) \cos\theta_1 - \left(\frac{b_0 y_2^2}{2} \right) + \left(\frac{b_2 y_2^2}{2} \right) \cos\theta_2 \right]. \tag{4.18}$$

Expand, simplify and factorise (4.18), yields

$$\gamma \left[\frac{1}{2} \left(b_0 y_0^2 - b_0 y_2^2 - b_1 y_1^2 \cos\theta_1 \right) \right] \tag{4.19}$$

Next, steps (4.4) to (4.13) are repeat for the right-hand side in (3.3).

$$\frac{P_{w_0}{}^2 \mu^2 \mathrm{Re}_0{}^2}{\rho A_0} \left(\frac{(1-q_r)^2}{A_2 / A_0} \cos\theta_2 + \frac{q_r^2}{A_1 / A_0} \cos\theta_1 - 1 + C\left((1-q_r) \sin\theta_2 + q_r \sin\theta_1 \right) \right) \tag{4.20}$$

From (4.20), the coefficient C is derived by incorporating the Reynold's number into the formulation in (2.5) where $k_0 = 0$ for rectangular channel, yielding

$$C = \frac{5}{6} - \frac{\left(\frac{\mathrm{Re}_1 \mu}{\rho R_h}\right)^2}{40g\left(\frac{A_1}{T}\right)}, \tag{4.21}$$

Simplify (4.21) and replace $R_h = \frac{A_1}{P_w}$ and $\rho = \frac{\gamma}{g}$ in (4.22), will become

$$C = \frac{5}{6} - \frac{\mathrm{Re}_1{}^2 \mu^2 T}{40gA_1\left(\frac{A_1}{P_w}\right)^2\left(\frac{\gamma}{g}\right)^2}. \tag{4.22}$$

Upon simplifying (4.22) and (4.19) with (4.20), the final model is a new model of open-channel dividing flow with Reynold's number in rectangular channel (OCDFR-R):

$$\begin{aligned} &\frac{\gamma^2 A_0}{g}\left[\frac{1}{2}\left(b_0 y_0^2 - b_0 y_2^2 - b_1 y_1^2 \cos\theta_1\right)\right] = \\ &P_{w_0}{}^2 \mu^2 \,\mathrm{Re}_0{}^2\left(A_0\left(\frac{(1-q_r)^2}{A_2}\cos\theta_2 + \frac{q_r^2}{A_1}\cos\theta_1\right) - 1 + C\left((1-q_r)\sin\theta_2 + q_r \sin\theta_1\right)\right) \end{aligned} \tag{4.23}$$

where $C = \frac{5}{6} - \frac{T_0 g P_{w_0}{}^2 \mu^2 \,\mathrm{Re}_0{}^2}{40A_0{}^3\gamma}$. The slope of the main channel is $S_0 = 0.00017491795$. Thus, Reynold's number in the main channel is $\mathrm{Re}_0 = 2.916591321$, which are subcritical and laminar flow.

4.2.3 V-Shaped Cross-Sectional Channel with Reynold's Number

The same steps from previous section are repeat to become a new model of open-channel dividing flow with Reynold's number in V-shape channel (OCDFR-V). The hydrostatic force is integrated as same as before but only the area is different,

$$P = \gamma\int_0^y ay^2 dy = \gamma\left[\frac{ay^3}{3}\right]_0^y = \gamma\left(\frac{ay^3}{3}\right) \tag{4.24}$$

Substitute (4.24) and $\Delta P = \gamma\left(\frac{ay_2^3}{2}\right) - P_2\cos\theta_2$ to the left-hand side of (3.3), the equation will obtain;

$$\gamma\left[\left(\frac{ay_0^3}{3}\right) - \left(\frac{ay_2^3}{3}\right)\cos\theta_2 - \left(\frac{ay_1^3}{3}\right)\cos\theta_1 - \left(\frac{ay_2^3}{3}\right) + \left(\frac{ay_2^3}{3}\right)\cos\theta_2\right]. \tag{4.25}$$

Expand, simplify and factorise (4.25), yields

$$\gamma\frac{a}{3}\left[y_0^3 - y_2^3 - y_1^3\cos\theta_1\right] \tag{4.26}$$

Next, steps (4.4) to (4.13) are repeat for the right-hand side in (3.3).

$$\frac{P_{w_0}{}^2\mu^2\,\mathrm{Re}_0{}^2}{\rho A_0}\left(\frac{(1-q_r)^2}{A_2/A_0}\cos\theta_2 + \frac{q_r^2}{A_1/A_0}\cos\theta_1 - 1 + C\left((1-q_r)\sin\theta_2 + q_r\sin\theta_1\right)\right) \tag{4.27}$$

Then, (4.26) is equal to (4.27) to become a new model of open-channel dividing flow with Reynold's number in V-shape channel (OCDFR-V):

$$\frac{\gamma^2 A_0}{g}\frac{a}{3}\left[\left(y_0^3 - y_2^3 - y_1^3\cos\theta_1\right)\right] =$$
$$P_{w_0}{}^2\mu^2\,\mathrm{Re}_0{}^2\left(A_0\left(\frac{(1-q_r)^2}{A_2}\cos\theta_2 + \frac{q_r^2}{A_1}\cos\theta_1\right) - 1 + C\left((1-q_r)\sin\theta_2 + q_r\sin\theta_1\right)\right) \tag{4.28}$$

where $C = \frac{5}{6} - \frac{T_0 g P_{w_0}{}^2\mu^2\,\mathrm{Re}_0{}^2}{40A_0{}^3\gamma}$. The slope of the main channel is $S_0 = 0.00042681062$ and Reynold's number in the main channel is $\mathrm{Re}_0 = 1.49391182$. The Maple software is used to evaluate the discharge ratio, q_r for different cross-sectional channel based on its GHP.

4.3 FLOW-3D Simulation

The physical experiment in a hydraulic laboratory or computer simulation for results validation may not be accessible due to high cost and time-consuming. However, the validity of the proposed model in computing the discharge ratio at various bifurcation angles can be validated using a computational fluid dynamics (CFD) simulation software, that uses the Navier–Stokes equations and the volume of fluid

(VOF) method to simulate and analyse complex fluid-based problem and interactions (Ghamam et al., 2023). FLOW-3D is widely used to validate the experimental results since it is known for its robustness and tendency to numerically reproduce flow with a clear visualization power accurately (Abdurrasheed et al., 2019). This software has advanced capabilities in modeling free-surface flows, such as in hydraulic engineering. FLOW-3D gained accuracy with percentage errors of less than 5% when compared with the experimental values. Therefore, the FLOW-3D simulation was conducted to validate the performance of the proposed mathematical model.

4.4 Setting Up Physics and Fluid Properties of FLOW-3D

There are many physics options available in FLOW-3D, but only two selections are required. First is the gravity option with gravitational acceleration in the vertical (z) direction set to -9.81 m/s^2. Second is the viscosity and turbulence model, where for this study, the Renormalized Group model was used, and the wall shear boundary condition is automatically set to a no-slip condition when the viscous flow is selected. In this setup, the fluid properties were based on the selected fluid. In this research, the temperature of water at $20°$ Celsius was used. The density and viscosity of water are 1000 kg/m^3 and 0.001 kg/m/s, respectively. Other parameters remained constant as default.

4.5 Meshing and Geometry

The preparation of model geometry is different for each simulation. For a bifurcated channel, the geometry was drawn in AutoCAD and exported in stereolithographic (stl) format. The most crucial part in CFD simulation is to determine an appropriate meshing size. The mesh and cell size can affect the accuracy and simulation time. In this study, the relative proportions of the computational domain dimensions are determined by the size ratio is (2: 2: 1) for each (x (length): y (width): z (height)), which does not exceed maximum size ratio 3:1 between two directions. After a suitable mesh is selected, the FAVORized tool is used to visualize the geometry so that it is sufficiently realistic with enough resolution to capture important features of the flow. Figures 4.1 and 4.2 show the actual and FAVORized geometry of the channel, respectively. The roughness property of the geometry is set to 0.242, equivalent to 0.03

manning's coefficient, n. The purpose of flux surface, which is located in each channel is to measure discharge and velocity in main and branch channels.

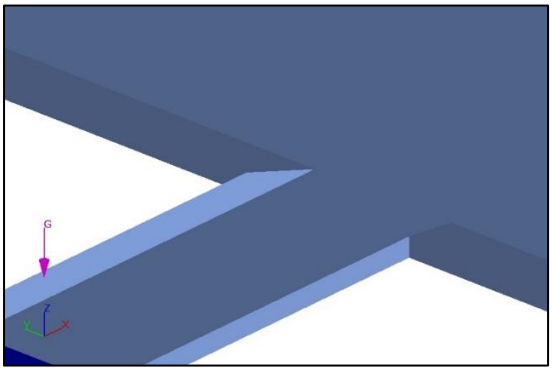


Figure 4.1 Actual geometry of the channel

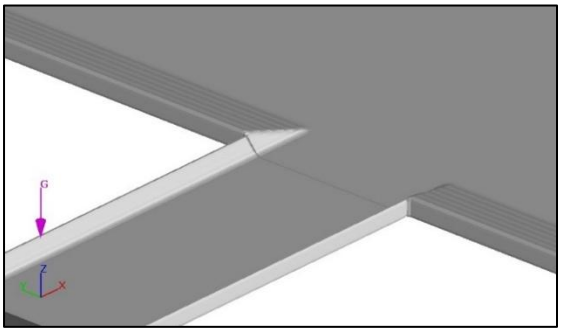


Figure 4.2 FAVORized geometry of the channel

4.6 Boundary and Initial Conditions

Boundary conditions define how fluid interacts with the edges of the computational domain. This condition is originally set to symmetry (S), which means no flow or heat transfer across this boundary. To study the discharge in the main and branch channels, the boundary condition at the main channel upstream is set to volumetric discharge (Q) and outflow (O) boundary conditions for both branch channels. The boundary at the top of the channel is set to a pressure (P) boundary condition, while the boundary at the bottom channel remains as default.

Initial conditions define the starting state of the fluid in the domain before the simulation begins. It follows the actual flow data of the water elevation and hydrostatic pressure. The discharge at the upstream is gradually increased from zero to the required discharge to reduce water splashing and immediate change of velocity, hence increasing the stability of the simulation and shortening the time to reach its steady state. The

setting of boundary and initial conditions will affect the simulation results as shown in Figures 4.3-4.8.

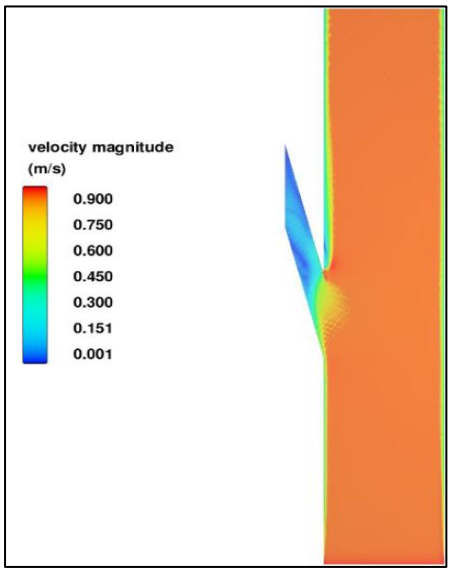


Figure 4.3 Velocity magnitude (m/s) when $\theta_1 = 0°$ and $\theta_2 = 15°$

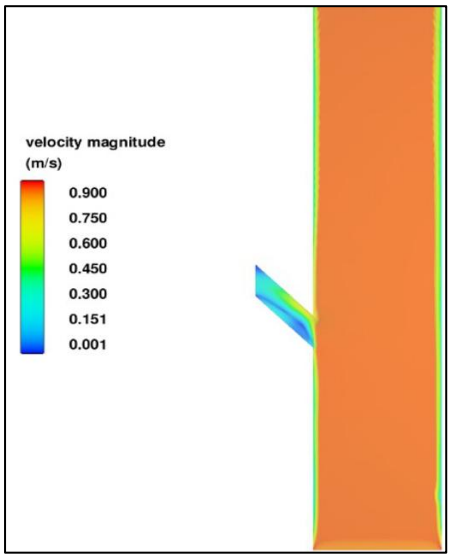


Figure 4.4 Velocity magnitude (m/s) when $\theta_1 = 0°$ and $\theta_2 = 45°$

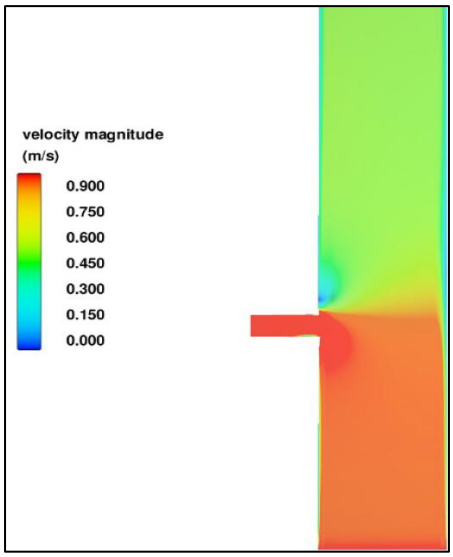


Figure 4.5 Velocity magnitude (m/s) when $\theta_1 = 0°$ and $\theta_2 = 90°$

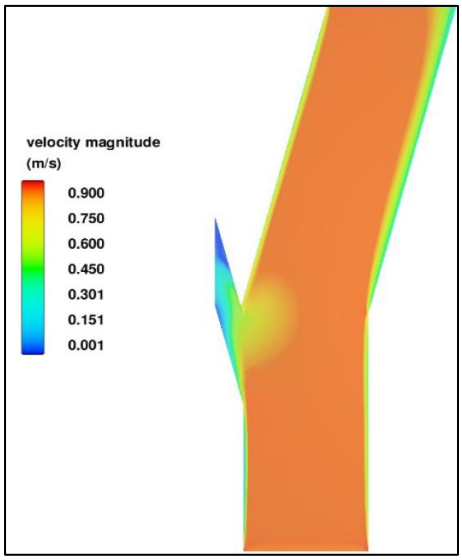


Figure 4.6 Velocity magnitude (m/s) when $\theta_1 = 15°$ and $\theta_2 = 15°$

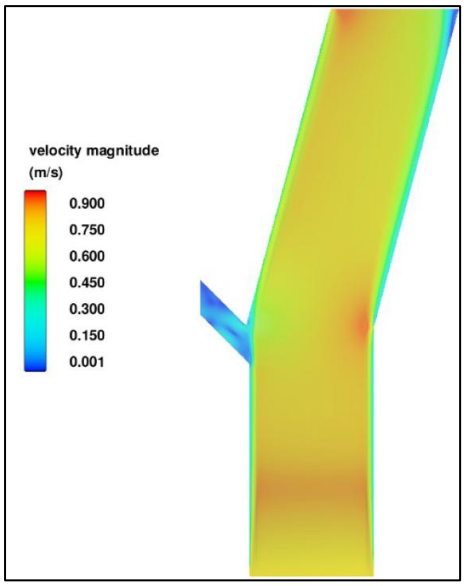


Figure 4.7 Velocity magnitude (m/s) when $\theta_1 = 15°$ and $\theta_2 = 45°$

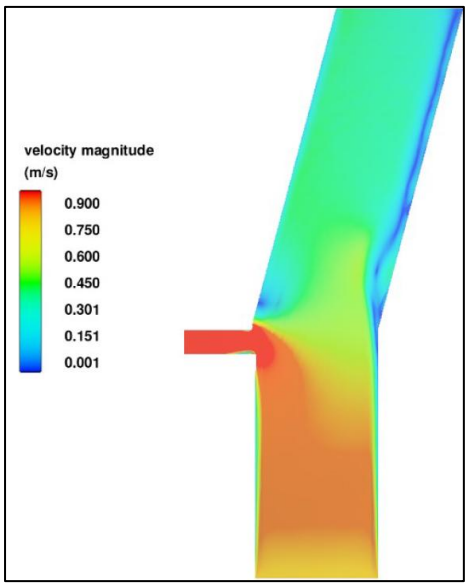


Figure 4.8 Velocity magnitude (m/s) when $\theta_1 = 15°$ and $\theta_2 = 90°$

4.7 Results Analysis

This section discusses the results of the proposed mathematical model of open channel dividing flow with Reynold's number for trapezoidal, rectangular and V-shape cross-sectional channel. As mention earlier, the FLOW-3D simulation results are available only for trapezoidal cross-sectional channel with $\theta_1 = 0°$ and $\theta_1 = 15°$, which is treated as benchmarking data for validating the proposed models. The critical discharge ratio, which represents theoretical threshold or limiting value is assumed to

be 0.8 for all cross-sectional channels. This value distinguishes between different flow regimes or behaviors. If the discharge ratio exceeds this value, it may lead to instability or overflow in branch channel 2.

4.7.1 Discharge Ratio in Trapezoidal Cross-Sectional Channel with Reynold's Number

Tables 4.1 and 4.2 exhibit the discharge ratio and its deviation percentage for the open channel dividing flow with Reynold's in trapezoidal channel (OCDFR-T), previous model of open-channel dividing flow in trapezoidal channel (OCDF-T) provided by Zawawi et al. (2019) and FLOW-3D simulation. The deviation percentage of OCDFR-T and OCDF-T is determined as follows:

$$\text{Deviation percentage (\%)} = \left| \frac{q_r^{\,Model} - q_r^{\,FLOW3D}}{q_r^{\,FLOW3D}} \right| \times 100,$$

where $q_r^{\,Model}$ is the discharge ratio of the OCDFR-T and OCDF-T, while $q_r^{\,FLOW3D}$ is the discharge ratio of the FLOW-3D simulation.

Table 4.1
The Discharge Ratio When $\theta_1 = 0°$

θ_2	OCDFR-T	OCDF-T	FLOW-3D	Deviation Percentage (%)	
				OCDFR-T	OCDF-T
15°	0.8468182695	0.8226499373	0.9815875219	13.73	16.19
30°	0.8511742960	0.8283690369	0.9785935509	13.02	15.35
45°	0.8439906764	0.8213714460	0.9766275734	13.58	15.90
60°	0.8166283420	0.7927880538	0.9502719692	14.06	16.57
75°	0.7382896595	0.7125397288	0.8518835633	13.33	16.36
90°	0.4138210173	0.4162893823	0.5132984892	19.38	18.90

From Table 4.1, the results show that the OCDFR-T model consistently exhibits lower deviation values compared to the OCDF-T model for all division angles except for $\theta_2 = 90°$. This consistency underscores the improved predictive alignment of OCDFR-T with the FLOW-3D simulation. Hence, the smallest deviation for the proposed model occurs at $\theta_2 = 30°$ (13.02%), whereas the largest is observed at

$\theta_2 = 90°$ (19.38%). The deviations in the OCDF-T remain uniformly higher when ranging from 15.35% to 18.90%.

Table 4.2
The Discharge Ratio When $\theta_1 = 15°$

θ_2	OCDFR-T	OCDF-T	FLOW-3D	Deviation Percentage (%)	
				OCDFR-T	OCDF-T
15°	0.8333117284	0.8066937934	0.9300000000	10.40	13.26
30°	0.8364214752	0.8110025330	0.9600000000	12.87	15.52
45°	0.8265790842	0.8010032400	0.9800000000	15.66	18.26
60°	0.7937457131	0.7663336286	0.9400000000	15.56	18.48
75°	0.7020171223	0.6717354488	0.7600000000	7.63	11.61
90°	0.3175102713	0.3194043084	0.4300000000	26.16	26.72

Table 4.2 shows that the OCDFR-T consistently have a lower deviation value for all division angles, except $\theta_2 = 90°$. The smallest deviation for the OCDFR-T is observed at $\theta_2 = 75°$ (7.63%), while the highest deviation is at $\theta_2 = 90°$ (26.16%). In comparison, OCDF-T exhibits larger deviations at all division angle. Although both mathematical models exhibit a higher deviation when $\theta_2 = 90°$, OCDFR-T remains comparably better even in this division angle. All the discharge ratios are less than the critical flow, while the angle at channel 2, $\theta_2 = 90°$ can be paired with any angles in channel 1, which are $\theta_1 = 0°$ and $15°$ to prevent the overflow in channel 2 (discharge ratio is less than 0.8). Both Figures 4.9 and 4.10 show a similar trend of discharge ratio, where an increase in the division angle in channel 2 results in a slight increase in the discharge ratio, followed by a sudden decrease for angles greater than 45°. It can be said that the results of the OCDFR-T model are closer to the FLOW-3D simulation than the OCDF-T model.

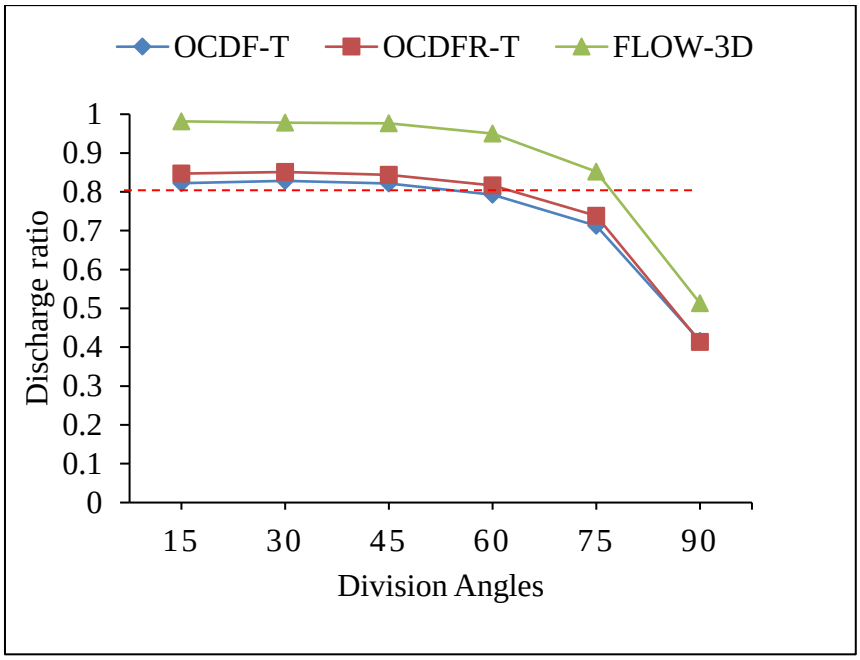


Figure 4.9 Graph Of The Discharge Ratio, q_r Against Division Angles, θ_2 When $\theta_1 = 0°$ for OCDF-T, OCDFR-T and FLOW-3D

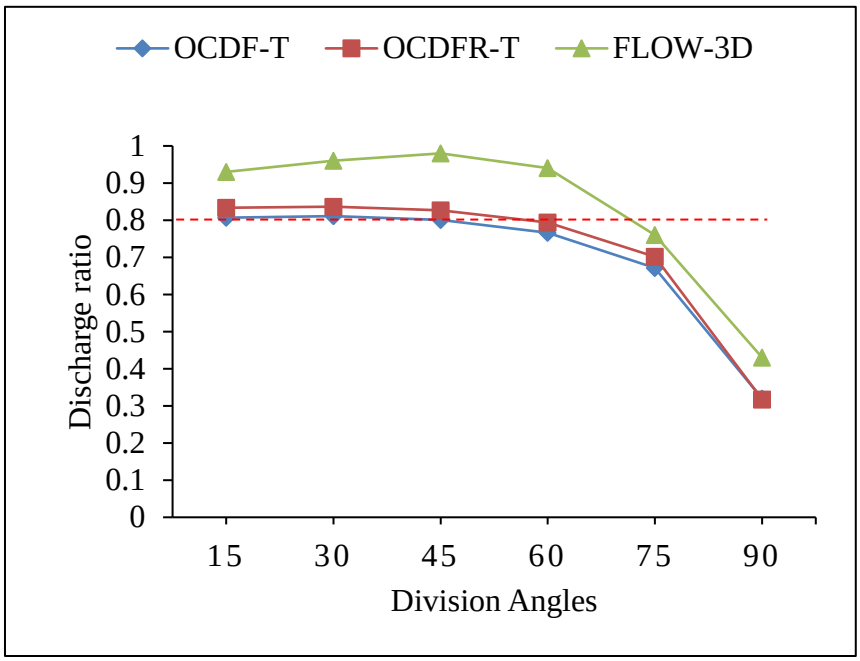


Figure 4.10 Graph Of The Discharge Ratio, q_r Against Division Angles, θ_2 When $\theta_1 = 15°$ for OCDF-T, OCDFR-T and FLOW-3D

The difference of results between the mathematical models and FLOW-3D simulation is most probably due to inaccurate boundary conditions used in the simulation or assumptions made in both techniques. For example, a mathematical model

may assume that the flow is steady-state, whereas in reality, the flow may be unsteady. Meanwhile, the viscosity of the fluid may vary with temperature, which the mathematical model may not account for. In contrast, FLOW-3D simulation solves the full Navier-Stokes equations in three-dimension, allowing for the detailed modelling of free-surface flow, turbulence and realistic channel geometries

4.7.2 Discharge Ratio in Rectangular Cross-Sectional Channel with Reynold's Number

The discharge ratio for the open channel dividing flow with Reynold's number in rectangular channel (OCDFR-R) is presented in Table 4.3 with $\theta_1 = 0°$ and $\theta_1 = 15°$. The discharge ratio for rectangular channel must be less than the critical discharge to prevent the overflow in channel 2.

Table 4.3
The Discharge Ratio For OCDFR-R When $\theta_1 = 0°$ and $\theta_1 = 15°$

θ_2	q_r	
	$\theta_1 = 0°$	$\theta_1 = 15°$
15°	0.846845279	0.8333333333
30°	0.8512280489	0.8364696572
45°	0.8440712522	0.8266532996
60°	0.816736904	0.7938463511
75°	0.7384333311	0.7021489307
90°	0.4140424520	0.3177013598

Table 4.3 presents the discharge ratio obtained by the OCDFR-R at various angles in branch channel ranging from $15°$ to $90°$. The discharge ratio is less than 0.8 when $\theta_1 = 0°$, $\theta_2 = 75°$ and $90°$. For $\theta_1 = 15°$, the discharge ratio for OCDFR-R is less than the critical discharge ratio when $\theta_2 = 60°, 75°$ and $90°$.

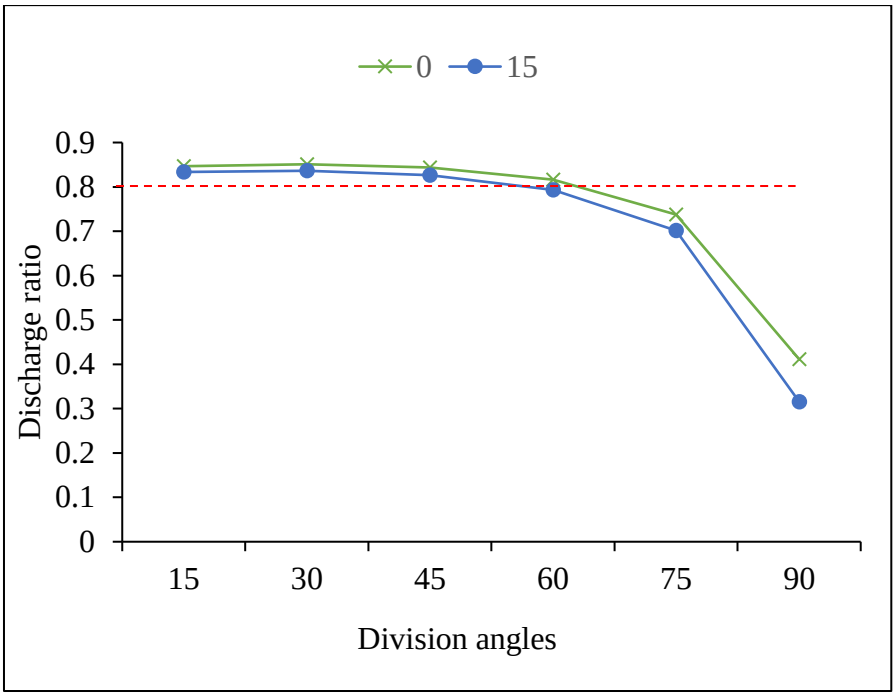


Figure 4.11 Graph Of The Discharge Ratio, q_r Against Division Angles, θ_2 When $\theta_1 = 0°$ and $15°$ for OCDFR-R

Figure 4.11 shows the graph of discharge ratio against division angles when $\theta_1 = 15°$ and $0°$. The horizontal dashed line in the graph represents the critical discharge ratio. It can be seen that the discharge ratio approaches the critical line when $\theta_2 = 15°, 30°, 45°$. For a single pair of angles, $\theta_1 = 15°$ and $\theta_2 = 60°$, the discharge ratio approaches the critical line. It can be observed that the division angles when $\theta_2 = 75°$ and $90°$ can be paired with any angles in θ_1. It can be observed that when the division angles is increased, the discharge ratio decreases. To validate the accuracy of the OCDFR-R, the results should be compared with the CFD simulation results from the theoretical three-dimensional (3D) ANSYS-16 software and experimental work provided by Sayed Abu-Zaid (2023). The computation of the proposed model follows the similar channel properties used in the experimental work, except several assumptions have to be made in order to produce the most optimal results. All the experiments were conducted in steady-flow conditions. The initial water depth was assumed to be about 0.16m in a 0.3m high duct at the inlet, which achieved an initial inlet mean velocity of about 0.3667 m/s. The main and branch channels have a width and depth of 0.3m. Due to the turbulence of the water surface and the occurrence of a separation zone, measuring water depths was challenging, especially at the beginning

of the branch channel and downstream of the junction region. The variance in water depths across the whole width of the channel makes it difficult to measure the dimensions of the separation zone empirically. Hence, it was necessary to compute the discharge in the main and branch channels for the different bifurcation angles. The discharge in the main channel was consistently 16.4 m/s in all division angles. Therefore, in this study, it was assumed that the flow depth in each downstream channel might decrease relative to the original 0.16m due to energy loss in the junction or difference slope.

Table 4.4 shows the discharge ratio of ANYSYS-16 simulation and experimental work in the diversion flume for different diversion angles, which were used in this study to validate the results produced by the OCDFR-R. The flow diverted into the dividing channel increases as the bifurcation angle decreases. This behavior may be influenced by the configuration of the junction between the main and branch channels, the extent of flow disturbance, and the energy losses occurring in the division region. The results of proposed model OCDFR-R show the best match with experimental data in discharge ratio across all angles, indicating good predictive accuracy.

Table 4.4
The Discharge Ratio And Estimated Flow Depth For OCDFR-R, ANSYS-16 Simulation, And Laboratory Experiment

θ_2	Discharge ratio, q_r			Estimated flow depth in channel 1, y_1	Estimated flow depth in channel 2, y_2
	ANSYS-16 simulation	Laboratory experiment	OCDFR-R	OCDFR-R	OCDFR-R
15°	0.506097561	0.554878049	0.5549451568	0.14	0.13
30°	0.793292683	0.8364696572	0.8326574754	0.14	0.08
45°	0.936585366	0.884756098	0.9463838398	0.13	0.09
60°	0.962195122	0.915853659	0.9684297788	0.12	0.1
75°	0.972560976	0.95304878	0.9671992092	0.12	0.1
90°	0.980487805	0.973170732	0.9669374413	0.12	0.1

Table 4.5 presents the deviation percentage that measures the difference between an observed discharge ratio value (ANSYS-16 simulation or OCDFR-R) and a reference value (experimental results), expressed as a percentage of the reference value.

Table 4.5
The Deviation Percentage Of ANSYS-16 Simulation and OCDFR-R

θ_2	Deviation Percentage (%)	
	ANSYS-16 simulation	OCDFR-R
15°	8.79	0.01
30°	5.16	0.46
45°	5.86	6.97
60°	5.06	5.74
75°	2.05	1.48
90°	0.75	0.64

It can be observed that the proposed model OCDFR-R have a great agreement between experimental results compared to the ANSYS-16 simulation results. At lower angles, particularly when $\theta_2 = 15°$ the OCDFR-R model demonstrates exceptional accuracy, with a deviation of only 0.01%, in stark contrast to the 8.79% deviation observed in the ANSYS-16 simulation. This indicates that OCDFR-R significantly outperforms ANSYS-16 at low diversion angles. As the angle increases to $\theta_2 = 30°$, OCDFR-R continues to show relatively low deviations of 0.46% and ANSYS-16 simulation have decrease deviation percentage which is 5.16%. However, at $\theta_2 = 45°$, OCDFR-R regains higher deviation percentage which is 6.97% slightly exceeding the deviations of ANSYS-16 (5.86%).

Despite this, OCDFR-R regains higher accuracy at larger angles $\theta_2 = 75°$ which is deviation of 1.48% compared to 2.05% for ANSYS-16. At $\theta_2 = 90°$, both methods produce very close results, with OCDFR-R at 0.64% and ANSYS-16 simulation at 0.75%. Overall, OCDFR-R demonstrates comparable accuracy across most division angles, especially at the critical low-angle condition, where accurate prediction is most challenging. These findings suggest that OCDFR-R is a robust and reliable tool for estimating discharge ratios in open-channel bifurcation flow, making it a valuable alternative to conventional numerical simulations.

4.7.3 Discharge Ratio in V-Shape Cross-Sectional Channel with Reynold's Number

The discharge ratio for the open channel dividing flow with Reynold's in V-shaped channel (OCDFR-V) is presented in Table 4.6. The results obtained by the OCDFR-V could not be validated due to the unavailability of relevant reference data.

Table 4.6
The Discharge Ratio For OCDFR-V When $\theta_1 = 0°$ and $\theta_1 = 15°$

θ_2	q_r	
	$\theta_1 = 0°$	$\theta_1 = 15°$
15°	0.8467287988	0.8333333334
30°	0.8509819103	0.8363504032
45°	0.8436621660	0.8263925126
60°	0.8160880662	0.7933875764
75°	0.7373300812	0.7013296081
90°	0.4114293070	0.3157008109

In Table 4.6, the discharge ratio for V-shaped cross-sectional channel is less than 0.8 when $\theta_1 = 0°$ and $\theta_2 = 75°, 90°$. The discharge ratio is less than the critical discharge ratio when $\theta_1 = 15°$ and $\theta_2 = 60°, 75°, 90°$.

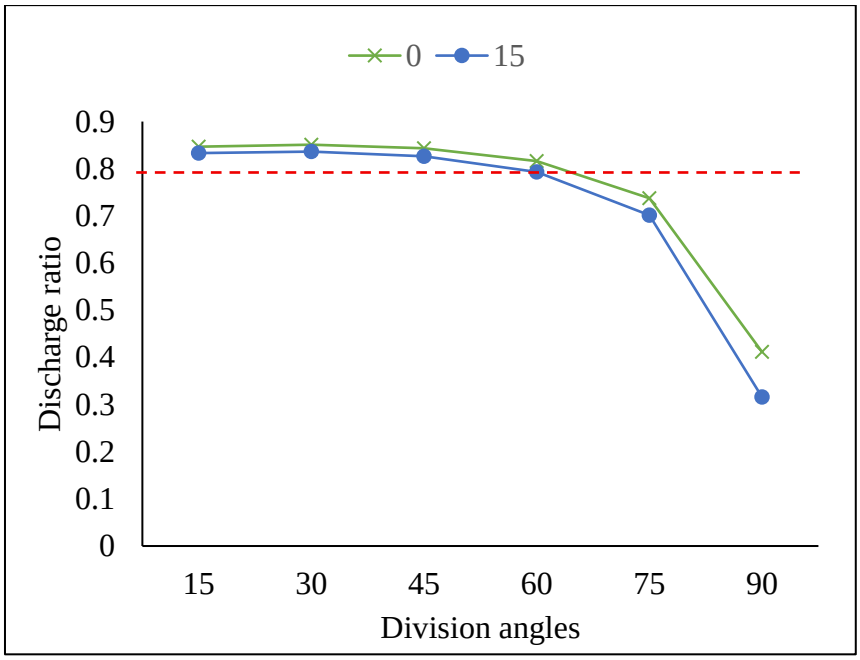


Figure 4.12 Graph Of The Discharge Ratio, q_r Against Bifurcation Angles, θ_2 When $\theta_1 = 0°$ and $15°$ for OCDFR-V

Figure 4.12 shows the graph of discharge ratio against bifurcation angles when $\theta_1 = 15°$ and $0°$ for V-shaped cross-sectional channel. The critical discharge ratio or critical line in this graph is 0.8. It is observed that when $\theta_2 = 75°$ and $90°$ for both bifurcation in branch channel 1, the discharge ratio is less than critical value and when $\theta_1 = 15°$ and $\theta_2 = 60°$ the discharge ratio approaches towards the critical line.

4.8 Conclusion

In this study, a new mathematical model of dividing open-channel flow with trapezoidal, rectangular and V-shaped cross-sectional channel has been derived based on the Reynold's number in the main channel to investigate the relationship between discharge ratio and division angles. In the context of an open channel flow, Reynold's number is important parameter because it determines whether the flow is laminar or turbulent, which affects the shear stresses and frictional losses in the channels. The discharge in an open channel dividing flow that is influenced by the Reynolds number affects the mixing and momentum transfer between the channels. However, the exact relationship between these parameters and the discharge depends on the GHP, Manning's roughness, as well as the properties of the fluid itself. By incorporating the Reynold's number in a mathematical model, the behavior of the discharge can be

estimated, particularly at locations where flow separation or other complex flow phenomena occur. This can result in more accurate predictions and better decision-making. These parameters may improve the efficiency of the modelling process, as they allow for the simplification of the model, while maintaining accuracy. This can save time and resources and make the modelling process more accessible to researchers and engineers.

Both simulation software and mathematical models can be useful tools for estimating discharge ratios in open channel flow systems. FLOW-3D offers more sophisticated and accurate representation of the flow behaviour, including complex phenomena, although it may require more computational resources and expertise for optimal utilisation. Conversely, mathematical models can provide more straightforward and faster solutions. However, they might not capture all the complexity of the flow behaviour. The decision to employ both methods for estimating discharge ratios is dependent upon the specific requirements of the research and the available resources. In certain cases, a combination of both methods may be employed, wherein simulation software provides more detailed information about the flow behaviour in specific regions, and mathematical models provide simpler and computationally efficient solutions for the entire system

CHAPTER 5
NUMERICAL ANALYSIS ON THE FLOW DEPTH BEHAVIOR IN OPEN-CHANNEL DIVIDING FLOW

5.1 Introduction

Flow depth can be defined as the vertical distance from the channel bed to the free surface of the water in an open-channel. In hydraulic engineering and open-channel flow analysis, flow depth is a key parameter used to determine hydraulic radius, cross-sectional area, and discharge. In this chapter, the OCDF-T, OCDF-R and OCDF-V models presented in Chapter 3 will be modified in the form of nonlinear polynomial equations. Subsequently, the resulting equations will be solved using the Newton-Raphson method to determine the upstream flow depth. Based on the GHP (case 2) presented in Chapter 3, the flow depth of dividing flow in trapezoidal, rectangular and V-shaped cross-sectional channels will be analysed with varying division angles and compared with experimental data for validation purposes. However, the experiment results provided in the literature are available only for the trapezoidal and rectangular cross-sectional channels due to time constraints. Lastly, comparative prediction of flow depth in trapezoidal, rectangular and V-shaped cross-sectional channels will be studied with similar flow conditions. The parametric investigation is based on two parameters, which are the Froude number and discharge ratio.

5.2 The Polynomial Equation of Open-Channel Dividing Flow

This section emphasizes modifying the OCDF-T, OCDF-R and OCDF-V models obtained in the previous studies into non-linear polynomial equations in order to determine the upstream flow depth. The conceptual derivation for both channels is presented in the following subsections.

5.2.1 Trapezoidal Cross-Sectional Channel

The general equation for the OCDF-T is given as follows:

$$\begin{aligned}&(1+2k_0)\left[\frac{1}{2}\left(1-y_r^{\,2}-Br_2y_r^{\,2}\cos\theta_2\right)+\frac{k_0}{3}\left(1-y_r^{\,3}-y_r^{\,3}\cos\theta_2\right)\right]\\&=F_0^2(1+k_0)^2\left[C\left(q_r\sin\theta_2+(1-q_r)\sin\theta_1\right)+\frac{1+k_0}{y_r}\left(\frac{(1-q_r)^2}{Br_1+k_0y_r}\cos\theta_1+\frac{q_r^{\,2}}{Br_2+k_0y_r}\cos\theta_2\right)-1\right].\end{aligned}\tag{5.1}$$

here $k_0=\frac{zy_0}{b_0}, Br_1=\frac{b_1}{b_0}$ and $Br_2=\frac{b_2}{b_1}$.

Expand (5.1), yields

$$\begin{aligned}&-\frac{F_0^2(1+k_0)^3(1-q_r)^2}{\left(Br_1y_r+k_0y_r^{\,2}\right)}\cos\theta_1-\frac{F_0^2(1+k_0)^3q_r^{\,2}}{\left(Br_2y_r+k_0y_r^{\,2}\right)}\cos\theta_2=\frac{1}{2}(1+2k_0)-\frac{y_r^{\,2}}{2}(1+2k_0)-\\&\frac{Br_2y_r^{\,2}}{2}(1+2k_0)\cos\theta_2+\frac{k_0}{3}(1+2k_0)-\frac{k_0}{3}(1+2k_0)y_r^{\,3}-\frac{k_0}{3}(1+2k_0)y_r^{\,3}\cos\theta_2+F_0^2(1+k_0)^2\\&-F_0^2C(1+k_0)^2(1-q_r)\sin\theta_1-F_0^2C(1+k_0)^2q_r\sin\theta_2.\end{aligned}\tag{5.2}$$

Equation (5.2) is unable to be solved for any values of angles θ_1 and θ_2 unless one of the angles is at 90^0. Hence, the division angles are set to be in the interval $0^0\le\theta_1\le90^0$ and eliminated $\cos\theta_2$ in (5.2) by choosing $\theta_2=90^0$, in which one of the trigonometry terms in (5.2) is eliminated. Then, both sides of the resulting equation are multiplied with $Br_1y_r+k_0y_r^{\,2}$, yields

$$\begin{aligned}&-F_0^2(1+k_0)^3(1-q_r^{\,2})\cos\theta_1=\left(Br_1y_r+k_0y_r^{\,2}\right)[\frac{1}{2}(1+2k_0)-\frac{y_r^{\,2}}{2}(1+2k_0)+\frac{k_0}{3}(1+2k_0)\\&-\frac{k_0}{3}(1+2k_0)y_r^{\,3}+F_0^2(1+k_0)^2-F_0^2C(1+k_0)^2(1-q_r)\sin\theta_1-F_0^2C(1+k_0)^2q_r].\end{aligned}\tag{5.3}$$

Expand (5.3) and rearrange in the following form:

$$-\frac{k_0^{\,2}}{3}(1+2k_0)y_r^{\,5}+\left[-\frac{Br_1k_0}{3}(1+2k_o)-\frac{k_o}{2}(1+2k_o)\right]y_r^{\,4}-\frac{Br_1}{2}(1+2k_o)y_r^{\,3}$$
$$+\left[\frac{k_o}{2}(1+2k_o)+\frac{k_o^{\,2}}{3}(1+2k_o)+F_o^{\,2}k_o(1+k_o)^2-F_o^{\,2}Ck_o(1+k_o)^2(1-q_r)\sin\theta_1-F_oCk_o(1+k_o)^2q_r\right]y_r^{\,2} \quad (5.4)$$
$$+\left[\frac{Br_1}{2}(1+2k_0)+\frac{Br_1k_0}{3}(1+2k_0)+Br_1F_0^2C(1+k_0)^2q_r\right]y_r+F_o^{\,2}(1+k_o)^3(1-q_r)^2\cos\theta_1=0.$$

From (5.4), the simplified non-linear polynomial of degree 5 is given by

$$f(y_r)=ay_r^{\,5}+by_r^{\,4}+dy_r^{\,3}+ey_r^2+ly_r+h \quad (5.5)$$

where

$$f(y_r)=0,\ a=-\frac{k_o^{\,2}}{3}(1+2k_o),\ b=-\frac{Br_1k_0}{3}(1+2k_o)-\frac{k_o}{2}(1+2k_o),\ d=-\frac{Br_1}{2}(1+2k_o),$$
$$e=\frac{k_o}{2}(1+2k_o)+\frac{k_o^{\,2}}{3}(1+2k_o)+F_o^{\,2}k_o(1+k_o)^2-F_o^{\,2}Ck_o(1+k_o)^2(1-q_r)\sin\theta_1$$
$$-F_oCk_o(1+k_o)^2q_r,\ l=\frac{Br_1}{2}(1+2k_0)+\frac{Br_1k_0}{3}(1+2k_0)+Br_1F_0^2C(1+k_0)^2q_r,$$
$$h=F_o^{\,2}(1+k_o)^3(1-q_r)^2\cos\theta_1.$$

5.2.2 Rectangular Cross-Sectional Channel

The general equation for rectangular cross-sectional channel can be retrieved from (5.1) by letting $k_0=0$. Hence, the following equation is obtained:

$$\frac{1}{2}\left(1-y_r^{\,2}-Br_2y_r^{\,2}\cos\theta_2\right)$$
$$=F_0^2\left[C\left(q_r\sin\theta_2+(1-q_r)\sin\theta_1\right)+\frac{1}{y_r}\left(\frac{(1-q_r)^2}{Br_1}\cos\theta_1+\frac{q_r^{\,2}}{Br_2}\cos\theta_2\right)-1\right]. \quad (5.6)$$

The similar steps are taken to derive the polynomial equation for the OCDF-R. Expand (5.6), yields

$$\frac{-F_0^2(1-q_r)^2}{Br_1y_r}\cos\theta_1-\frac{-F_0^2q_r^{\,2}}{Br_2y_r}\cos\theta_2=-\frac{1}{2}+\frac{y_r^{\,2}}{2}+\frac{Br_2y_r^{\,2}}{2}\cos\theta_2-F_0^2+$$
$$F_0^2C(1-q_r)\sin\theta_1+F_0^2Cq_r\sin\theta_2. \quad (5.7)$$

Then, the division angles, $0^0 \le \theta_1 \le 90^0$ and $\theta_2 = 90^0$ are considered. By eliminating one of the trigonometry in (5.7) and multiply with $Br_1 y_r$, the following equation is obtained:

$$\frac{Br_1}{2} y_r^{\,3} + \left[-\frac{Br_1}{2} - Br_1 F_0^2 + Br_1 F_0^2 C(1-q_r)\sin\theta_1 + Br_1 F_0^2 C q_r \right] y_r + F_o^{\,2}(1-q_r)^2 \cos\theta_1 = 0 \quad (5.8)$$

From (5.8), the simplified non-linear polynomial equation of degree 3 for the OCDF-R is

$$f(y_r) = j.y_r^{\,3} + k.y_r + l, \quad (5.9)$$

where:

$$f(y_r) = 0,\ j = \frac{Br_1}{2},\ k = -\frac{Br_1}{2} - Br_1 F_0^2 + Br_1 F_0^2 C(1-q_r)\sin\theta_1 + Br_1 F_0^2 C q_r,$$
$$l = F_o^{\,2}(1-q_r)^2 \cos\theta_1.$$

5.2.3 V-shaped Cross-Sectional Channel

The general equation for the V-shaped cross-sectional channel can be written as:

$$\frac{2}{3}\left[1 - y_r^{\,3} - y_r^{\,3}\cos\theta_2\right] = F_0^{\,2}\left[\frac{1}{y_r^{\,2}}\left((1-q_r)^2\cos\theta_1 + q_r^{\,2}\cos\theta_2\right) - 1 + C\left(q_r\sin\theta_2 + (1-q_r)\sin\theta_1\right)\right], \quad (5.10)$$

where $C = \frac{5}{6} - \frac{F_0^{\,2}}{40}$.

The similar steps from (5.2) until (5.4) are taken to derive the polynomial equation for the OCDF-V. Thus, the simplified non-linear polynomial equation of degree 5 for the OCDF-V can be written as:

$$f(y_r) = \frac{2}{3} y_r^{\,5} + k.y_r^{\,2} + m \quad (5.11)$$

where

$$f(y_r) = 0, k = -\frac{2}{3} - F_0^2 + F_0^2 C q_r + F_0^2 C(1-q_r)\sin\theta_1 \text{ and}$$

$$m = F_0{}^2(1-q_r)^2\cos\theta_1.$$

5.3 Newton Raphson Method

The Newton-Raphson method, which is also known as Newton's method, is an iterative numerical method used to estimate the roots of a real-valued function, $f(y_r)$ using initial guess value for the first iteration, $y_r^{(0)}$ and then approximating the next iteration, $y_r^{(1)}$ which is approximate to roots. This method originates from Taylor's series expansion of the function $f(y_r)$ about the point $y_r^{(1)}$:

$$f(y_r) = f(y_r^{(1)}) + (y_r - y_r^{(1)}) f'(y_r^{(1)}) + \frac{1}{2!}(y_r - y_r^{(1)})^2 f''(y_r^{(1)}) + \ldots \tag{5.12}$$

where f and its first and second order derivatives, f' and f'' are calculated at y_r. The first two terms of the Taylor's series expansion are considered as follows:

$$f(y_r) \approx f(y_r^{(1)}) + (y_r - y_r^{(1)}) f'(y_r^{(1)}). \tag{5.13}$$

Then set (5.13) to zero, which gives:

$$f(y_r^{(1)}) + (y_r - y_r^{(1)}) f'(y_r^{(1)}) = 0 \tag{5.14}$$

Rearranging (5.14), the next approximation to the root is obtained as:

$$y_r = y_r^{(2)} = y_r^{(1)} - \frac{f(y_r^{(1)})}{f'(y_r^{(1)})} \tag{5.15}$$

Thus, generalizing (5.15), Newton's iterative method for solving (5.5) and (5.9) is given by

$$y_r^{(i)} = y_r^{(i-1)} - \frac{f(y_r^{(i-1)})}{f'(y_r^{(i-1)})}. \tag{5.16}$$

The iteration procedure starts with an initial guess value, $y_r^{(0)}$ and continues until a predefined criterion is fulfilled. The initial value for this study is depends on the experiment results provided by Pandey & Mishra (2012). The values of $y_r^{(0)}$ for each set (R1, R2, R3) of the experiment are different. The tolerance value (Tol) is 10^{-7} and the maximum number of iterations (NOI) is 200. Based on (5.16), the Newton's method for trapezoidal channel can be written as:

$$y_r^{(i)} = y_r^{(i-1)} - \frac{a(y_r^{(i-1)})^5 + b(y_r^{(i-1)})^4 + d(y_r^{(i-1)})^3 + e(y_r^{(i-1)})^2 + g(y_r^{(i-1)}) + h}{5a(y_r^{(i-1)})^4 + 4b(y_r^{(i-1)})^3 + 3d(y_r^{(i-1)})^2 + 2e(y_r^{(i-1)}) + g} \quad (5.17)$$

where the data R1 for trapezoidal channel in Tables 5.1 and 5.2 are applied into (5.17). By using initial guess of $y_r^{(0)} = 1.03004$ and performing Newton's method up to third iteration, $i = 3$, the following solutions are obtained:

$$y_r^{(1)} = 1.00433$$
$$y_r^{(2)} = 1.00313$$
$$y_r^{(3)} = 1.00312$$

Therefore, the results achieve convergence within 3 iterations and produce the final solution $y_r \approx 1.00312$ that satisfies the stopping criteria $|f(y_r)| < 10^{-7}$. Then, similar mathematical approach are used for the rectangular and V-shaped cross-sectional channel to obtained the initial guess value and Newton's method for rectangular and V-shape channel.

Newton's method for rectangular cross-sectional channel

$$y_r^{(i)} = y_r^{(i-1)} - \frac{j(y_r^{(i-1)})^3 + k(y_r^{(i-1)}) + l}{3j(y_r^{(i-1)})^2 + k}.$$

Newton's method for V-shape cross-sectional channel:

$$y_r^{(i)} = y_r^{(i-1)} - \frac{\frac{2}{3}(y_r^{(i-1)})^5 + k(y_r^{(i-1)})^2 + m}{\frac{10}{3}(y_r^{(i-1)})^4 + 2k(y_r^{(i-1)})}.$$

Newton's method is employed to solve the non-linear polynomial equations for trapezoidal, rectangular and V-shaped cross-sectional channels in order to determine the upstream flow depth. However, the polynomial roots for three (3) set of experiment are computed using Maple software for all cross-sectional channels.

5.4 The Geometric and Hydraulic Properties of Channels

The geometrical properties of the channel junction are given in Table 5.1, while Table 5.2 shows the experimental and measured hydraulic details of the trapezoidal and rectangular channels (Pandey & Mishra, 2012). There is no experiment results for V-shape cross-sectional channel but we assume the geometric properties for V-shape channel is similar as trapezoidal channel. From Table 5.1, the value of the bottom width, b for the trapezoidal and rectangular channels has been kept different for all channels. Further, the angle of the branch for the branch channel 1 and branch channel 2 has been kept 30^0 and 90^0 respectively to the main channel. However, there are four parameters that involved in this research which are k_0, F_0, q_r and measured depth in the main channel and channel after junction (y_0 and y_1).

Table 5.1
The Geometrical Properties Of The Channel Junction

Type of channel	Channel	Bottom width (m), b	Dividing angle from the direction of flow in main channel
Rectangular	0	0.450	N/A
	1	0.350	30^0
	2	0.250	90^0
Trapezoidal	0	0.272	N/A
	1	0.172	30^0
	2	0.072	90^0
V-shaped	0	N/A	N/A
	1	N/A	30^0
	2	N/A	90^0

Table 5.2

Characteristics of the channels and flow depth measured in experiment

Type of channel		Slope side, k_0	Froude number, F_0	Discharge ratio, q_r	Measured depth (m)		Measured depth ratio (m)
					y_0	y_1	y_r
Rectangular	R1	0.000	0.238	0.380	0.1097	0.1107	1.0091
	R2	0.000	0.401	0.600	0.1146	0.1156	1.0087
	R3	0.000	0.410	0.810	0.1151	0.1163	1.0104
Trapezoidal	R1	0.226	0.303	0.435	0.1065	0.1097	1.0300
	R2	0.188	0.188	0.322	0.0885	0.0907	1.0249
	R3	0.200	0.404	0.635	0.0942	0.0995	1.0563
V-shaped	R1	N/A	0.303	0.435	0.1065	N/A	N/A
	R2	N/A	0.188	0.322	0.0885	N/A	N/A
	R3	N/A	0.404	0.635	0.0942	N/A	N/A

5.5 Results validation

Table 5.3 presents a comparison between experimental and predicted flow using a proposed non-linear polynomial equation. Three sets of experimental measured depth (R1, R2 and R3) are used to validate the predicted flow depth ratio, y_r obtained by the proposed model.

Table 5.3

Deviation percentage between measured and predicted flow depth in channel 1, y_1 and depth ratio, y_r

Type of channel		Predicted depth ratio, y_r	Predicted depth in channel 1, y_1	Deviation percentage (%) for y_r	Deviation percentage (%) for y_1
Rectangular	R1	0.9999	0.1096	0.91	0.99
	R2	1.0259	0.1176	1.70	1.73
	R3	1.0348	0.1191	2.41	2.41
Trapezoidal	R1	1.0031	0.1068	2.61	2.64
	R2	0.9970	0.0882	2.71	2.76
	R3	1.0250	0.0966	2.96	2.91
V-shaped	R1	1.0296	0.1097	N/A	N/A
	R2	1.0146	0.0898	N/A	N/A

	R3	1.0339	0.0974	N/A	N/A

For rectangular channels, R1 demonstrated the highest predictive accuracy, with a predicted depth ratio of 0.9999 and a predicted depth of 0.1096, corresponding to deviation percentages of only 0.91% and 0.99%, respectively. These values suggest near-perfect agreement with the experiment data, indicating that R1 is the most reliable model for this channel type. In contrast, R2 and R3 showed progressively higher deviations, with R3 reaching a deviation of 2.41% for both depths, y_1 and depth ratio, y_r.

For trapezoidal channels, the results showed slightly higher deviations compared to the rectangular configuration. R1 yielded a predicted depth ratio of 1.0031 and a depth value of 0.1068, with deviation percentages of 2.61% and 2.64% respectively. R2 and R3 showed increased deviations, with R3 having the highest errors which are 2.96% for y_r and 2.91% for y_1. Despite this, the R1 provided the best performance among the three tested, although the deviations suggest a slightly less precise predictive capacity in trapezoidal geometries compared to rectangular ones.

For V-shaped channels, the deviation percentages were not provided because of the limitation in experimental data. However, based on the predicted values, R1 again showed the most conservative predictions where depth ratio, y_r is 1.0296 and y_1 is 0.1097, while R3 produced the highest depth ratio and lowest depth in channel 1 (y_r is 1.0339 and y_1 is 0.0974).

In conclusion, for all cross-sectional channel the results from R1 consistently produced the lowest deviation values where such data was available, highlighting its robustness and reliability. The highest predictive accuracy was observed in rectangular channels followed by trapezoidal, while V-shaped channels require further validation due to the absence of deviation percentage data. These findings suggest that R1 may serve as the optimal model for generalized predictive applications in open-channel flow especially when model simplicity and accuracy are both prioritized.

5.6 Parametric Investigation: Comparative Flow Characteristics

Comparative prediction of flow depth is studied for trapezoidal, rectangular and V-shaped cross-sectional channels with similar flow conditions. The parametric

investigation is based on two parameters, which are the Froude number, F_0 and discharge ratio, q_r. The experimental data, R3 in Tables 5.1 and 5.2 are used as fixed variables to analyse the effect of parameters on y_r. The property values of other cases are obtained by varying each parameter, whilst keeping the other value constant. The effect of the Froude number, F_0 and discharge ratio, q_r on y_r has been analysed and shown in Tables 5.4 and 5.5.

Table 5.4
The Effect Of Discharge Ratio, q_r On Depth Ratio, y_r

q_r	y_r		
	Trapezoidal	Rectangular	V-shaped
0.2	0.96	0.96	0.99
0.4	1.00	1.00	1.00
0.6	1.02	1.03	1.01
0.8	1.03	1.03	1.02

Table 5.5
The Effect Of Froude Number, F_0 On Depth Ratio, y_r

F_0	y_r		
	Trapezoidal	Rectangular	V-shaped
0.2	1.00	1.01	1.00
0.4	1.02	1.03	1.02
0.6	1.06	1.08	1.03
0.8	1.11	1.14	1.06

Table 5.4 shows the relationship between discharge ratio and flow depth ratio for three different channel cross-sectional channel. As the discharge ratio increases from 0.2 to 0.8, indicating that a larger proportion of the total flow is directed into a branch channel, the depth ratio also gradually increases for all cross-sectional channel. For q_r = 0.2, the depth ratio in trapezoidal and rectangular is 0.96 and 0.99 for V-shaped, suggesting the branch channel receives less flow and hence has a slightly shallower depth. As the discharge ratio increases to 0.4, the depth ratio becomes 1.00 for all cross-sectional shape, indicating a balanced condition where the depth in the branch matches the main channel. Further increases in discharge ratio to 0.6 and 0.8 result in depth ratios slightly above 1.00 (1.02–1.03), meaning the branch channel begins to carry more flow

and thus has a marginally greater depth. In summary, increasing the discharge ratio generally leads to a proportional increase in depth ratio, and this behavior is consistent for trapezoidal, rectangular and V-shaped channels, demonstrating the robustness of the depth response to flow distribution at channel junctions.

Table 5.5 presents the variation of depth ratio, y_r with different Froude number, F_0 for two types of channel cross-sections which is trapezoidal, rectangular and V-shaped channels. As observed from the table, there is an increasing in the depth ratio, y_r with increasing Froude number, F_0 for all channel geometries. At the lowest flow of $F_0 = 0.2$, the depth ratios are close to 1.00 for the trapezoidal and V-shaped channel and 1.01 for the rectangular channel, indicating that when a small portion of the flow is diverted into the branch channel, the resulting depth in the branch remains nearly equal to that in the main channel. As the Froude number increases to $F_0 = 0.4$ the depth ratio gradually increases. For instance, at $F_0 = 0.6$ the depth ratio rises to 1.03 for V-shaped, 1.06 for the trapezoidal channel and 1.08 for the rectangular channel. The highest Froude number considered in the table, $F_0 = 0.8$ results in depth ratios of 1.06 for V-shaped, 1.11 for trapezoidal and 1.14 for rectangular.

In conclusions, Froude number play the major role in determining the depth ratio to avoid the overflow of water in both trapezoidal and rectangular channels. This supports the results by Kesserwani et al. (2008) that states the nonlinear models are more sensitive to Froude number. This is rational because the inflow water obviously depends on the condition of the water flow at the outflow water. However, discharge ratio plays the second most important part in determining the value of depth ratio. This happens because the discharge ratio highly depends on the hydraulic velocity of the water flow and the cross-sectional area of the water flow.

For simplicity, Figures 5.1 and 5.2 show the dependence of depth ratio on various parameters, which are Froude number, F_0 and discharge ratio, q_r respectively. Figure 5.1 shows that the depth ratio increases when the discharge ratio increases for all cross-sectional channels. The trapezoidal, rectangular and V-shaped channels have a similar value of depth ratio, y_r when $q_r = 0.4$.

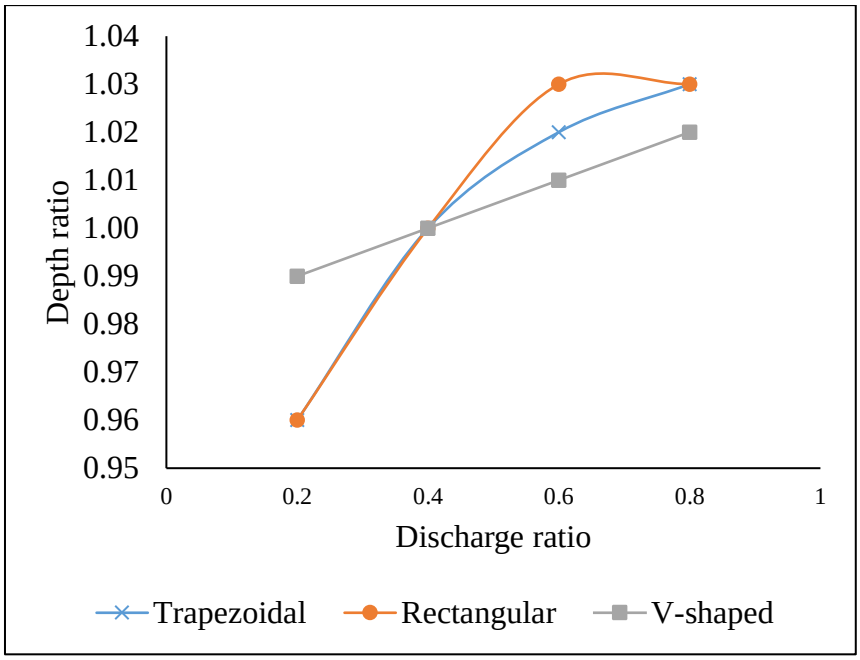


Figure 5.1 The Graph Of Effect Of Discharge Ratio On Depth Ratio For Trapezoidal, Rectangular And V-Shaped channels

In Figure 5.2, the highest value of y_r is 1.06 for V-shaped, 1.14 for the rectangular channel and 1.11 for the trapezoidal channel with the increase of F_0. In conclusion, these results give the similar pattern to (Pandey & Mishra, 2012) for trapezoidal and rectangular channel, in which the main factors to have an effect on the water depth in the branch channel system are the discharge ratio and Froude number.

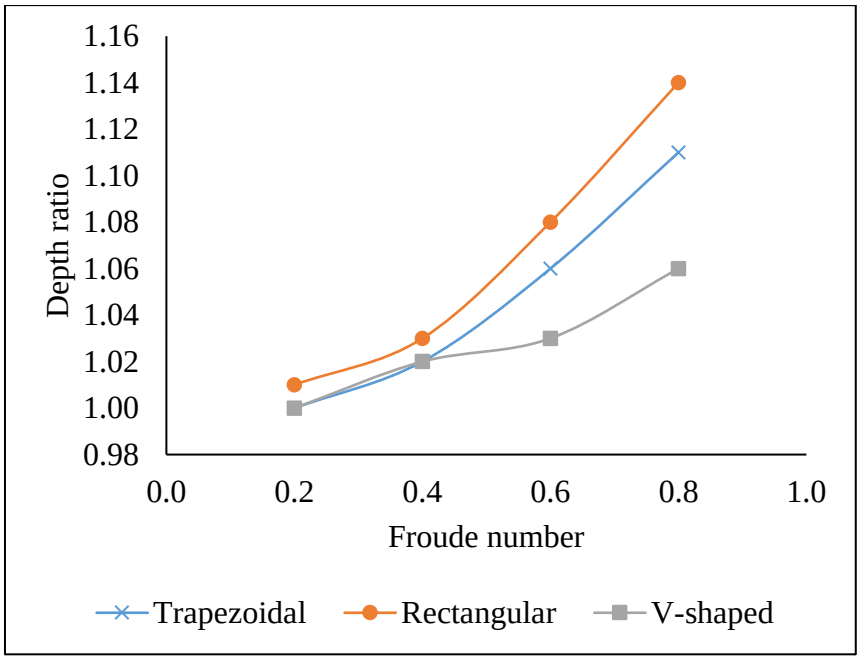


Figure 5.2 The Graph Of Effect Of Froude Number On Depth Ratio For The Trapezoidal, Rectangular And V-Shaped Channel

5.7 Conclusion

The mathematical models of open channel dividing flow have been simplified into polynomial equations by considering the division angles after junction and branch channel are $\theta_1 = 30^0$ and $\theta_2 = 90^0$ respectively. From the results analysis, Froude number and discharge ratio influence the behavior of depth flow in trapezoidal, rectangular and V-shaped channels. The results from the proposed model for trapezoidal and rectangular demonstrate a strong correlation between experimental and predicted results, with small errors. The proposed equation shows that the predicted depth matches very well with the experimental data. However, a proposed model for V-shaped channel accuracy cannot be validated because of lack of the experimental data. At low discharge ratios, all channels exhibit similar depth ratios. However, as the discharge ratio increases, the flow depth in the rectangular channel surpasses that of the V-shaped and trapezoidal channel. Moreover, as the Froude number increases, the rectangular channel experiences a consistently higher rate of flow depth increase compared to the V-shaped and trapezoidal channel. Comparing all cross-sectional channels, the values of depth ratio remain very similar across all discharge ratios, reflecting that the cross-sectional shape has a minor effect on the depth ratio under these conditions. This suggests that the influence of discharge ratio on depth ratio is predominantly governed

by flow division, and not significantly altered by channel geometry within the given range.

Overall, the results analysis demonstrates that the OCDF-T, OCDF-R and OCDF-V models in the form of non-linear polynomial equations are robust and versatile for predicting the depth ratio influenced by discharge ratio and Froude numbers. It shows higher accuracy in rectangular sections due to their simpler geometry but still maintains good predictive performance for trapezoidal channels. This validates the model's applicability for different channel shapes in open channel flow analysis, particularly in scenarios involving flow division in open-channel.

CHAPTER 6
MODELLING OF OPEN-CHANNEL DIVIDING FLOW FOR V-SHAPE CHANNEL WITH SEPARATION ZONE

6.1 Introduction

This chapter focuses on the modelling approach for open-channel dividing flow in the V-shaped cross-sectional channel that exhibits a separation zone. The separation zone shape index is defined as the ratio of the width to the length of separation zone that provides its general shape. According to previous studies, the average value of the separation zone index was between 0.17 to 0.19 and 0.2 to 0.28 (Jamshidi et al., 2016). Therefore, it is essential to examines the impact of the discharge ratio on the separation zone within the branch channel by considering different bifurcation angles in a V-shaped cross-sectional channel. The new mathematical model employs the least squares regression method, which includes the width and length of separation zone index based on the data obtained by the FLOW-3D simulation.

6.2 FLOW-3D Simulation Data

The FLOW-3D is employed to calculate the shape index of the separation zone, which is the length and width of the separation zone. The geometric properties that have been used in this study are the same as in FLOW-3D. However, the simulation data of length and width of separation zone are available only for the V-shaped cross-sectional channel with $\theta_1 = 0^0$ and $\theta_2 = 30^0, 45^0, 60^0, 75^0, 90^0$. The separation length (S_L) and separation width (S_W) were measured parallel to the branch and length of the branch channel as shown in Figure 6.1.

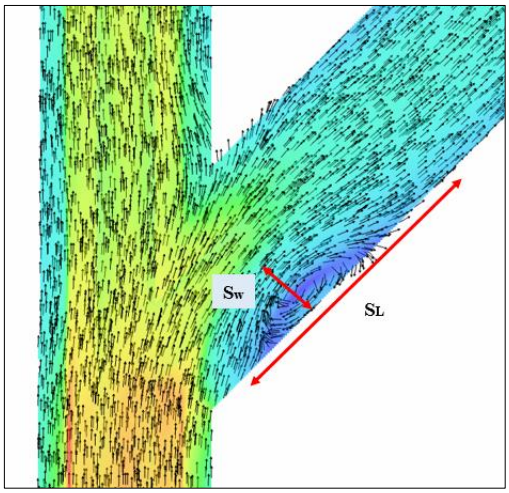


Figure 6.1 Separation Zone Length And Width In The Branch Channel

Figures 6.2 to 6.7 show the velocity distribution for each off-take angle. From these figures, the separation zone in the branch channel is developed at off-take angle of 45° to 90°. The velocity field pattern throughout the water depth presented the separation area. It can be seen that the separation area becomes larger with increasing height near the surface. The surface slice was applied for separation zone analysis as it has the highest and most significant velocity and separation zone. The separation zone usually occurs in the branch channel, in which the location and size of the separation zone are influenced by the discharge ratio, off-take angle, and bottom width of the channel. From these figures, the separation zone can be seen at the very low velocity area on the right side of the branch channel immediately after the flow is diverted into the channel.

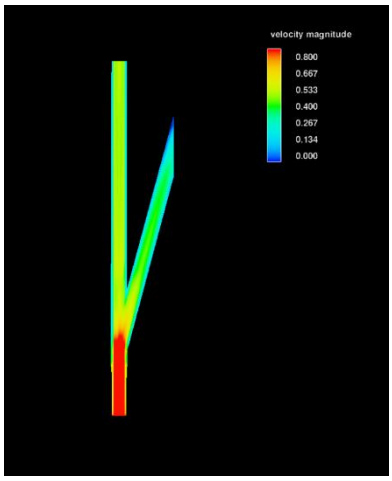


Figure 6.2 Velocity Distribution At 15°

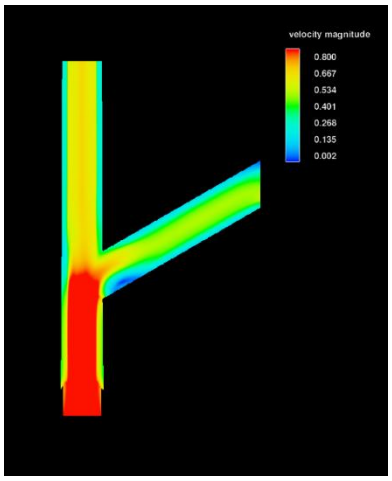


Figure 6.3 Velocity Distribution At 60°

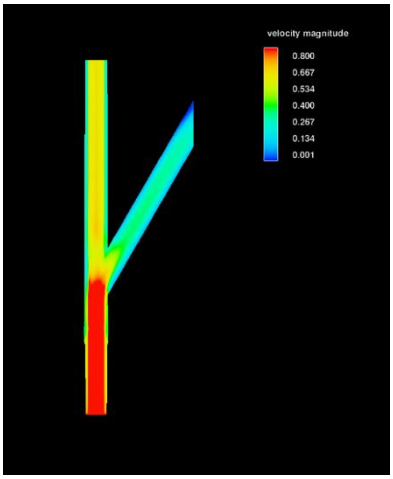


Figure 6.4 Velocity Distribution At 30°

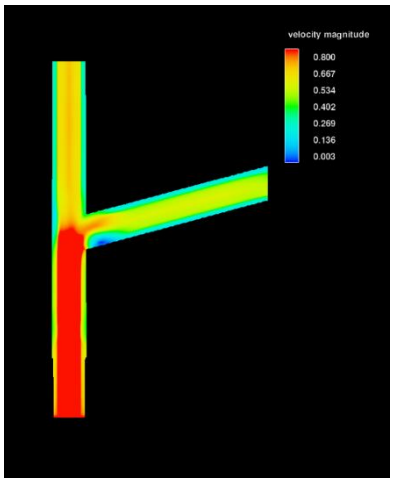


Figure 6.5 Velocity Distribution At 75°

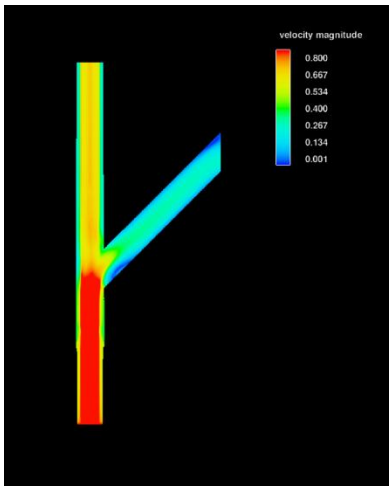


Figure 6.6 Velocity Distribution At 45°

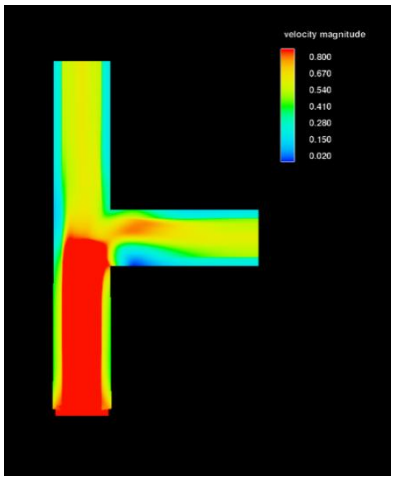


Figure 6.7 Velocity Distribution At 90°

Tables 6.1-6.5 show the dimension of separation length and width in V-shaped cross-sectional channel with various discharge ratio and dividing angles. It is observed that the average index of separation zone is between 0.0 up to 0.36.

Table 6.1
The Dimension Of The Separation Zone For $\theta_2 = 30^0$

q_r	$S_L\,(m)$	$S_W\,(m)$	Dimension		
			$\frac{S_W}{S_L}$	$\frac{S_W}{T}$	$\frac{S_L}{T}$
0.32545864	0	0	0	0	0
0.418149643	0	0	0	0	0
0.462087215	728.191	35.03118	0.048	0.117	2.427
0.518708574	768.4422	96.47989	0.126	0.322	2.561
0.561348252	0	0	0	0	0

Table 6.2
The Dimension Of The Separation Zone For $\theta_2 = 45^0$

q_r	$S_L(m)$	$S_W(m)$	Dimension		
			$\frac{S_W}{S_L}$	$\frac{S_W}{T}$	$\frac{S_L}{T}$
0.408360554	0	0	0	0	0
0.453340889	545.5093	46.8789	0.086	0.156	1.818
0.461219295	578.0312	126.1079	0.218	0.420	1.927
0.473737478	518.2615	103.6954	0.200	0.346	1.728
0.597435397	849.21	159.48	0.188	0.532	2.831

Table 6.3
The Dimension Of The Separation Zone For $\theta_2 = 60^0$

q_r	$S_L(m)$	$S_W(m)$	Dimension		
			$\frac{S_W}{S_L}$	$\frac{S_W}{T}$	$\frac{S_L}{T}$
0.486355592	0	0	0	0	0
0.51782751	434.7088	43.63727	0.100	0.145	1.449
0.555562137	592.5639	129.7885	0.219	0.433	1.975
0.510565101	551.394	142.9157	0.259	0.476	1.838
0.533843909	641.18	159.45	0.249	0.532	2.137

Table 6.4
The Dimension Of The Separation Zone For $\theta_2 = 75^0$

q_r	$S_L(m)$	$S_W(m)$	Dimension		
			$\frac{S_W}{S_L}$	$\frac{S_W}{T}$	$\frac{S_L}{T}$
0.529740859	213.62	47.94	0.224	0.160	0.712
0.454556321	387.4222	62.21937	0.161	0.207	1.291
0.537414233	576.1346	144.7322	0.251	0.482	1.920
0.540229496	540.4274	152.0265	0.281	0.507	1.801
0.589988519	543.07	171.37	0.316	0.571	1.810

Table 6.5
The Dimension Of The Separation Zone For $\theta_2 = 90^0$

q_r	$S_L(m)$	$S_W(m)$	Dimension		
			$\frac{S_W}{S_L}$	$\frac{S_W}{T}$	$\frac{S_L}{T}$
0.553243479	392.95	54.44	0.139	0.181	1.310
0.511090945	361.9209	51.38831	0.142	0.171	1.206
0.510654785	712.4971	108.379	0.152	0.361	2.375
0.509784615	549.2939	163.11	0.297	0.544	1.831
0.500326042	476.69	173.71	0.364	0.579	1.589

6.3 Mathematical Models for Dimensionless Width and Length of Separation Zone

The least squares method is the process of finding the best-fitting curve or line of best fit for a set of data points by minimising the sum of the squares of the offsets of the points from the curve. In this study, the quadratic least squares regression method is used to obtain the polynomial regression models for the dimensionless width and length of the separation zone in open-channel flow. This method is preferred for modelling nonlinear polynomial relationships because quadratic regression avoids overfitting and provides a more stable particularly when the data are limited. Although the sample size for dimensionless width and length of the separation zone is limited ($n = 5$), quadratic least squares regression is valid because the number of observations exceeds the number of unknown parameters.

By taking the difference of the estimate, or $P_n = \sum_{i=1}^{n} (y_i - (ax_i^2 + bx_i + c))^2$, then we take the partial derivative of P_n with respect to a and set the equation equal to zero.

$$\frac{\partial(P_n)}{\partial a} = -2\sum_{i=1}^{n} x_i^2 \left[y_i - (ax_i^2 + bx_i + c) \right] = 0 \tag{6.1}$$

Then, divide (6.1) by -2 gives

$$\sum_{i=1}^{n} x_i^2 \left[y_i - (ax_i^2 + bx_i + c) \right] = 0 \tag{6.2}$$

Distribute the x_i^2 term in (6.2), yields

$$\sum_{i=1}^{n}(y_i x_i^2 - ax_i^4 - bx_i^3 - cx_i^2) = 0 \tag{6.3}$$

Rearrange (6.3) to obtain

$$a\sum_{i=1}^{n} x_i^4 + b\sum_{i=1}^{n} x_i^3 + c\sum_{i=1}^{n} x_i^2 = \sum_{i=1}^{n} y_i x_i^2 \tag{6.4}$$

By using the similar step (6.2) - (6.4), find the partial of derivative of P_n with respect to b.

$$\frac{\partial(P_n)}{\partial b} = -2\sum_{i=1}^{n} x_i \left[y_i - (ax_i^2 + bx_i + c) \right] = 0 \tag{6.5}$$

Rearrange (6.5) to obtain

$$a\sum_{i=1}^{n} x_i^3 + b\sum_{i=1}^{n} x_i^2 + c\sum_{i=1}^{n} x_i = \sum_{i=1}^{n} y_i x_i \tag{6.6}$$

Then, find the partial derivative of P_n with respect to

$$\frac{\partial(P_n)}{\partial c} = -2\sum_{i=1}^{n} \left[y_i - (ax_i^2 + bx_i + c) \right] = 0 \tag{6.7}$$

Rearrange (6.7) to obtain

$$a\sum_{i=1}^{n} x_i^2 + b\sum_{i=1}^{n} x_i + \sum_{i=1}^{n} c = \sum_{i=1}^{n} y_i \tag{6.8}$$

Notice that $\sum_{i=1}^{n} c = cn$. Thus, the equation becomes:

$$a\sum_{i=1}^{n} x_i^2 + b\sum_{i=1}^{n} x_i + cn = \sum_{i=1}^{n} y_i \tag{6.9}$$

The Cramer's Rule is employed to solve the linear system of equations that is formed by (6.4), (6.6) and (6.8). In this method, the values of the variables in the system are calculated using the determinants of matrices, M :

$$M = \begin{vmatrix} \sum_{i=1}^{n} x_i^4 & \sum_{i=1}^{n} x_i^3 & \sum_{i=1}^{n} x_i^2 \\ \sum_{i=1}^{n} x_i^3 & \sum_{i=1}^{n} x_i^2 & \sum_{i=1}^{n} x_i \\ \sum_{i=1}^{n} x_i^2 & \sum_{i=1}^{n} x_i & n \end{vmatrix}.$$

Therefore, the matrices a, b and c becomes

$$a = \frac{\begin{vmatrix} \sum_{i=1}^{n} y_i x_i^2 & \sum_{i=1}^{n} x_i^3 & \sum_{i=1}^{n} x_i^2 \\ \sum_{i=1}^{n} y_i x_i & \sum_{i=1}^{n} x_i^2 & \sum_{i=1}^{n} x_i \\ \sum_{i=1}^{n} y_i & \sum_{i=1}^{n} x_i & n \end{vmatrix}}{M}, b = \frac{\begin{vmatrix} \sum_{i=1}^{n} x_i^4 & \sum_{i=1}^{n} y_i x_i^2 & \sum_{i=1}^{n} x_i^2 \\ \sum_{i=1}^{n} x_i^3 & \sum_{i=1}^{n} y_i x_i & \sum_{i=1}^{n} x_i \\ \sum_{i=1}^{n} x_i^2 & \sum_{i=1}^{n} y_i & n \end{vmatrix}}{M}, c = \frac{\begin{vmatrix} \sum_{i=1}^{n} x_i^4 & \sum_{i=1}^{n} x_i^3 & \sum_{i=1}^{n} y_i x_i^2 \\ \sum_{i=1}^{n} x_i^3 & \sum_{i=1}^{n} x_i^2 & \sum_{i=1}^{n} y_i x_i \\ \sum_{i=1}^{n} x_i^2 & \sum_{i=1}^{n} x_i & \sum_{i=1}^{n} y_i \end{vmatrix}}{M}$$

Next, find the determinant of M using cofactor expansion,

$$= \sum_{i=1}^{n} x_i^2 \begin{vmatrix} \sum_{i=1}^{n} x_i^2 & \sum_{i=1}^{n} x_i \\ \sum_{i=1}^{n} x_i & n \end{vmatrix} - \sum_{i=1}^{n} x_i^3 \begin{vmatrix} \sum_{i=1}^{n} x_i^3 & \sum_{i=1}^{n} x_i \\ \sum_{i=1}^{n} x_i^2 & n \end{vmatrix} + \sum_{i=1}^{n} x_i^2 \begin{vmatrix} \sum_{i=1}^{n} x_i^3 & \sum_{i=1}^{n} x_i^2 \\ \sum_{i=1}^{n} x_i^2 & \sum_{i=1}^{n} x_i \end{vmatrix}$$

$$= \sum_{i=1}^{n} x_i^4 \left(n \sum_{i=1}^{n} x_i^2 - \left(\sum_{i=1}^{n} x_i \right)^2 \right) - \sum_{i=1}^{n} x_i^3 \left(n \sum_{i=1}^{n} x_i^3 - \sum_{i=1}^{n} x_i^2 \sum_{i=1}^{n} x_i \right) + \sum_{i=1}^{n} x_i^2 \left(\sum_{i=1}^{n} x_i^3 \sum_{i=1}^{n} x_i - \left(\sum_{i=1}^{n} x_i^2 \right)^2 \right) \quad (6.10)$$

Similarly, find the determinant of M to determine a, b and c.

$$a = \frac{\sum_{i=1}^{n} y_i x_i^2 \left(n \sum_{i=1}^{n} x_i^2 - \left(\sum_{i=1}^{n} x_i \right)^2 \right) - \sum_{i=1}^{n} x_i^3 \left(n \sum_{i=1}^{n} y_i x_i - \sum_{i=1}^{n} x_i \sum_{i=1}^{n} y_i \right) + \sum_{i=1}^{n} x_i^2 \left(\sum_{i=1}^{n} x_i \sum_{i=1}^{n} y_i x_i - \sum_{i=1}^{n} x_i^2 \sum_{i=1}^{n} y_i \right)}{M} \quad (6.11)$$

$$b = \frac{\sum_{i=1}^{n} x_i^4 \left(n\sum_{i=1}^{n} y_i x_i - \sum_{i=1}^{n} x_i \sum_{i=1}^{n} y_i \right) - \sum_{i=1}^{n} y_i x_i^2 \left(n\sum_{i=1}^{n} x_i^3 - \sum_{i=1}^{n} x_i^2 \sum_{i=1}^{n} x_i \right) + \sum_{i=1}^{n} x_i^2 \left(\sum_{i=1}^{n} x_i^3 \sum_{i=1}^{n} y_i - \sum_{i=1}^{n} x_i^2 \sum_{i=1}^{n} y_i x_i \right)}{M} \quad (6.12)$$

$$c = \frac{\sum_{i=1}^{n} x_i^4 \left(\sum_{i=1}^{n} x_i^2 \sum_{i=1}^{n} y_i - \sum_{i=1}^{n} y_i x_i \sum_{i=1}^{n} x_i \right) - \sum_{i=1}^{n} x_i^3 \left(\sum_{i=1}^{n} x_i^3 \sum_{i=1}^{n} y_i - \sum_{i=1}^{n} x_i^2 \sum_{i=1}^{n} y_i x_i \right) + \sum_{i=1}^{n} y_i x_i^2 \left(\sum_{i=1}^{n} x_i^3 \sum_{i=1}^{n} x_i - \left(\sum_{i=1}^{n} x_i^2 \right)^2 \right)}{M} \quad (6.13)$$

Equations (6.11) to (6.13) are the least squares coefficients a, b and c for quadratic model, $y = ax^2 + bx + c$. The discharge ratio is the independent variable (x-intercept), while the value of the separation zone shape index is the dependent variable (y-intercept) for the regression.

6.4 Least Squares Regression Model for Length of The Separation Zone

This section presents the polynomial least square regression for the V-shaped cross-sectional channel. From Tables 6.1-6.5, the discharge ratio and length of the separation zone with the different angles of the branch channel 2 is applied in Section 6.3 using Maple software, where the value of $k = 2$. The following steps show the computation of the least squares regression model for length of the separation zone (LSMLS).

Step 1: Define the value for discharge ratio and length of the separation zone. For example: $\theta_2 = 30^0$.

>dr:= [0.33,0.42,0.46,0.52,0.56]

>ls:= [0,0,2.43,2.56,0]

Step 2: Define equations using Maple's mathematical functions.

>fit[leastsquare[[qr,SL/T],y=a*qr^2+b*qr+c]]([dr,ls]):

Step 3: Solving the equation and display the LSMLS.

>SL/T:= unapply(rhs(%),qr)

The polynomial least squares models with length of separation zone (LSMLS) are obtained as follows:

For $\theta_2 = 30^0$:

$$\frac{S_L}{T} = -107.8555238q_r^{\,2} + 101.0313617q_r - 21.95840112. \tag{6.14}$$

For $\theta_2 = 45^0$:

$$\frac{S_L}{T} = -142.7342356q_r^{\,2} + 158.5034774q_r - 40.89982433. \tag{6.15}$$

For $\theta_2 = 60^0$:

$$\frac{S_L}{T} = -723.7069509q_r^{\,2} + 788.6701281q_r - 212.7059413. \tag{6.16}$$

For $\theta_2 = 75^0$:

$$\frac{S_L}{T} = 40.83997676q_r^{\,2} - 37.94457996q_r + 10.06248055. \tag{6.17}$$

For $\theta_2 = 90^0$:

$$\frac{S_L}{T} = -1078.519870q_r^{\,2} + 1132.021856q_r - 295.0130794. \tag{6.18}$$

where S_L is the length of the separation zone, T is the top width of branch channel 2, and q_r is the discharge ratio.

6.5 Least Squares Regression Model for Width of The Separation Zone

The similar technique as described in the previous section is applied to derive the polynomial least square regression for the discharge ratio and width of the separation zone in V-shaped cross-sectional channel. The following steps show the computation of the least squares regression model for length of the separation zone (LSMWS).

Step 1: Define the value for discharge ratio and width of the separation zone. For example: $\theta_2 = 30^0$.

>dr:= [0.33,0.42,0.46,0.52,0.56]

>ws:= [0,0,0.117,0.322,0]

Step 2: Define equations using Maple's mathematical functions.

>fit[leastsquare[[qr,SW/T],y=a*qr^2+b*qr+c]]([dr,ws]):

Step 3: Solving the equation and display the LSMWS.

>SW/T:= unapply(rhs(%),qr)

The polynomial least squares models with width of separation zone (LSMWS) can be obtained as follows:

For $\theta_2 = 30^0$:

$$\frac{S_W}{T} = -6.296913686 q_r^{\,2} + 6.229463180 q_r - 1.404167336. \tag{6.19}$$

For $\theta_2 = 45^0$:

$$\frac{S_W}{T} = -26.61285805 q_r^{\,2} + 29.74672466 q_r - 7.736251351. \tag{6.20}$$

For $\theta_2 = 60^0$:

$$\frac{S_W}{T} = -149.2805740 q_r^{\,2} + 163.3456159 q_r - 44.21180645. \tag{6.21}$$

For $\theta_2 = 75^0$:

$$\frac{S_W}{T} = 13.99688538 q_r^{\,2} - 11.72995494 q_r + 2.642121370. \tag{6.22}$$

For $\theta_2 = 90^0$:

$$\frac{S_W}{T} = 167.9942886 q_r^{\,2} - 183.4794559 q_r + 50.28308236. \tag{6.23}$$

where S_W is the width of the separation zone, T is the top width of branch channel 2, and q_r is the discharge ratio. The data of length and width of separation zone produced by the FLOW-3D are utilised to obtain the quadratic polynomial least squares regression models. These models are essential for the derivation of the proposed mathematical models that will be discussed in the next section.

6.6 Modelling of Open-Channel Dividing Flow with Separation Zone Shape Index

A new modelling of open-channel dividing flow will be developed based on the OCDF-V model obtained in Chapter 3 and least squares regression models in Sections 6.4 and 6.5. By using algebraic manipulation and several simplification techniques, the modelling will take into account the length and width of the separation zone index in a V-shaped cross-sectional channel (OCDFS-V). The model is referred to as OCDFLS-V when considering the length of separation and OCDFWS-V when considering the width of separation zone. All channels are assumed to have the same width. The hydraulic depth, $D = \frac{A}{T}$, from the Froude number is employed, where $T = \frac{S_L}{LSM}$ or $T = \frac{S_W}{LSM}$. Therefore, the established hydraulic depths are given

$$D = \frac{A}{\left(\frac{S_L}{LSM_{S_L}}\right)} \tag{6.24}$$

$$D = \frac{A}{\left(\frac{S_W}{LSM_{S_W}}\right)} \tag{6.25}$$

Equations (6.24) or (6.25) are substituted into (3.18) to obtain the OCDFS-V model:

$$\begin{aligned} &\frac{2}{3}\left[1 - {y_r}^3 - {y_r}^3 \cos\theta_2\right] \\ &= {F_{LSM}}^2 \left[\frac{1}{{y_r}^2}\left(\left(1-q_r\right)^2 \cos\theta_2 + {q_r}^2 \cos\theta_1\right) - 1 + C\left(q_r \sin\theta_1 + \left(1-q_r\right)\sin\theta_2\right)\right], \end{aligned} \tag{6.26}$$

where the established Froude number is

$$F_{LSM} = \frac{V}{\sqrt{g\left(\frac{A}{\left(\frac{S_L}{LSM_{S_L}}\right)}\right)}} \quad \text{or} \quad F_{LSM} = \frac{V}{\sqrt{g\left(\frac{A}{\left(\frac{S_W}{LSM_{S_W}}\right)}\right)}}$$

6.7 Results Analysis

The new mathematical model (6.26) is used to calculate the discharge ratio with the dimensionless length and width of the separation zone. The credibility of the proposed models is shown by computing the discharge ratio based on the division angles $\theta_1 = 0^0$ and $\theta_2 = 30^0, 45^0, 60^0, 75^0, 90^0$. The results are divided into two sections: discharge ratio with the length of separation zone and discharge ratio with the width of separation zone.

6.7.1 Discharge Ratio with Length of Separation Zone

There are four (4) possible values of discharge ratio with the length of the separation zone are presented in Table 6.6. For $\theta_1 = 0°$, the discharge ratio is less than the critical ratio for all angles in branch 2, θ_2. Although the discharge ratio at $\theta_2 = 75°$ shows complex value, the model is able to obtain the real solutions for other division angles. There is a value of discharge ratio that approaches to zero. However, for the hydraulic analysis, the real part of the complex value is also considered as discharge ratio.

Table 6.6
The Discharge Ratio Obtained By The OCDFLS-V

θ_2	Discharge ratio, q_r			
30°	0.342661196	0.344200084	0.592028476	0.594017024
45°	0.407724358	0.408413867	0.702022818	0.702728785
60°	0.490220043	0.490642754	0.59911672	0.599538275
75°	0.00004506875956	0.4646746909 + 0.1723006230I	0.464606993 + 0.1750145482I	N/A
90°	0.48138532970000	0.481767195	0.567862063	0.568219426

6.7.2 Discharge Ratio with Width of Separation Zone

The discharge ratio in the V-shaped cross-sectional channels with the width of the separation zone is presented in Table 6.7. The discharge ratio is the form of complex value when $\theta_2 = 75°$ and $90°$, while some values approach zero. Overall, the discharge ratio is less than the critical discharge ratio for all division angles, including the real part of complex values.

Table 6.7
The Discharge Ratio Obtained By The OCDFWS-V

θ_2	Discharge ratio			
30°	0.347341895	0.348375279	0.64062594	0.641911896
45°	0.411687816	0.412434116	0.705286188	0.706041805
60°	0.490836489	0.491352978	0.602860745	0.603374674
75°	0.00004804957043	0.4192251484 + 0.1118705193I	0.4190776364 + 0.1150462288I	N/A
90°	0.000002806268124	0.5460599564 + 0.03217914585I	0.5460905621 + 0.03324130972I	N/A

6.8 Results validation

The discharge ratio with varying division angles obtained by the OCDF-V model from Chapter 3 and FLOW-3D are presented in Table 6.8. Interestingly, there is a similar trend between the OCDF-V model and computational FLOW-3D. This is counter-intuitive because it is expected that the separation zone will affect the discharge ratio.

Table 6.8
The Discharge Ratio Obtained By The OCDF-V And FLOW-3D

θ_2	OCDF-V	FLOW-3D
30°	0.575664164	0.561348252
45°	0.586674292	0.597435397
60°	0.573716916	0.533843909
75°	0.525085782	0.589988519
90°	1.000084685	0.500326042

To validate the performance of the OCDFLS-V and OCDFWS-V, the absolute error or deviation percentage is determined by evaluating the difference between the discharge ratio of the proposed models and OCDF-V with FLOW-3D simulation data.

Table 6.9
The Comparison Of Deviation Percentage Between OCDF-V, OCDFLS-V And OCDFWS-V Models

Division angles θ_2	Deviation percentage (%)								
	OCDF-V	OCDFLS-V				OCDFWS-V			
30°	2.55	38.96	38.68	5.47	5.82	38.12	37.94	14.12	14.35
45°	1.80	31.75	31.64	17.51	17.62	31.09	30.97	18.05	60.16
60°	7.47	8.17	8.09	12.23	12.31	8.06	7.96	12.93	53.78
75°	11.00	99.99	21.24	21.25	N/A	99.99	28.94	28.97	N/A
90°	99.89	3.79	3.71	13.50	13.57	100.00	9.14	9.15	N/A

Table 6.9 presents a comparison of deviation percentages across different division angles, 30°, 45°, 60°, 75°, and 90° for OCDF-V, OCDFLS-V, and OCDFWS-V. At lower dividing angles such as 30° and 45°, the OCDF-V model performs with high accuracy, showing very low deviation percentages (as low as 1.80% to 2.55%), while both the OCDFLS-V and OCDFWS-V models demonstrate significantly higher deviations, exceeding 30% in most cases. This indicates that OCDF-V is more reliable for smaller division angles.

As the division angle increases to 60°, OCDF-V's accuracy begins to decline, though it still performs reasonably well (around 7–12% deviation). Interestingly, at this angle, the OCDFLS-V and OCDFWS-V models improve in accuracy, showing deviations around 8%, suggesting better suitability of these models for moderate angles. At 75°, OCDF-V records a deviation of 11% signaling a breakdown in performance. Meanwhile, OCDFLS-V and OCDFWS-V show higher derivation percentage, pointing to numerical instability or convergence issues at steep angles.

At the extreme case of a 90° bifurcation, OCDF-V again fails with near 100% deviation, confirming its unsuitability for perpendicular divisions or right-angled channel. In contrast, OCDFLS-V and OCDFWS-V offer improved results with deviations as low as 3.7%, though some values remain unavailable, again indicating

limitations in model robustness, these results are consistent with the findings of Zakaria et al. (2025). Overall, the analysis reveals that OCDF-V is well-suited for small division angles, while OCDFLS-V and OCDFWS-V become more reliable at larger angles despite some stability concerns.

Figure 6.8 illustrates the graph of deviation percentage for OCDFLS-V and OCDFWS-V across various division angles at channel 2 (30°, 45°, 60°, 75°, and 90°). The figure compares both maximum and minimum deviation percentages for the OCDFLS-V and OCDFWS-V models, as well as a single deviation value for OCDF-V.

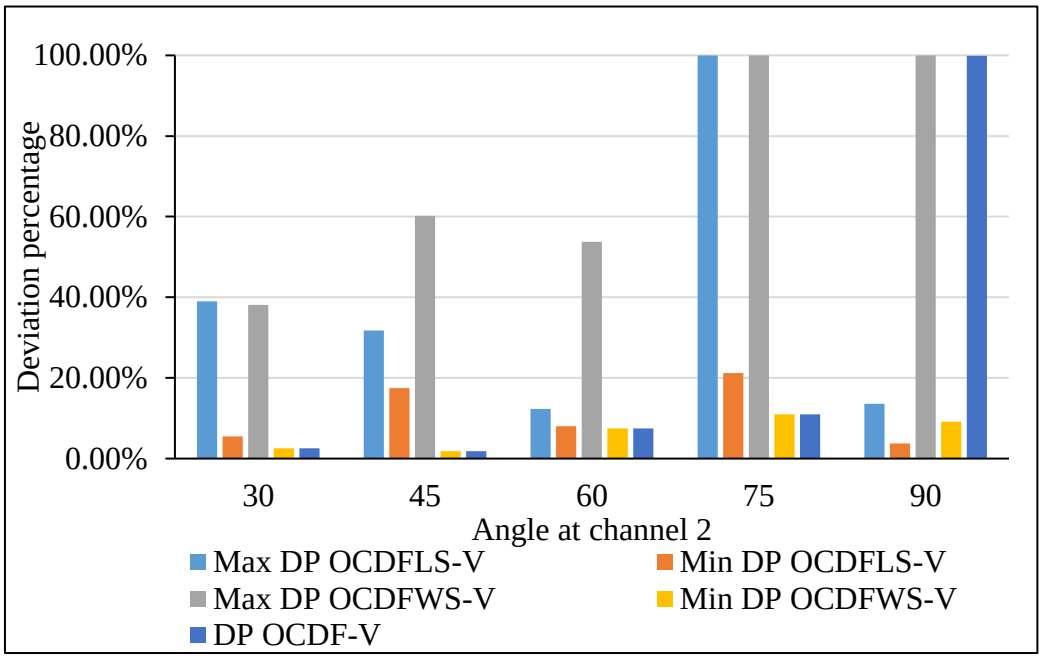


Figure 6.8 The Graphs Of Maximum And Minimum Deviation Percentage For OCDFLS-V And OCDFWS-V Models

At 30°, the OCDF-V model shows a low deviation (2.55%), indicating high accuracy. Both OCDFLS-V and OCDFWS-V models exhibit higher maximum deviations (around 39%) but much lower minimum deviations (<6%), suggesting inconsistency in their performance at this angle.

As the angle increases to 45°, the OCDF-V deviation rises slightly, while OCDFLS-V and OCDFWS-V again show a large gap between their maximum and minimum deviations, with OCDFWS-V reaching 60%. The minimum deviations for both OCDFLS-V and OCDFWS-V are very low, indicating that these models can outperform OCDF-V, which has a higher deviation.

At 60°, deviations from most of the models become closer, where OCDF-V and both variants of OCDFLS-V and OCDFWS-V hover around 10–15%, showing relatively balanced and improved accuracy at moderate angles. However, at 75°, both OCDFLS-V and OCDFWS-V reach their maximum deviation of 99.99%, indicating a critical failure or breakdown in performance. The OCDF-V also shows a notable increase, but less severe. Although the maximum deviation for OCDFLS-V and OCDFWS-V are higher than OCDF-V's, their minimum values are competitive, showing strong potential for accurate predictions in moderate-angle dividing channel with separation zone.

Finally, at 90°, the OCDF-V shows very high maximum deviations (up to 100%), indicating failure or significant divergence. However, both OCDFLS-V and OCDFWS-V again demonstrate low minimum deviations (around 9%), highlighting high accuracy. This reinforces the robustness of OCDFLS-V and OCDFWS-V under complex, high-angle flow divisions when optimal conditions are met.

6.9 Conclusion

The performance of the mathematical models has been verified by comparing the results with computational FLOW-3D. The significant difference in the results between the proposed models and simulation data is most probably due to the assumptions made in the mathematical modeling, in which the velocities and water surface elevations are constant across the channels, the pressure distribution is hydrostatic at all sections of the control volume, and the effect of vertical acceleration and the wall friction force as compared to other forces are neglected. There will be flow separation in the vicinity of the junction, especially at the branch channel. The flow will slowly adapt to the change in geometry, and this provides an area of circulation near the wall at the inside part of the branch.

In conclusion, while OCDFLS-V and OCDFWS-V may exhibit variability as seen in the wide range between their minimum and maximum deviations, their ability to produce very low deviation percentages in some cases suggests that they are potentially more accurate and adaptable than OCDF-V, especially at moderate to large division angles. This makes them preferable choices for more complex hydraulic modeling where sensitivity and dynamic flow conditions are expected

CHAPTER 7
CONCLUSION

7.1 Conclusion

This thesis has provided a comprehensive exploration of bifurcation flow in open channels through mathematical modelling, focusing on understanding the dynamics and implications of flow bifurcation. Each chapter has contributed to a holistic view of the study, leading to significant findings and future directions.

Chapter 1 introduced the fundamental concepts of open-channel flow and the significance of bifurcation or diversion phenomena. The objectives of this study are to derive a new general equation for open-channel dividing flow in V-shaped cross-sectional channels based on momentum principles and mass continuity, and to develop mathematical models for open-channel dividing flow that incorporate dimensionless width and length of the separation zone in trapezoidal, rectangular and V-shaped cross-sectional channels. Additionally, the study aims to analyse the discharge ratio and flow depth in open-channel dividing flow, validate the accuracy of the proposed models through comparisons with FLOW-3D simulations, and create a graphical user interface (GUI) for these models using Maple software. It also outlined the significance, scope and limitation of the research, setting the stage for the subsequent chapters.

Chapter 2 reviewed relevant literature and established the theoretical framework. One of the gaps in the existing literature is the limited study of the separation zone in open-channel flow, particularly with mathematical modelling. This chapter highlighted previous models and identified gaps that our research aimed to address, specifically focusing on the cross-sectional channel in open-channel flow, which is the V-shaped channel.

Chapter 3 presented the mathematical formulation of the flow model, detailing the governing equations and boundary conditions for trapezoidal, rectangular and V-shaped cross-sectional channel. The derivation of these equations laid the foundation for understanding the flow dynamics. However, the mathematical formulation for trapezoidal and rectangular cross-sectional channel was derived by previous study. The relation between discharge ratio and bifurcation angles has been analysed and discussed with two case which are case 1 investigates the constant width of the channel, whereas

case 2 investigates the different width of the channel. The discussion shows that case 1 shows that trapezoidal and rectangular tends to not overflow by any bifurcation angles but for case 2, V-shaped channels has produced the discharge ratio below the critical discharge. The discharge ratio must be lesser than the critical discharge to prevent the channel from overflow and the discharge ratio is affected by the bifurcation angles.

Chapter 4 examines the relationship between the discharge ratio and bifurcation angles in trapezoidal, rectangular and V-shaped cross-sectional channels, with particular emphasis on the incorporation of the Reynold's number into the mathematical model. The results indicate that the Reynold's number serves as a valuable alternative parameter in the proposed model, which can be utilized to design and optimize the dimensions of such channels. In open channel flow, the discharge distribution is influenced by the Reynold's number, which affects mixing and momentum transfer between branches. By including the Reynold's number in the mathematical formulation, the model can more accurately simulate discharge behavior, particularly in regions where flow separation or other complex flow phenomena occur.

Chapter 5 explored various scenarios of bifurcation flow, analyzing the effects of flow depth in the channel using the mathematical models of dividing flow in trapezoidal, rectangular and V-shaped cross-sectional in the form of nonlinear polynomial equations. The proposed equations are solved using Newton-Raphson procedure to determine the upstream flow depth. The results from the proposed model demonstrate a strong correlation between experimental and predicted results. The proposed equation shows that the predicted depth, y_r matches very well with the experimental data. The results illustrated how changes in channel geometry and flow conditions can lead to significant bifurcation phenomena, providing insights into practical implications for hydraulic engineering.

Chapter 6 focused on the numerical methods employed to resolve the mathematical model for the V-shaped cross-sectional channel, which includes characteristics of an open channel with dividing flow, which is the separation zone, implementing the quadratic least squares regression approach. The discharge ratio results for the V-shaped cross-sectional channel, considering the width and length of the separation zone, indicate that it is below to the critical discharge ratio for all bifurcation angles in branch 2. We established the robustness of the new mathematical model and general equation by validating the model's accuracy and efficiency using the

FLOW-3D simulation. The validation shows that a comparable pattern exists between new mathematical models featuring a separation zone and computational FLOW-3D, although a divergent trend is observed with the general equation. In conclusion, the separation zone will influence the discharge ratio in an open-channel bifurcation flow.

Chapter 7 discusses the broader implications of our findings, including potential applications in environmental management and infrastructure design. This chapter emphasized the importance of understanding bifurcation flows in addressing ecological and engineering challenges. This research demonstrated that bifurcation flows exhibit complex behaviors influenced by various factors, including channel shape, flow rate, and sediment transport. The developed mathematical model effectively captures these dynamics, contributing valuable insights to both theoretical and practical domains. In conclusion, the mathematical modelling of bifurcation flow in open channels is a vital area of study with significant implications for water resource management and environmental sustainability. This thesis not only advances our understanding of these phenomena but also opens avenues for future research that can lead to more resilient and adaptive water management strategies

7.2 Future Research

In future research, it is recommended to study the mathematical models of dividing flow equation by considering the Saint-Venant equation in the form of hyperbolic partial differential equations. Additional cross-sectional channel shapes and features, incorporating other parameters such as hydraulic jumps, separation zones, and surface discontinuities might be considered. It is also recommended to apply other shapes of cross-sectional channel such as semi-circular or composite trapezoidal, which combines the standard trapezoidal section with another section, often a rectangular or semi-circular for practical and more realistic channel design. The models of dividing flow for all channels should be extended for analysing the behaviour of flow depth in open-channel flow. Since this research only focuses on the dividing flow channel, the study of combining flow for other cross-sectional channels that include the separation zone and Reynold's number may be considered for future research. Nevertheless, researchers can evaluate the effectiveness of the proposed models for all types of channels by validating the results with CFD simulations. Future studies are encouraged to incorporate experimental investigations to complement and further validate the

theoretical findings presented in this work. Furthermore, this study has primarily focused on the investigation of flow characteristics and separation zones within V-shaped open channels. Future research is encouraged to explore others channel cross-sections to assess how the separation zone behaves under varying geometric conditions. This could lead to a more comprehensive understanding of flow behavior in diverse practical applications. Expanding the scope beyond V-shaped channels would help validate and extend the current findings and may uncover geometry-specific phenomena that were not captured in this study.

REFERENCES

A, K. S., S, I. N., J, L., & Eze, M. O. (2015). Simulation of 2D Saint-Venant equations in open channel by using MATLAB. *Journal of IT in Asia*.

Abd Elmoaty, M. S., & T. A, E. S. (2020). Manning roughness coefficient in vegetated open channels. *Water Science*, *34*(1), 121–128. https://doi.org/10.1080/11104929.2020.1794706

Abdurrasheed Sa'id Abdurrasheed, K. W., Hamid, E., Alqadami, H., Takaijudin, H., Ghani, A. A., Muhammad, M. M., Sholagberu, A. T., Zainalfikry, M. K., Osman, M., & Patel, M. S. (2019). Modelling of Flow Parameters through Subsurface Drainage Modules for Application in BIOECODS. *Water*, *11*(1823), 1–15. https://doi.org/10.3390/w11091823

Ac, C., Jk, K., & Js, M. (2021). The effect of a difference in angle in two lateral inflow channels on the main channel's velocity. *Journal of Statistics and Applied Mathematics*, *6*(3), 30–36. http://www.mathsjournal.com

Ahammed, N., Asirvatham, L. G., & Wongwises, S. (2016). Effect of volume concentration and temperature on viscosity and surface tension of graphene-water nanofluid for heat transfer applications. *Journal of Thermal Analysis and Calorimetry*, *123*(2), 1399–1409. https://doi.org/10.1007/s10973-015-5034-x

Alfatlawi, T. J., & Hussein, A. H. (2024). A Review of Studying the Flow Characteristics in Branching Open Channels. In *International Journal of Heat and Technology* (Vol. 42, Number 2, pp. 560–566). International Information and Engineering Technology Association. https://doi.org/10.18280/ijht.420222

Alfatlawi, T. J. M., & Hussein, A. H. (2024). A numerical study of diversion flow to determine the optimum flow system in open channels. *Water Practice & Technology*, *19*(4), 1330–1347. https://doi.org/10.2166/wpt.2024.056

Ali, H., & Elhamaimi, A. (2020). An Experimental and Numerical Investigation for Characteristics of Submerged Hydraulic Jump over Corrugated Beds. *Port-Said Engineering Research Journal*, *0*(0), 0–0. https://doi.org/10.21608/pserj.2020.18744.1015

Alomari, N. K., Yusuf, B., & Mohammad, T. A. (2016). Flow in a Branching Open Channel : A Review Flow in a Branching Open Channel : A Review. *Pertanika Journal of Scholarly Research Reviews*, *2(2)*(June), 40–56.

Alomari, N. K., Yusuf, B., Mohammad, T. A., & Ghazali, A. H. (2018). Experimental investigation of scour at a channel junctions of different diversion angles and bed width ratios. *Catena*, *166*, 10–20. https://doi.org/10.1016/j.catena.2018.03.013

Alomari, N. K., Yusuf, B., Mohammad, T. A., & Ghazali, A. H. (2020). Influence of diversion angle on water and sediment flow into diversion channel. *International Journal of Sediment Research*, *35*(6), 600–608. https://doi.org/10.1016/j.ijsrc.2020.06.006

Azimi, H., & Shabanlou, S. (2016). Comparison of Subcritical and Supercritical Flow Patterns Within Triangular Channels Along the Side Weir. *International Journal of Nonlinear Sciences and Numerical Simulation*, *17*(7–8), 361–368. https://doi.org/10.1515/ijnsns-2015-0103

Azma, A., & Zhang, Y. (2020a). The effect of variations of flow from tributary channel on the flow behavior in a T-shape confluence. *Processes*, *8*(5). https://doi.org/10.3390/PR8050614

Azma, A., & Zhang, Y. (2020b). Tributary channel width effect on the flow behavior in trapezoidal and rectangular channel confluences. *Processes*, *8*(11), 1–15. https://doi.org/10.3390/pr8111344

Ben Meftah, M. (2022). Flow Hydrodynamic in Open Channels: A Constantly Evolving Topic. In *Water (Switzerland)* (Vol. 14, Number 24). MDPI. https://doi.org/10.3390/w14244120

Best, B. J. L., & Reid, I. (1985). *Separation zone at open-channel junctions*. *110*(11), 1588–1594.

Bryanskaya, Y., & Ostiakova, A. (2019). The conditions for occurrence of critical flow regime of water in the open stream. *E3S Web of Conferences*, *97*, 05006. https://doi.org/10.1051/e3sconf/20199705006

Cao, J., Kraut, M., Dittmeyer, R., Zhang, L., & Xu, H. (2018). Numerical analysis on the effect of bifurcation angle and inlet velocity on the distribution uniformity performance of consecutive bifurcating fluid flow distributors. *International Communications in Heat and Mass Transfer*, *93*, 60–65. https://doi.org/10.1016/j.icheatmasstransfer.2017.04.017

Chen, Z., Zhou, J., & Chen, Q. (2023). Research and Application of the Calculation Method of River Roughness Coefficient with Vegetation. *Water (Switzerland)*, *15*(14). https://doi.org/10.3390/w15142638

Cheng, T., Wang, J., & Sui, J. (2018). Calculation of critical flow depth using method of algebraic inequality. *Journal of Hydrology and Hydromechanics*, *66*(3), 316–322. https://doi.org/10.2478/johh-2018-0020

Cheng, Y., Song, Y., Liu, C., Wang, W., & Hu, X. (2022). Numerical Simulation Research on the Diversion Characteristics of a Trapezoidal Channel. *Water (Switzerland)*, *14*(17). https://doi.org/10.3390/w14172706

David, C., Chepkonga, D., Kulei, W., & Owuor, C. (2024). *Mathematical Modelling of Fluid Flow in Open Circular Channels in Sewerage Systems.* . https://doi.org/10.22541/essoar.171561457.75982212/v1

de Ruijsscher, T. V., Hoitink, A. J. F., Naqshband, S., & Paarlberg, A. J. (2019). Bed morphodynamics at the intake of a side channel controlled by sill geometry. *Advances in Water Resources*, *134*, 103452. https://doi.org/10.1016/j.advwatres.2019.103452

Demir, V., & Keskin, A. Ü. (2020). Obtaining the manning roughness with terrestrial-remote sensing technique and flood modeling using FLO-2D: A case study Samsun from Turkey. *Geofizika*, *37*(2), 131–156. https://doi.org/10.15233/gfz.2020.37.9

El Aydi, M., Barkatou, M., Bendaoud, R., Sbaa, M., & Bounouar, S. (2020). Use of Maple to Analytically Solve the Equations of an Electrical Circuit Containing a Resistor, Diodes and Voltage Generator. *Journal of Computer Science*, *16*(12), 1669–1683. https://doi.org/10.3844/jcssp.2020.1669.1683

Fadl-Elmola, S. A. M., Ciocan, C. M., & Popescu, I. (2021). Application of smooth particle hydrodynamics to particular flow cases solved by saint-venant equations. *Water (Switzerland)*, *13*(12). https://doi.org/10.3390/w13121671

Feng, W., Shao, Z., Gong, H., Xu, L., Yost, S. A., & Ma, H. (2022). Mechanics Experimental and numerical investigation of flow distribution pattern at a T-shape roadway crossing under extreme storms. https://doi.org/10.1080/19942060.2022.2141329

G. Kesserwani; J. Vazquez; N. Rivière; Q. Liang; G. Travin; and R. Mosé. (2010). *New Approach for Predicting Flow Bifurcation at Right-Angled Open-Channel Junction*. (September), 662–668.

Gąsiorowski, D., & Artichowicz, W. (2019). Distribution of Flows in A Channel Network Under Steady Flow Conditions. *Acta Scientiarum Polonorum*

Formatio Circumiectus, *18*(1), 27–37. https://doi.org/10.15576/ASP.FC/2019.18.1.27

Gautam, A. (2021). Determination of Manning's Roughness Coefficient in Bijayapur Irrigation Canal, Kaski, Nepal. *Himalayan Journal of Applied Science and Engineering*, *2*(2), 14–23. https://doi.org/10.3126/hijase.v2i2.43879

Ghamam, A. S., Abohatem, M. A., Bin Mohd Haniffah, M. R., & Othman, Ilya K. (2023). The Relationship Between Flow and Pressure Head of Partially Submerged Orifice Through CFD Modelling Using Flow-3D. In S. Harun, Ilya Khairanis Othman, & M. H. Jamal (Eds.), *Proceedings of the 5th International Conference on Water Resources (ICWR) – Volume 1* (pp. 235–250). Springer Nature Singapore.

Goudarzizadeh, R., & Musavi-Jahromi, S. H. (2020). Experiment-Based CFD Simulation of Flow Pattern at Open-Channel Junctions. *Iranian Journal of Science and Technology, Transactions of Civil Engineering*, *44*(S1), 427–436. https://doi.org/10.1007/s40996-019-00341-4

Guo, J., Julien, P. Y., Guo, J., & Julien, P. Y. (2005). Shear Stress in Smooth Rectangular Open-Channel Flows. *Journal of Hydraulic Engineering*, (January).

Harmizi, P. N. S., Zakaria, S. A. A., Zawawi, I. S. M., & Haniffah, M. R. M. (2023). Numerical Analysis on the Flow Depth Behaviour in Dividing Open-Channel for Trapezoidal and Rectangular Cross-Sectional Channel. *Journal of Advanced Research in Fluid Mechanics and Thermal Sciences*, *108*(2), 98–109. https://doi.org/10.37934/arfmts.108.2.98109

Harmizi, P. N. S., Zawawi, I. S. M., Haniffah, M. R. M., Khairudin, T. K. A., & Aris, H. (2022). A Mathematical Study of the Relation Between Discharges, Froude Number, Bed Width in Dividing Open Channel Flows. In *Lecture Notes in Civil Engineering* (Vol. 293). https://doi.org/10.1007/978-981-19-5947-9_15

Hassan, W. H., & Shabat, N. A. (2023). Numerical Investigation of the Optimum Angle for Open Channel Junction. *Civil Engineering Journal (Iran)*, *9*(5), 1121–1131. https://doi.org/10.28991/CEJ-2023-09-05-07

Hemmat Esfe, M., Afrand, M., Gharehkhani, S., Rostamian, H., Toghraie, D., & Dahari, M. (2016). An experimental study on viscosity of alumina-engine oil: Effects of temperature and nanoparticles concentration. *International Communications in*

Heat and Mass Transfer, *76*, 202–208. https://doi.org/10.1016/j.icheatmasstransfer.2016.05.013

Hsu, C.-C., Tang, C.-J., Lee, W.-J., & Shieh, M.-Y. (2002). Subcritical 90° Equal-Width Open-Channel Dividing Flow. *Journal of Hydraulic Engineering*, *128*(7). https://doi.org/10.1061/(asce)0733-9429(2002)128:7(716)

Ibrahim, I., Legori Ibrahim, S., & Khan, S. (2020). Flow structures in dividing open channels: a review. *IOP Conference Series: Earth and Environmental Science*, *437*(1), 012008. https://doi.org/10.1088/1755-1315/437/1/012008

Jamal, M. S., & Md Ali, Z. (2023). Kajian Menentukan Pekali Kekasaran Manning, ndi Saliran Kampung Parit Jelutong. *Recent Trends in Civil Engineering and Built Environment*, *4*(3), 639–650.

Jamshidi, A., Farsadizadeh, D., & Dalir, H. H. (2016). Variations of Flow Separation Zone at Lateral Intakes Entrance using Submerged Vanes. In *Journal homepage: Journal of Civil Engineering and Urbanism* (Vol. 6, Number 3). www.ojceu.ir/main54

Jasim, R. A., Hussen, W. Q., Abdullah, M. F., & Zulkifli, R. (2023). Numerical Simulation of Characterization of Hydraulic Jump Over an Obstacle in an Open Channel Flow. *Journal of Advanced Research in Fluid Mechanics and Thermal Sciences*, *106*(1), 1–15. https://doi.org/10.37934/arfmts.106.1.115

Kamali, P., Ebrahimian, H., & Parsinejad, M. (2018). Estimation of Manning roughness coefficient for vegetated furrows. *Irrigation Science*, *36*(6), 339–348. https://doi.org/10.1007/s00271-018-0593-9

Kesserwani, G., Ghostine, R., Vazquez, J., Mosé, R., Abdallah, M., & Ghenaim, A. (2008). Simulation of subcritical flow at open-channel junction. *Advances in Water Resources*, *31*(2), 287–297. https://doi.org/10.1016/j.advwatres.2007.08.007

Kestin, J., Sokolov, M., & Wakeham, W. A. (1978). Viscosity of Liquid Water in the Range of -8°C to 150°C. *J. Phys. Chem. Ref. Data*, *7*(3), 941–948.

Korson, L., Drost-Hansen, W., & Millero, F. J. (1969). Viscosity of water at various temperatures. *Journal of Physical Chemistry*, *73*(1), 34–39. https://doi.org/10.1021/j100721a006

Lama, K. S., Kudoh, K., & Kuroki, M. (2003). Study of flow characteristics of junction flow with free flow condition at branch channel. In *Annual Journal of Hydraulic Engineering* (Vol. 47).

Lama, S. K., Kuroki, Dr. M., & Hasegawa, D. K. (2002). Study of flow bifurcation at the 30 open channel-junction when the width ratio of branch channel to main channel is large. *Journal of Hydraulic Engineering*.

Le, T. B., Crosato, A., Mosselman, E., & Uijttewaal, W. S. J. (2018). On the stability of river bifurcations created by longitudinal training walls. Numerical investigation. *Advances in Water Resources*, *113*, 112–125. https://doi.org/10.1016/j.advwatres.2018.01.012

Liu, Y., Tang, Z., Huang, L., Stoesser, T., & Fang, H. (2024). On the role of the Froude number on flow, turbulence, and hyporheic exchange in open-channel flow through boulder arrays. *Physics of Fluids*, *36*(9). https://doi.org/10.1063/5.0222673

Macharia, K. S. (2014). Modeling fluid flow in an open rectangular channel with lateral inflow channel. Pan African University.

Magdalena, I., Imawan, R., & Nugroho, M. A. (2024). Numerical investigation for water flow in an irregular channel using Saint-Venant equations. *Journal of King Saud University - Science*, *36*(7). https://doi.org/10.1016/j.jksus.2024.103237

Malik, L., & Abdul Matin, M. (2021). Experimental study on flow and sediment distribution at off-take channel. *International Journal of Environmental Science and Development*, *12*(2), 35–41. https://doi.org/10.18178/IJESD.2021.12.2.1315

Mnassri, S., & Triki, A. (2021). On the unidirectional free-surface flow behavior in trapezoidal cross-sectional open-channels. *Ocean Engineering*, *223*. https://doi.org/10.1016/j.oceaneng.2021.108656

Mohammadi, S., & Kashefipour, S. M. (2014). Numerical modeling of flow in riverine basins using an improved dynamic roughness coefficient. *Water Resources*, *41*(4), 412–420. https://doi.org/10.1134/S0097807814040149

Mohammed, A. Y. (2015). Numerical analysis of flow over side weir. *Journal of King Saud University - Engineering Sciences*, *27*(1), 37–42. https://doi.org/10.1016/j.jksues.2013.03.004

Muhamediyeva, D., Mamatov, N., Turgunov, B., & Yusupova, D. (2024). Control of unstable water flow in open channels. *E3S Web of Conferences*, *590*. https://doi.org/10.1051/e3sconf/202459002002

Nazari-Sharabian, M., Karakouzian, M., & Hayes, D. (2020). Flow topology in the confluence of an open channel with lateral drainage pipe. *Hydrology*, *7*(3). https://doi.org/10.3390/HYDROLOGY7030057

Nazir, T., & Awan, S. A. (2021). Estimated Zones of Saint-Venant Equations for Flood Routing with Over Bank Unsteady Flow in Open Channel. *International Journal of Innovations in Science and Technology*, *3*(5), 96–109. https://doi.org/10.33411/ijist/2021030507

Nohani, E. (2019). Estimating the Manning's Roughness Coefficient in Rivers by Experimental Method. *Foot*, *1*(6), 50. https://doi.org/10.21859/ojest-02012

Nyaga, C. M., Okongo, M., & Kirimi, J. (2024). Developing a Model for Open Channel Fluid Flow with a Segment Base having Lateral Inflow Channel. *Journal of Advances in Mathematics and Computer Science*, *39*(9), 46–55. https://doi.org/10.9734/jamcs/2024/v39i91926

Ouro, P., Cea, L., Croquer, S., Dong, W., Garcia-Feal, O., Navas-Montilla, A., Rogers, B. D., Uchida, T., & Juez, C. (2024). Benchmark of computational hydraulics models for open-channel flow with lateral cavities. *Journal of Hydraulic Research*, *62*(5), 441–460. https://doi.org/10.1080/00221686.2024.2401905

Pandey, A. K., & Mishra, R. (2012). Comparison of flow characteristics at rectangular and trapezoidal channel junctions. *Journal of Physics: Conference Series*, *364*(1). https://doi.org/10.1088/1742-6596/364/1/012141

Pandey, A. K., & Mohapatra, P. K. (2019). 3D Simulation of Flow in a Right Angled Channel Junction with a Pit. *World Environmental and Water Resources Congress 2019*.

Pandey, K. K., Abhash, A., Tripathi, R. P., & Dayal, S. (2019). Flow-field near forty-five degree dividing open channel. *International Journal of Recent Technology and Engineering*, *8*(3), 2768–2773.https://doi.org/10.35940/ijrte.C4917.098319

Parsaie, A., Najafian, S., Omid, M. H., & Yonesi, H. (2017). Stage discharge prediction in heterogeneous compound open channel roughness. *ISH Journal of Hydraulic Engineering*, *23*(1), 49–56. https://doi.org/10.1080/09715010.2016.1235471

Pourbakhshian, S., & Pouraminian, M. (2021). Analytical Models for Optimal Design of a Trapezoidal Composite Channel Cross-Section. *Civil and Environmental Engineering Reports*, *31*(1), 118–138. https://doi.org/10.2478/ceer-2021-0009

Pradhan, S., Paikray, S., Das, S., & Sen Sahoo, A. (2024). Matlab Modelling of Various Open Channel Flow Parameters. *International Journal of Innovative Science*

and Research Technology (IJISRT), 1723–1735. https://doi.org/10.38124/ijisrt/ijisrt24mar1138

Putra, F. H. K., Taufik, M., & Nadlifah, M. (2024). Development of MATLAB GUI-Based Mathematics Learning Media with ADDIE Model to Enhance Students' Mathematical Connection Ability. *Mathematics Education Journal*, *8*(1), 102–113. https://doi.org/10.22219/mej.v8i1.28850

Qiu, C., Liu, S., Huang, J., Pan, W., & Xu, R. (2023). Influence of Cross-Sectional Shape on Flow Capacity of Open Channels. *Water (Switzerland)*, *15*(10). https://doi.org/10.3390/w15101877

Ramamurthy, A. S., Carballada, L. B., & Tran, D. M. (1989). Combining Open Channel Flow at Right Angled Junctions. *Journal of Hydraulic Engineering*, *114*(12), 1449–1460.

Ramamurthy, A. S., Qu, J., & Vo, D. (2007). Numerical and Experimental Study of Dividing Open-Channel Flows. *Journal of Hydraulic Engineering*, *133*(10), 1135–1144. https://doi.org/10.1061/(asce)0733-9429(2007)133:10(1135)

Ravichandran, S. R., Sengottian, M., Manoharan, D., Sekar, S., Sekar, J., Ravichandran, I., & Shanmugam, J. (2020). Study of fluid flow over corrugated open channels. *AIP Conference Proceedings*, *2240*. https://doi.org/10.1063/5.0011047

Rooniyan, F. (2014). The Effect of Confluence Angle on the Flow Pattern at a Rectangular Open-Channel. *Engineering, Technology & Applied Science Research*, *4*(1), 576–580. https://doi.org/10.48084/etasr.395

Sabah, S., & Bachir, A. (2023). Manning's roughness coefficient in a truncated triangular open-channel flow section. *Water Practice & Technology*, *18*(4), 845–858. https://doi.org/10.2166/wpt.2023.044

Saldana, M., Gallegos, S., Gálvez, E., Castillo, J., Salinas-Rodríguez, E., Cerecedo-Sáenz, E., Hernández-Ávila, J., Navarra, A., & Toro, N. (2024). The Reynolds Number: A Journey from Its Origin to Modern Applications. In *Fluids* (Vol. 9, Number 12). Multidisciplinary Digital Publishing Institute (MDPI). https://doi.org/10.3390/fluids9120299

Sayed Abu-Zaid, T. (2023). Three-dimensional numerical study for determining the optimum diversion angle of bifurcating channels. *Ain Shams Engineering Journal*, *14*(4). https://doi.org/10.1016/j.asej.2022.101940

Sayed, T. (2019). An experimental study of branching flow in open channels. *Limnological Review*, *19*(2), 93–101. https://doi.org/10.2478/limre-2019-0008

Schindfessel, L., Creëlle, S., & De Mulder, T. (2017). How Different Cross-Sectional Shapes Influence the Separation Zone of an Open-Channel Confluence. *Journal of Hydraulic Engineering*, *143*(9). https://doi.org/10.1061/(asce)hy.1943-7900.0001336

Shahari, N. A., Husaini Norwaza, N. A., Mohd Zawawi, I. S., Mohd Kamarul, N. A., & Said, A. (2021). Numerical investigation on the behavior of combining open-channel flow. *Indonesian Journal of Electrical Engineering and Computer Science*, *23*(2), 1110–1119. https://doi.org/10.11591/ijeecs.v23.i2.pp1110-1119

Shamloo, H., & Pirzadeh, B. (2008). Investigation of Characteristics of Separation Zones in T-Junctions. *Wseas Transactions on Mathematics*.

Siti Natasha Malik Fesal, Mas Fawzi, Mohd Azahari Razali, & Juntakan Taweekun. (2023). Flow Visualization on Submerged Flow Conditions in Open Channel Weir Downstream. *Journal of Advanced Research in Fluid Mechanics and Thermal Sciences*, *108*(2), 140–150. https://doi.org/10.37934/arfmts.108.2.140150

Sui, B., & Huang, S. hua. (2017). Numerical analysis of flow separation zone in a confluent meander bend channel. *Journal of Hydrodynamics*, *29*(4), 716–723. https://doi.org/10.1016/S1001-6058(16)60783-7

Tahmid, A., Rahman, Md. H., Mounota, S., & Abid Ahsan, K. (2021). Relationship Between Manning Roughness Coefficient and Flow Depth in Bangladesh River. *Malaysian Journal of Civil Engineering*, *33*(3). https://doi.org/10.11113/mjce.v33.17363

Teixeira, E. K. da C., Coelho, M. M. L. P., Pinto, E. J. de A., Diniz, J. G., & Saliba, A. P. M. (2018). Manning's roughness coefficient for the doce river. *Revista Brasileira de Recursos Hidricos*, *23*. https://doi.org/10.1590/2318-0331.231820180013

Toghraie, D., Alempour, S. M., & Afrand, M. (2016). Experimental determination of viscosity of water-based magnetite nanofluid for application in heating and cooling systems. *Journal of Magnetism and Magnetic Materials*, *417*, 243–248. https://doi.org/10.1016/j.jmmm.2016.05.092

Uruba, V. (2019). Reynolds number in laminar flows and in turbulence. *AIP Conference Proceedings*, *2118*. https://doi.org/10.1063/1.5114728

Waller, P., & Yitayew, M. (2016). *Irrigation and Drainage Engineering*.

Wan, D., Sun, G., & Zhang, M. (2021). Subcritical and supercritical bifurcations in axisymmetric viscoelastic pipe flows. https://doi.org/10.1017/jfm.2021.852

Webber, N. B., Struct, E., & Greated, C. A. (1967). An Investigation of flow behaviour at the junction of rectangular channels.

Weber, L. J., Schumate, E. D., & Mawer, N. (2001). Experiments on flow at a 90 open-channel junction. *Journal of Hydraulic Engineering*. www.iihr.uiowa.edu

Welahettige, P., Berg, C., Lundberg, J., Lie, B., & Vaagsaether, K. (2019). Computational Fluid Dynamics Study of the Effects of Drill Cuttings on the Open Channel Flow. *International Journal of Chemical Engineering*, *2019*. https://doi.org/10.1155/2019/6309261

Wibowo, H., Suripin, Kodoatie, R., & Isdiyana. (2015). Comparing the Calculation Method of the Manning Roughness Coefficient in Open Channels. *International Journal of Engineering Research & Technology (IJERT)*, *4*(06). www.ijert.org

Wuppukondur, A. (2018). Review of Flow Hydrodynamics and Sediment Transport at Open Channel Confluences. *Civil Engineering Research Journal*, *5*(3). https://doi.org/10.19080/cerj.2018.05.555664

Xue, Z., Zhou, L., & Liu, D. (2023). Accurate Numerical Modeling for 1D Open-Channel Flow with Varying Topography. *Water (Switzerland)*, *15*(16). https://doi.org/10.3390/w15162893

Zahran, A., Gado, T., & Rashwan, E. (2019). Comparison between Numerical, Analytical, and Field Solutions with Experimental Data for 90^{o} Open Channel Junctions. *Journal of Engineering Research*, *3*(9), 40–45. https://doi.org/10.21608/erjeng.2019.125701

Zakaria, S. A. A., Haniffah, M. R., Khairuddin, T. K. A., & Zawawi, I. S. (2025). 3D Simulation on Multiple Off-takes Branching Channel with Separation Zones. *Journal of Water Resources Management*.

Zawawi, I. S. M., Abdullah, N. L., Aris, H., Jaafar, B. A., Norwaza, N. A. H., & Yunos, M. H. F. M. (2019). Mathematical Modeling for Flood Mitigation: Effect of Bifurcation Angles in River Flowrates. *Civil Engineering and Architecture*, *7*(6A), 50–57. https://doi.org/10.13189/cea.2019.071406

Zhang, T., XU, W. lin, & WU, C. (2009). Effect of discharge ratio on flow characteristics in 90° equal-width open-channel junction. *Journal of Hydrodynamics*, *21*(4), 541–549. https://doi.org/10.1016/S1001-6058(08)60182-1

APPENDICES

APPENDIX 1

The discharge ratio for the trapezoidal channel when $\theta_1 = 0^0$

θ_1	θ_2	**Case**	**Discharge ratio,** q_r		
0	0	1	0.5000000000 - 2.861471065I	0.5000000000 + 2.861471065I	N/A
		2	0.8067160848 - 1.795691265I	0.8067160848 + 1.795691265I	N/A
0	15	1	0.000066414369	0.5461054114 + 2.894618625I	0.5461054114 - 2.894618625I
		2	0.000056298300	0.8226382348 + 1.822853525I	0.8226382348 - 1.822853525I
0	30	1	0.000127541633	0.5755808979 + 2.977391740I	0.5755808979 - 2.977391740I
		2	0.000109937000	0.8283452301 + 1.904747953I	0.8283452301 - 1.904747953I
0	45	1	0.000180220495	0.5865540452 + 3.117145351I	0.5865540452 - 3.117145351I
		2	0.000159398800	0.8213342498 + 2.059076928I	0.8213342498 - 2.059076928I
0	60	1	0.000221681207	0.5735640691 + 3.327364091I	0.5735640691 - 3.327364091I
		2	0.000202863500	0.7927343687 +	0.7927343687 -

				2.329207269I	2.329207269I
0	75	1	0.000249551834	0.5249051775 + 3.630964780I	0.5249051775 - 3.630964780I
		2	0.000238017700	0.7124608934 + 2.834048834I	0.7124608934 - 2.834048834I
0	90	1	0.000261913265	0.4161511761 + 4.066895263I	0.4161511761 - 4.066895263I
		2	0.000261913400	0.4161443710 + 4.066918481I	0.4161443710 - 4.066918481I

APPENDIX 2

The discharge ratio for the trapezoidal channel when $\theta_1 = 15°$

θ_1	θ_2	**Case**	**Discharge ratio, q_r**		
15	0	1	0.4538613814 + 2.843448566I	0.4538613814 - 2.843448566I	NA
		2	0.7911013937 + 1.778495250I	0.7911013937 - 1.778495250I	NA
15	15	1	0.000068735966	0.4999656320 + 2.877826804I	0.4999656320 - 2.877826804I
		2	0.000057957671	0.8066871059 + 1.805757756I	0.8066871059 - 1.805757756I
15	30	1	0.000131972562	0.5274728248 + 2.962173940I	0.5274728248 - 2.962173940I
		2	0.000113213590	0.8109839965 + 1.887546144I	0.8109839965 - 1.887546144I
15	45	1	0.000186476038	0.5340995931 + 3.104176391I	0.5340995931 - 3.104176391I
		2	0.000164273085	0.8009719983 + 2.041688804I	0.8009719983 - 2.041688804I
15	60	1	0.000229410270	0.5133969807 + 3.317939882I	0.5133969807 - 3.317939882I
		2	0.000209317248	0.7662873548 +	0.7662873548 -

				2.311985011I	2.311985011I
15	75	1	0.000258336239	0.4515365724 + 3.627616515I	0.4515365724 - 3.627616515I
		2	0.000245996179	0.6716673110 + 2.819384476I	0.6716673110 - 2.819384476I
15	90	1	0.000271264208	0.3192880683 + 4.074800116I	0.3192880683 - 4.074800116I
		2	0.000271264477	0.3192795235 + 4.074824040I	0.3192795235 - 4.074824040I

APPENDIX 3

The discharge ratio for the trapezoidal channel when $\theta_1 = 30^0$

θ_1	θ_2	**Case**	**Discharge ratio,** q_r		
30	0	1	0.4243553313 + 2.766033881I	0.4243553313 - 2.766033881I	NA
		2	0.7868614482 + 1.705903233I	0.7868614482 - 1.705903233I	NA
30	15	1	0.000076573345	0.4724229022 + 2.802332116I	0.4724229022 - 2.802332116I
		2	0.000063432073	0.8026398125 + 1.732801204I	0.8026398125 - 1.732801204I
30	30	1	0.000146917409	0.4999265413 + 2.889798407I	0.4999265413 - 2.889798407I
		2	0.000124037956	0.8066540658 + 1.813122850I	0.8066540658 - 1.813122850I
30	45	1	0.000207572616	0.5041908116 + 3.037208109I	0.5041908116 - 3.037208109I
		2	0.000180428105	0.7956266293 + 1.964932600I	0.7956266293 - 1.964932600I
30	60	1	0.000255493626	0.4774402349 + 3.260946738I	0.4774402349 - 3.260946738I
		2	0.000230818529	0.7582042246 +	0.7582042246 -

				2.233155376I	2.233155376I
30	75	1	0.000288023305	0.4023784604 + 3.590083845I	0.4023784604 - 3.590083845I
		2	0.000272768719	0.6545505153 + 2.745178973I	0.6545505153 - 2.745178973I
30	90	1	0.000302933150	0.2401870884 + 4.077678078I	0.2401870884 - 4.077678078I
		2	0.000302933571	0.2401765844 + 4.077704574I	0.2401765844 - 4.077704574I

APPENDIX 4

The discharge ratio for the trapezoidal channel when $\theta_1 = 45^0$

θ_1	θ_2	Case	Discharge ratio, q_r		
45	0	1	0.4133558446 + 2.611054645I	0.4133558446 - 2.611054645I	N/A
		2	0.7948174697 + 1.569320757I	0.7948174697 - 1.569320757I	N/A
45	15	1	0.000093533850	0.4657604019 + 2.650073651I	0.4657604019 - 2.650073651I
		2	0.000074644812	0.8113592294 + 1.595196459I	0.8113592294 - 1.595196459I
45	30	1	0.000179187530	0.4956158083 + 2.742019924I	0.4956158083 - 2.742019924I
		2	0.000146280247	0.8163584990 + 1.672022806I	0.8163584990 - 1.672022806I
45	45	1	0.000253112140	0.4998734439 + 2.897769422I	0.4998734439 - 2.897769422I
		2	0.000213878445	0.8066091456 + 1.818019800I	0.8066091456 - 1.818019800I
45	60	1	0.000311888100	0.4688619674 + 3.138363375I	0.4688619674 - 3.138363375I
		2	0.000275888366	0.7704568039 +	0.7704568039 -

				2.079501995I	2.079501995I
45	75	1	0.000352431940	0.3793144587 + 3.503771914I	0.3793144587 - 3.503771914I
		2	0.000329862042	0.6644960296 + 2.594217879I	0.6644960296 - 2.594217879I
45	90	1	0.000372000010	0.1722403341 + 4.075702275I	0.1722403341 - 4.075702275I
		2	0.000372001137	0.1722262016 + 4.075734449I	0.1722262016 - 4.075734449I

APPENDIX 5

The discharge ratio for the trapezoidal channel when $\theta_1 = 60^0$

θ_1	θ_2	**Case**	**Discharge ratio,** q_r		
60	0	1	0.4263250903 + 2.332605455I	0.4263250903 - 2.332605455I	N/A
		2	0.8158835905 + 1.348326872I	0.8158835905 - 1.348326872I	N/A
60	15	1	0.000131482519	0.4864225730 + 2.375139510I	0.4864225730 - 2.375139510I
		2	0.000096984140	0.8338330477 + 1.372070554I	0.8338330477 - 1.372070554I
60	30	1	0.000251039735	0.5223064984 + 2.471733600I	0.5223064984 - 2.471733600I
		2	0.000190883475	0.8413532061 + 1.441801678I	0.8413532061 - 1.441801678I
60	45	1	0.000354441323	0.5308048678 + 2.636782996I	0.5308048678 - 2.636782996I
		2	0.000282007926	0.8358169980 + 1.575305127I	0.8358169980 - 1.575305127I
60	60	1	0.000437815161	0.4997810924 + 2.899797104I	0.4997810924 - 2.899797104I
		2	0.000370044204	0.8065310627 +	0.8065310627 -

				1.819244347I	1.819244347I
60	75	1	0.000497362216	0.3956360764 + 3.323651661I	0.3956360764 - 3.323651661I
		2	0.000453574377	0.7096814712 + 2.322798771I	0.7096814712 - 2.322798771I
60	90	1	0.000529229124	0.1112713479 + 4.065704978I	0.1112713479 - 4.065704978I
		2	0.000529229870	0.1112506317 + 4.065750115I	0.1112506317 - 4.065750115I

APPENDIX 6

The discharge ratio for the trapezoidal channel when $\theta_1 = 75^0$

θ_1	θ_2	Case	Discharge ratio, q_r		
75	0	1	0.4749700466 + 1.800223321I	0.4749700466 - 1.800223321I	N/A
		2	0.8508949019 + 0.9881394689I	0.8508949019 - 0.9881394689I	N/A
75	15	1	0.000249226272	0.5482096464 + 1.846910905I	0.5482096464 - 1.846910905I
		2	0.000148862317	0.8709907424 + 1.007603975I	0.8709907424 - 1.007603975I
75	30	1	0.000470937482	0.5972420592 + 1.942917950I	0.5972420592 - 1.942917950I
		2	0.000295980880	0.8829582015 + 1.062761132I	0.8829582015 - 1.062761132I
75	45	1	0.000663969112	0.6201773408 + 2.107492059I	0.6201773408 - 2.107492059I
		2	0.000448316435	0.8855863895 + 1.168968012I	0.8855863895 - 1.168968012I
75	60	1	0.000826322371	0.6037020813 + 2.383551847I	0.6037020813 - 2.383551847I
		2	0.000614129327	0.8716262437 +	0.8716262437 -

				1.368138308I	1.368138308I
75	75	1	0.000954367116	0.4995228164 + 2.882582093I	0.4995228164 + 2.882582093I
		2	0.000805287046	0.8063134411 + 1.808568078I	0.8063134411 - 1.808568078I
75	90	1	0.001042095061	0.0542697543 + 4.028257016I	0.05426975437 - 4.028257016I
		2	0.001042097947	0.05422717560 + 4.028342753I	0.05422717560 - 4.028342753I

APPENDIX 7

The discharge ratio for the trapezoidal channel when $\theta_1 = 90^0$

θ_1	θ_2	**Case**	**Discharge ratio, q_r**		
90	0	1	1.171226035000	0.000790300240	N/A
		2	1.126376216000	0.674147370000	N/A
90	15	1	0.006689782010	0.144956968100	1.209505849000
		2	0.000349551367	0.702995094400	1.143592282000
90	30	1	0.008123314760	0.245873206800	1.265326368000
		2	0.000723840684	0.716349825900	1.167759736000
90	45	1	0.010987478700	0.295369129500	1.348790724000
		2	0.001222570826	0.712992460300	1.203161078000
90	60	1	0.018578765900	0.275139098800	1.483210210000
		2	0.002107568294	0.683595337500	1.260850814000
90	75	1	1.757643008000	0.06638769415 + 0.06990954025I	0.06638769415 - 0.06990954025I
		2	0.004838085373	0.584297576400	1.384609584000
90	90	1	-0.026133512100	0.5130667561 + 150.9954353I	0.5130667561 - 150.9954353I

		2	-0.026131597130	0.8197818834 + 93.88117934I	0.8197818834 - 93.88117934I

APPENDIX 8

The discharge ratio for the rectangular channel when $\theta_1 = 0^0$

θ_1	θ_2	**Case**	**Discharge ratio, q_r**	
0	0	1	0.5000000000 - 2.832491834I	0.5000000000 + 2.832491834I
		2	0.8333333334 + 1.652238547I	0.8333333334 - 1.652238547I
0	15	1	0.5461392314 - 2.865381461I	0.5461392314 + 2.865381461I
		2	0.8469445738 + 1.677747688I	0.8469445738 - 1.677747688I
0	30	1	0.5756459162 - 2.947356362I	0.5756459162 + 2.947356362I
		2	0.8514377717+ 1.755612718I	0.8514377717 - 1.755612718I
0	45	1	0.5866460837 - 3.085704455I	0.5866460837 + 3.085704455I
		2	0.8444196963 + 1.903650830I	0.8444196963 - 1.903650830I
0	60	1	0.5736775976 - 3.293773640I	0.5736775976 + 3.293773640I
		2	0.8172901037 +	0.8172901037 -

			2.166579261I	2.166579261I
0	75	1	0.5250335256 - 3.594234147I	0.5250335256 + 3.594234147I
		2	0.7393746843 + 2.672930807I	0.7393746843 - 2.672930807I
0	90	1	0.4162867882 - 4.025588111I	0.4162867882 + 4.025588111I
		2	0.4162782116 + 4.025617063I	0.4162782116 - 4.025617063I

APPENDIX 9

The discharge ratio for the rectangular channel when $\theta_1 = 15^0$

θ_1	θ_2	**Case**	**Discharge ratio, q_r**	
15	0	1	0.4538607686 - 2.814894291I	0.4538607686 + 2.814894291I
		2	0.8200330548 + 1.636135102I	0.8200330548 - 1.636135102I
15	15	1	0.5000000000 - 2.849020194I	0.5000000000 + 2.849020194I
		2	0.8333333333 + 1.661684190I	0.8333333333 - 1.661684190I
15	30	1	0.5275394241 - 2.932569658I	0.5275394241 + 2.932569658I
		2	0.8365716767 + 1.739341583I	0.8365716767 - 1.739341583I
15	45	1	0.5341940785 - 3.073159138I	0.5341940785 + 3.073159138I
		2	0.8268763138 + 1.887005138I	0.8268763138 - 1.887005138I
15	60	1	0.5135136142 - 3.284749755I	0.5135136142 + 3.284749755I
		2	0.7942384322 +	0.7942384322 -

			2.149711918I	2.149711918I
15	75	1	0.4516684284 - 3.591228473I	0.4516684284 + 3.591228473I
		2	0.7028482116 + 2.657768602I	0.7028482116 - 2.657768602I
15	90	1	0.3194272727 - 4.033697625I	0.3194272727 + 4.033697625I
		2	0.3194165895 + 4.033727450I	0.3194165895 - 4.033727450I

APPENDIX 10

The discharge ratio for the rectangular channel when $\theta_1 = 30^0$

θ_1	θ_2	**Case**	**Discharge ratio, q_r**	
30	0	1	0.4243540838 - 2.738422479I	0.4243540838 + 2.738422479I
		2	0.8168828573 + 1.567593871I	0.8168828573 - 1.567593871I
30	15	1	0.4724605759 - 2.774467728I	0.4724605759 + 2.774467728I
		2	0.8303221901 + 1.592670897I	0.8303221901 - 1.592670897I
30	30	1	0.5000000000 - 2.861119413I	0.5000000000 + 2.861119413I
		2	0.8333333334 + 1.668599331I	0.8333333334 - 1.668599331I
30	45	1	0.5042952108 - 3.007073217I	0.5042952108 + 3.007073217I
		2	0.8228333108 + 1.813354375I	0.8228333108 - 1.813354375I
30	60	1	0.4775692291 - 3.228545652I	0.4775692291 + 3.228545652I
		2	0.7879829499 +	0.7879829499 -

			2.072670444I	2.072670444I
30	75	1	0.4025244005 - 3.554283474I	0.4025244005 + 3.554283474I
		2	0.6888738901 + 2.582148425I	0.6888738901 - 2.582148425I
30	90	1	0.2403412429 - 4.036706421I	0.2403412429 + 4.036706421I
		2	0.2403280768 + 4.036739455I	0.2403280768 - 4.036739455I

APPENDIX 11

The discharge ratio for the rectangular channel when $\theta_1 = 45^0$

θ_1	θ_2	**Case**	**Discharge ratio, q_r**	
45	0	1	0.4133539163 - 2.585096725I	0.4133539163 + 2.585096725I
		2	0.8245228246 + 1.439124909I	0.8245228246 - 1.439124909I
45	15	1	0.4658059215 - 2.623857726I	0.4658059215 + 2.623857726I
		2	0.8385829933 + 1.463042834I	0.8385829933 - 1.463042834I
45	30	1	0.4957047892 - 2.714959351I	0.4957047892 + 2.714959351I
		2	0.8425082971 - 1.535117809I	0.8425082971 - 1.535117809I
45	45	1	0.5000000000 - 2.869179695I	0.5000000000 + 2.869179695I
		2	0.8333333333 + 1.673206406I	0.8333333333 - 1.673206406I
45	60	1	0.4690185245 - 3.107343402I	0.4690185245 + 3.107343402I
		2	0.8001464023 +	0.8001464023 -

			1.923640718I	1.923640718I
45	75	1	0.3794919222 - 3.468976718I	0.3794919222 + 3.468976718I
		2	0.7004964995 + 2.429927574I	0.7004964995 - 2.429927574I
45	90	1	0.1724282626 - 4.034798308I	0.1724282626 + 4.034798308I
		2	0.1724105783 + 4.034838426I	0.1724105783 - 4.034838426I

APPENDIX 12

The discharge ratio for the rectangular channel when $\theta_1 = 60^0$

θ_1	θ_2	**Case**	**Discharge ratio,** q_r	
60	0	1	0.4263224024 - 2.309453097I	0.4263224024 + 2.309453097I
		2	0.8435426343 + 1.232836837I	0.8435426343 - 1.232836837I
60	15	1	0.4864863858 - 2.351724309I	0.4864863858 + 2.351724309I
		2	0.8587571813 + 1.254505731I	0.8587571813 - 1.254505731I
60	30	1	0.5224307709 - 2.447444127I	0.5224307709 + 2.447444127I
		2	0.8649370981 + 1.319207077I	0.8649370981 - 1.319207077I
60	45	1	0.5309814755 - 2.610880967I	0.5309814755 + 2.610880967I
		2	0.8597075049 + 1.443996668I	0.8597075049 - 1.443996668I
60	60	1	0.5000000000 - 2.871244226I	0.5000000000 + 2.871244226I
		2	0.8333333333 +	0.8333333333 -

			1.674386462I	1.674386462I
60	75	1	0.3958853704 - 3.290720240I	0.3958853704 + 3.290720240I
		2	0.7444868412 + 2.160828908I	0.7444868412 - 2.160828908I
60	90	1	0.1115372099 - 4.024778936I	0.1115372099 + 4.024778936I
		2	0.1115111007 + 4.024835191I	0.1115111007 - 4.024835191I

APPENDIX 13

The discharge ratio for the rectangular channel when $\theta_1 = 75^0$

θ_1	θ_2	**Case**	**Discharge ratio,** q_r	
75	0	1	0.4749664744 - 1.782221807I	0.4749664744 + 1.782221807I
		2	0.8743213990 + 0.9002848483I	0.8743213990 - 0.9002848483I
75	15	1	0.5483315716 - 1.828663248I	0.5483315716 + 1.828663248I
		2	0.8912876210 + 0.9176906009I	0.8912876210 - 0.9176906009I
75	30	1	0.5974755995 - 1.923823743I	0.5974755995 + 1.923823743I
		2	0.9013332628 + 0.9680878504I	0.9013332628 - 0.9680878504I
75	45	1	0.6205080778 - 2.086789318I	0.6205080778 + 2.086789318I
		2	0.9033932006 + 1.065785411I	0.9033932006 - 1.065785411I
75	60	1	0.6041146296 - 2.360051879I	0.6041146296 + 2.360051879I
		2	0.8911110804 +	0.8911110804 -

			1.250298240I	1.250298240I
75	75	1	0.5000000000 - 2.853903771I	0.5000000000 + 2.853903771I
		2	0.8333333333 + 1.664475233I	0.8333333333 - 1.664475233I
75	90	1	0.05479141481 - 3.987023011I	0.05479141481 + 3.987023011I
		2	0.05473775213 + 3.987129826I	0.05473775213 - 3.987129826I

APPENDIX 14

The discharge ratio for the rectangular channel when $\theta_1 = 90^0$

θ_1	θ_2	**Case**	**Discharge ratio,** q_r	
90	0	1	0.000000000000	1.167478482000
		2	0.715673027100	1.117812747000
90	15	1	0.155759144700	1.205386310000
		2	0.739238386300	1.132991226000
90	30	1	0.258498495000	1.260819020000
		2	0.749472182200	1.154391758000
90	45	1	0.311243839000	1.343899636000
		2	0.745147304000	1.185881873000
90	60	1	0.299041377000	1.477884203000
		2	0.717899246300	1.237486132000
90	75	1	0.138897758000	1.751519412000
		2	0.629117374400	1.348966308000
90	90	1	0.5000000000 - 150.9906469I	0.5000000000 + 150.9906469I
		2	0.8333333333 + 87.17480929I	0.8333333333 - 87.17480929I

APPENDIX 15

The discharge ratio for the V-shaped channel when $\theta_1 = 0^0$

θ_1	θ_2	**Case**	**Discharge ratio,** q_r	
0	0	1	0.5000000000 - 3.634117326I	0.5000000000 + 3.634117326I
		2	0.5000000000 + 3.655111416I	0.5000000000 - 3.655111416I
0	15	1	0.5461481972 - 3.607989670I	0.5461481972 + 3.607989670I
		2	0.5461488004 + 3.693203295I	0.5461488004 - 3.693203295I
0	30	1	0.5756641641 - 3.508645262I	0.5756641641 + 3.508645262I
		2	0.5756651764 + 3.795645758I	0.5756651764 - 3.795645758I
0	45	1	0.5866742924 - 3.313177976I	0.5866742924 + 3.313177976I
		2	0.5866757371 + 3.971661358I	0.5866757371 - 3.971661358I
0	60	1	0.5737169162 - 2.964702885I	0.5737169162 + 2.964702885I
		2	0.5737189263 +	0.5737189263 -

			4.238485900I	4.238485900I
0	75	1	0.5250857823 - 2.303903445I	0.5250857823 + 2.303903445I
		2	0.5250884537 + 4.625764399I	0.5250884537 - 4.625764399I
0	90	1	0.000000000000	1.000084685000
		2	0.4163583717 + 5.184509752I	0.4163583717 - 5.184509752I

APPENDIX 16

The discharge ratio for the V-shaped channel when $\theta_1 = 15^0$

θ_1	θ_2	**Case**	**Discharge ratio,** q_r	
15	0	1	0.4538518028 - 3.672065510I	0.4538518028 + 3.672065510I
		2	0.4538511996 + 3.628769285I	0.4538511996 - 3.628769285I
15	15	1	0.5000000000 - 3.647017009I	0.5000000000 + 3.647017009I
		2	0.5000000000 + 3.667937435I	0.5000000000 - 3.667937435I
15	30	1	0.5275483899 - 3.549480642I	0.5275483899 + 3.549480642I
		2	0.5275487711 + 3.771982995I	0.5275487711 - 3.771982995I
15	45	1	0.5342123264 - 3.356565191I	0.5342123264 + 3.356565191I
		2	0.5342130598 + 3.950544085I	0.5342130598 - 3.950544085I
15	60	1	0.5135418228 - 3.011119897I	0.5135418228 + 3.011119897I
		2	0.5135430815 +	0.5135430815 -

			4.221695955I	4.221695955I
15	75	1	0.4517077471 - 2.352656456I	0.4517077471 + 2.352656456I
		2	0.4517095243 + 4.616824281I	0.4517095243 - 4.616824281I
15	90	1	0.000000000000	0.844228136000
		2	0.3194818701 + 5.190812013I	0.3194818701 - 5.190812013I

APPENDIX 17

The discharge ratio for the V-shaped channel when $\theta_1 = 30^0$

θ_1	θ_2	**Case**	**Discharge ratio,** q_r	
30	0	1	0.4243358359 - 3.773977226I	0.4243358359 + 3.773977226I
		2	0.4243348236 + 3.528828719I	0.4243348236 - 3.528828719I
30	15	1	0.4724516101 - 3.750530106I	0.4724516101 + 3.750530106I
		2	0.4724512289 + 3.569803638I	0.4724512289 - 3.569803638I
30	30	1	0.5000000000 - 3.656479504I	0.5000000000 +3.656479504I
		2	0.5000000000+ 3.677346234I	0.5000000000 - 3.677346234I
30	45	1	0.5043041764 - 3.468599998I	0.5043041764 + 3.468599998I
		2	0.5043044947 + 3.862448957I	0.5043044947 - 3.862448957I
30	60	1	0.4775874769 - 3.128073824I	0.4775874769 + 3.128073824I
		2	0.4775883208 +	0.4775883208 -

			4.146132508I	4.146132508I
30	75	1	0.4025526091 - 2.467120763I	0.4025526091 + 2.467120763I
		2	0.4025539097 + 4.566264506I	0.4025539097 - 4.566264506I
30	90	1	0.000000000000	0.741446634000
		2	0.2403822939 + 5.193153996I	0.2403822939 - 5.193153996I

APPENDIX 18

The discharge ratio for the V-shaped channel when $\theta_1 = 45^0$

θ_1	θ_2	**Case**	**Discharge ratio,** q_r	
45	0	1	0.4133257076 - 3.949024298I	0.4133257076 + 3.949024298I
		2	0.4133242629 + 3.332253157I	0.4133242629 - 3.332253157I
45	15	1	0.4657876736 - 3.928114079I	0.4657876736 + 3.928114079I
		2	0.4657869402 + 3.375778038I	0.4657869402 - 3.375778038I
45	30	1	0.4956958236 - 3.840574114I	0.4956958236 + 3.840574114I
		2	0.4956955053 + 3.488373655I	0.4956955053 - 3.488373655I
45	45	1	0.5000000000 - 3.662793876I	0.5000000000 + 3.662793876I
		2	0.5000000000 - 3.683625040I	0.5000000000 - 3.683625040I
45	60	1	0.4690274903 - 3.333343239I	0.4690274903+ 3.333343239I
		2	0.4690280103 +	0.4690280103 -

			3.988503466I	3.988503466I
45	75	1	0.3795101701 - 2.670726086I	0.3795101701 + 2.670726086I
		2	0.3795110490 + 4.455064809I	0.3795110490 - 4.455064809I
45	90	1	0.000000000000	0.688659399000
		2	0.1724574256 + 5.191676389I	0.1724574256 - 5.191676389I

APPENDIX 19

The discharge ratio for the V-shaped channel when $\theta_1 = 60^0$

θ_1	θ_2	**Case**	**Discharge ratio,** q_r	
60	0	1	0.4262830838 - 4.214346896I	0.4262830838 + 4.214346896I
		2	0.4262810737 + 2.981859336I	0.4262810737 - 2.981859336I
60	15	1	0.4864581772 - 4.197742922I	0.4864581772 + 4.197742922I
		2	0.4864569185 + 3.028405369I	0.4864569185 - 3.028405369I
60	30	1	0.5224125231 - 4.122666525I	0.5224125231 + 4.122666525I
		2	0.5224116792 + 3.145930568I	0.5224116792 - 3.145930568I
60	45	1	0.5309725097 - 3.965965382I	0.5309725097 + 3.965965382I
		2	0.5309719897 + 3.352308094I	0.5309719897 - 3.352308094I
60	60	1	0.5000000000 - 3.664418115I	0.5000000000 + 3.664418115I
		2	0.5000000000 +	0.5000000000 -

			3.685240409I	3.685240409I
60	75	1	0.3958943363 - 3.017646244I	0.3958943363 + 3.017646244I
		2	0.3958947946 + 4.226358286I	0.3958947946 - 4.226358286I
60	90	1	0.000000000000	0.700813829000
		2	0.1115563906 + 5.183904408I	0.1115563906 - 5.183904408I

APPENDIX 20

The discharge ratio for the V-shaped channel when $\theta_1 = 75^0$

θ_1	θ_2	**Case**	**Discharge ratio,** q_r	
75	0	1	0.4749142177 - 4.599408589I	0.4749142177 + 4.599408589I
		2	0.4749115463 + 2.317520379I	0.4749115463 - 2.317520379I
75	15	1	0.5482922529 - 4.590607816I	0.5482922529 + 4.590607816I
		2	0.5482904757 + 2.366363311I	0.5482904757 - 2.366363311I
75	30	1	0.5974473909 - 4.540388745I	0.5974473909 + 4.540388745I
		2	0.5974460903 + 2.481353390I	0.5974460903 - 2.481353390I
75	45	1	0.6204898299 - 4.429848024I	0.6204898299 + 4.429848024I
		2	0.6204889510 + 2.686038555I	0.6204889510 - 2.686038555I
75	60	1	0.6041056637 - 4.202430938I	0.6041056637 + 4.202430938I
		2	0.6041052054 +	0.6041052054 -

			3.034895175I	3.034895175I
75	75	1	0.5000000000 - 3.650865603I	0.5000000000 + 3.650865603I
		2	0.5000000000 + 3.671765701I	0.5000000000 - 3.671765701I
75	90	1	0.000000000000	0.860876687000
		2	0.05480083896 + 5.154678948I	0.05480083896 - 5.154678948I

APPENDIX 21

The discharge ratio for the V-shaped channel when $\theta_1 = 90^0$

θ_1	θ_2	**Case**	**Discharge ratio,** q_r	
90	0	1	0.5836451098 - 5.154907829I	0.5836451098 + 5.154907829I
		2	0.0000000000	1.1673689050
90	15	1	0.6805204708 - 5.161246078I	0.6805204708 + 5.161246078I
		2	0.155773813200	1.205262447000
90	30	1	0.7596194386 - 5.163601318I	0.7596194386 + 5.163601318I
		2	0.2585574188	1.2606779930
90	45	1	0.8275435286 - 5.162115036I	0.8275435286 + 5.162115036I
		2	0.3113468684	1.3437382800
90	60	1	0.8884445423 - 5.154297964I	0.8884445423 + 5.154297964I
		2	0.299194970500	1.477692248000
90	75	1	0.9451996194 - 5.124902185I	0.9451996194 + 5.124902185I

		2	0.139136817400	1.751261505000
90	90	1	0.5000000000 + 150.9464114I	0.5000000000 - 150.9464114I
		2	0.5000000000 + 150.9437787I	0.5000000000 - 150.9437787I

AUTHOR'S PROFILE



Puteri Nadia Shafiqah Harmizi obtained her Bachelor of Science in Business Mathematics (Hons.) in 2014 from Universiti Utara Malaysia (UUM), her Master of Science in Applied Mathematics in 2018 from Universiti Tun Hussein Onn Malaysia (UTHM), and her Doctor of Philosophy (PhD) in Mathematics from Universiti Teknologi MARA (UiTM), Shah Alam, Selangor, Malaysia in 2025. Throughout her PhD studies, she actively participated in national and international conferences such as the International Conference on Water Resources in 2021 and National Symposium on Mathematical Sciences in 2024. Her research has been published in the Journal of Advanced Research in Fluid Mechanics and Thermal Sciences in 2023 and two indexed proceedings. In 2024, she participated in the 3-Minute Thesis (3MT) competition and served as a committee member for the International Day of Mathematics (IDM) program, organised by the faculty. She has also taken part in numerous academic and research-based workshops to strengthen her methodological and analytical skills. She is passionate about mathematical modelling in the field of open-channel hydraulics that contribute to sustainable water resource management.

LIST OF PUBLICATION:

Puteri Nadia Shafiqah Harmizi, Iskandar Shah Mohd Zawawi, Mathematical modeling of the flow division in V-shaped cross-sectional channel. *AIP Conf. Proc.* 19 August 2024; 3189 (1): 030010. https://doi.org/10.1063/5.0224694

Puteri Nadia Shafiqah Harmizi, Siti Aimi Asyarah Zakaria, Iskandar Shah Mohd Zawawi, Mohd Ridza Mohd Haniffah, Numerical Analysis on the Flow Depth Behavior in Dividing Open-Channel for Trapezoidal and Rectangular Cross-Sectional Channel. *Journal of Advanced Research in Fluid Mechanics and Thermal Sciences*, *108*(2), 98–109, 2023. https://doi.org/10.37934/arfmts.108.2.98109

Puteri Nadia Shafiqah Harmizi, Iskandar Shah Mohd Zawawi, Mohd Ridza Mohd Haniffah, Taufiq Khairi Ahmad Khairudin, Hazleen Aris, A Mathematical Study of the Relation Between Discharges, Froude Number, Bed Width in Dividing Open Channel Flows. Proceedings of the 5th International Conference on Water Resources (ICWR) – Volume 1. Lecture Notes in Civil Engineering, vol 293. Springer, Singapore, 2023. https://doi.org/10.1007/978-981-19-5947-9_15.

Puteri Nadia Shafiqah Harmizi, Iskandar Shah Mohd Zawawi, Mohd Ridza Mohd Haniffah, Siti Aimi Asyarah Zakaria, Comparative Analysis Dishcarge Ratio in Trapezoidal Cross-section Open-channel Dividing Flow. Journal of Quality Measurement and Analysis. (Accepted: Publish in June 2026).